Instituto Alberto Luiz Coimbra de
Pós-Graduação e Pesquisa de Engenharia
COPPE
UFRJ

CONVECTION HEAT TRANSFER COEFFICIENT ESTIMATION IN DUCTS USING THE RECIPROCITY FUNCTIONAL METHOD

Inoussa Tougri

Tese de Doutorado apresentada ao Programa de Pós-graduação em Engenharia Mecânica, COPPE, da Universidade Federal do Rio de Janeiro, como parte dos requisitos necessários à obtenção do título de Doutor em Engenharia Mecânica.

Orientadores: Marcelo José Colaço
Fabio Bozzoli

Rio de Janeiro
Junho de 2018

CONVECTION HEAT TRANSFER COEFFICIENT ESTIMATION IN DUCTS USING THE RECIPROCITY FUNCTIONAL METHOD

Inoussa Tougri

TESE SUBMETIDA AO CORPO DOCENTE DO INSTITUTO ALBERTO LUIZ COIMBRA DE PÓS-GRADUAÇÃO E PESQUISA DE ENGENHARIA (COPPE) DA UNIVERSIDADE FEDERAL DO RIO DE JANEIRO COMO PARTE DOS REQUISITOS NECESSÁRIOS PARA A OBTENÇÃO DO GRAU DE DOUTOR EM CIÊNCIAS EM ENGENHARIA MECÂNICA.

Examinada por:

Prof. Marcelo José Colaço, D.Sc.

Prof. Fabio Bozzoli, Ph.D.

Prof. Albino José Kalab Leiroz, Ph.D.

Prof. Helcio Rangel Barreto Orlande, Ph.D.

Prof. Manuel Ernani de Carvalho Cruz, Ph.D.

Prof. Nilson Costa Roberty, D.Sc.

Dr. Carlos Frederico Trotta Matt, D.Sc.

RIO DE JANEIRO, RJ – BRASIL
JUNHO DE 2018

Tougri, Inoussa

Convection Heat Transfer Coefficient Estimation in Ducts using the Reciprocity Functional Method/Inoussa Tougri. – Rio de Janeiro: UFRJ/COPPE, 2018.

XVII, 124 p.: il.; 29, 7cm.

Orientadores: Marcelo José Colaço
Fabio Bozzoli

Tese (doutorado) – UFRJ/COPPE/Programa de Engenharia Mecânica, 2018.

Referêcias Bibliográficas: p. 118 – 124.

1. Inverse Problem. 2. Reciprocity Functional. 3. Heat Transfer. I. Colaço, Marcelo José *et al.* II. Universidade Federal do Rio de Janeiro, COPPE, Programa de Engenharia Mecânica. III. Título.

"Education is the most powerful weapon which you can use to change the world."

NELSON MANDELA

(1918 – 2013)

Acknowledgement

Foremost, I would like to express my sincere gratitude to my advisor Prof. Marcelo José Colaço for the continuous support of my D.Sc. study and research, for his patience, motivation, enthusiasm, and immense knowledge. His guidance helped me in all the time of research and writing of this thesis. I could not have imagined having a better advisor and mentor for my D.Sc. study.

My sincere thanks also goes to my co-adviser Prof. Fabio Bozzoli for offering me the internship opportunities in their groups and leading me working on the experimental part of this thesis I did in their laboratory at the University of Parma in Italy. I would like to thank all the research group for they help during my stay in Parma. I cannot forget the help of Andréa Mocerino, Chiara Freddi and Luca Cattani with the experimental setup of this work.

I thank my fellow labmates at Federal University of Rio de Janeiro: *Bernard Lamien, Bruna Loiola, Bruno Jaccoud, Camila Ribeiro, César Pacheco, Diana Santos, Diego Estumano, Gabriel Verissimo, Henrique Massard, Iasmin Herzog, Luiz Abreu, Masoud Ghanbari, Nilton Pereira, Paula Falquetto, Ricardo Suarez, Ricardo Padilha, Sami Massalami, Souleymane Zio* and all the workers of the Laboratory of Thermal Machines (LMT/COPPE) and LTTC/COPPE.

My thanks to all the professors of the Department of Mechanical Engineering of Federal University of Rio de Janeiro and to Vera Noronha the secretary of the Department.

I would like to thank my family: my parents Kindaogo Moumouni Tougri and Asseta Segda, my aunt Alima Arzuma and heir husband Lokré Nagnango and my uncle Hado Tougri.

This work has been partially funded by CNPq and CAPES (fostering agencies from the Brazilian Ministries of Science and Education, respectively), FAPERJ (fostering agency from the State of Rio de Janeiro), and Emilia-Romagna Region (POR FSE 2007-2013) Italy.

Resumo da Tese apresentada à COPPE/UFRJ como parte dos requisitos necessários para a obtenção do grau de Doutor em Ciências (D.Sc.)

ESTIMATIVA DO COEFICIENTE DE TRANSFERÊNCIA DE CALOR INTERNO EM DUTOS USANDO O MÉTODO DO FUNCIONAL DE RECIPROCIDADE

Inoussa Tougri

Junho/2018

Orientadores: Marcelo José Colaço
Fabio Bozzoli

Programa: Engenharia Mecânica

Neste trabalho apresenta-se uma abordagem original de problema inverso baseada no Método do Funcional de Reciprocidade, acoplado à Técnica da Transformada Integral Clássica. A abordagem totalmente analítica é aplicada a um problema inverso tridimensional para estimar a distribuição interna do coeficiente de transferência de calor em dutos usando medições de temperatura na superfície externa do duto. A metodologia permite o uso de medições de temperatura de parede externa tanto em regime permanente quanto em transiente como dado de entrada. Para estimar o coeficiente de transferência de calor em um duto na abordagem aqui apresentada, são necessários dois problemas auxiliares: o primeiro está relacionado com a estimativa do fluxo de calor e o segundo com a estimativa da temperatura interna da parede. O coeficiente de transferência de calor por convecção é então calculado, uma vez que o fluxo de calor e a temperatura da parede interna são conhecidos. Tal metodologia inovadora evita a solução de sistemas lineares, reduzindo os custos computacionais que são consideráveis quando as abordagens tradicionais são aplicadas a problemas tridimensionais. O procedimento proposto é inicialmente verificado usando dados sintéticos de temperatura e depois validado usando medições reais de temperatura adquiridas por uma câmera infravermelha. Os resultados evidenciam que a metodologia é capaz de recuperar as funções desconhecidas em um tempo computacional baixo e com uma boa precisão, mesmo quando medidas de temperatura com ruídos são utilizadas.

Abstract of Thesis presented to COPPE/UFRJ as a partial fulfillment of the requirements for the degree of Doctor of Science (D.Sc.)

CONVECTION HEAT TRANSFER COEFFICIENT ESTIMATION IN DUCTS USING THE RECIPROCITY FUNCTIONAL METHOD

Inoussa Tougri

June/2018

Advisors: Marcelo José Colaço
Fabio Bozzoli

Department: Mechanical Engineering

In this work, we present an original inverse problem approach, based on the Reciprocity Functional Method coupled with the Classical Integral Transform Technique. This results in a fully analytical estimation approach, which is applied to a three-dimensional inverse problem to estimate the internal heat transfer coefficient distribution in ducts, using temperature measurements taken on the external boundary of the duct. The methodology allows the use of both steady-state and transient external wall temperature measurements as input data. To estimate the heat transfer coefficient in a duct, according to the proposed technique, two auxiliary problems are required: the first is related to the estimate of the heat flux and the second to the estimate of the internal wall temperature. The convection heat transfer coefficient is therefore calculated, since the heat flux and the internal wall temperature are known. Such innovative methodology, avoiding the solution of linear systems, reduces the computational cost that is considerable when traditional approaches are applied to three-dimensional problems. The proposed procedure is first verified adopting synthetic temperature data and then validated using real temperature measurements acquired by an infrared camera. The results highlighted that the presented methodology is able to recover the unknown functions in a very short computational time and with a good accuracy, even when the noisy temperature measurements are used.

Contents

List of Figures

List of Tables

List of Symbols

Symbol	Description	Unit
E_h	Estimation error	%
f	Orthonormal basis function	
g	Heat generated	W/m^3
h	Convective heat-transfer coefficient	$W/(m^2K)$
K	Thermal conductivity or Bessel third order function	W/(m.K) or $-$
L	Tube length	m
M, N	Integers related to the number of basis function	$-$
q	Convective heat flux	W/m^2
r	Radial coordinate	m
R	Residues	°C
Re	Reynolds number	$-$
S_0, S_1	Internal and external surface	m^2
T	Temperature	°C
x, y	Cartesian coordinates	m
Y	Measured temperature	°C
z	Axial coordinate	m
α	Linear coefficient related to the first auxiliary problem	$-$
β	Linear coefficient related to the second auxiliary problem	$-$
μ	Generic basis function in the first auxiliary problem	$-$
ξ	Generic basis function in the second auxiliary problem	$-$
σ	Standard deviation of the temperature measurements	°C
ε	Random variable	$-$
λ	Eigenvalues of an associated eigenvalue problem	$-$
Γ_0, Γ_1	Lateral surfaces	m^2
Ω	Domain of the physical problem	$-$
Φ	Harmonic test function in the first auxiliary problem	$-$
Ψ	Harmonic test function in the second auxiliary problem	$-$
θ	Angular coordinate	$-$

Subscripts, Superscripts

b	Bulk
env	Environment
$ext, 1$	External
$int, 0$	Internal
k, l, m, n	Integers
p, q, ν	Integers
$meas$	Measurement
opt	Optimal

Abbreviations

Abbreviations	**Meaning**
CITT	Classical Integral Transform Technique
CPU	Central Processing Unit
IHCP	Inverse Heat Conduction Problem
RAM	Random Access Memory
RFM	Reciprocity Functional Method
TRN	Thermal Resistance Network

Chapter 1

Introduction

1.1 Motivations and Objectives

Engineering is the field of research and development which applies a set of scientific theories in real life. In this context, the heat transfer analysis is important in various engineering applications. In fact, although thermal energy can be directly used in some applications, it is often transformed into other forms of energy through heat transfer. As such, heat can be transferred from one medium to another via conduction, convection or radiation. For example, in nuclear generation plants, the heat produced by the fission or, in some cases, nuclear fusion is transferred to the water by convection, producing steam which will move the turbine blades, generating electricity. Through a similar process, convection is also used in the electric energy production through the transformation of solar thermal energy. In this case, the solar irradiation is transformed into thermal energy, and through convection, the heat produced is transferred to a fluid that moves turbine blades, generating electricity. Convection processes are also very important in many engineering applications, such as thermal power plants, heat exchangers, oil pipelines, food pasteurization systems, etc. In most of these applications, it is necessary to know the spatial distribution of the heat transfer coefficient on the internal wall of some ducts. Therefore, a fundamental study of the different modes of heat transfer, including convection heat transfer, is of great interest for the industry. A convection process is generally a thermal interaction between a surface and a fluid in contact, which may be at rest or in motion, as in the case of fluid flow in pipes. However, convection can also occur between fluids of different temperatures when mixed.

There are several industrial applications where circular pipes are used, such as in heat exchangers and oil pipelines. Therefore, it is of great interest investigating the heat transfer mode that occurs between the inner surface of a circular duct and a fluid that is in contact with it. For this, it is necessary to measure the temperature

and the heat flux on this inner surface, and therefore calculate the heat transfer coefficient by convection. However, this task, which consists in making direct measurements, is not always possible for several reasons: the probes commonly used in thermal measurements may encounter problems of size; the surface may be inaccessible; or the medium in which the sensors are placed may be hostile to their proper functioning. Consequently, it is necessary to find an alternative, where measurements on the external surface can allow the calculation of the unknown quantities on the internal surface. A solution for this interesting issue can be obtained by formulating an Inverse Heat Conduction Problem (IHCP) in the bounding wall.

In general, IHCPs are complicated because they are ill-posed, which implies that they are highly sensitive to fluctuations in input data, such as those caused by experimental noise. Furthermore, the proper formulation of IHCP may also incur in truncation and round-off. To overcome these difficulties, many methods, based on experimental data processing, have been suggested and validated in the literature. Among these techniques we can cite:

1) gradient based methods [1];
2) methods based on Green's functions [2];
3) regularization techniques [3];
4) mollification algorithms [4];
5) Bayesian techniques [5, 6].

Generally, the solution of inverse problems requires a high computational time, especially when treating three-dimensional problems. In addition, the great variety of applications using circular tubes justify our interest in developing and improving methods that can reduce this computational time. It is in this sense that this work seeks to improve and use the Reciprocity Functional Method, which is a non-intrusive and non-iterative method for solution of linear Inverse Convection Heat Transfer Probelems (ICHTPs)[7, 8].

The main objective of this work is to calculate the internal convection heat transfer coefficient in a circular duct from temperature measurements on the external wall using the Reciprocity Functional Method in a three-dimensional analysis.

The Reciprocity Functional Method requires the solution of two auxiliary problems: the first one is used to calculate the normal temperature derivative on the internal surface; and the second one is used to calculate the internal surface temperature. From these two quantities we can calculate the heat transfer coefficient between the fluid and the internal surface of the duct. Preliminary results using steady-state measurements have been published by TOUGRI and COLAÇO [9] and TOUGRI *et al.* [8]. Similarly to the steady state analysis, the heat transfer coefficient was estimated through transient temperature data by TOUGRI *et al.* [10], based on the methodology used in TOUGRI *et al.* [11].

1.2 Thesis Organization

For a better understanding of the text and to guide the reader, this section presents the manuscript organization and highlights the main contents of each chapter. As such, this introductory chapter explored the motivations and relevance of this research, as well as introduce the main and specifics objectives.

Chapter 2 shows the literature review, where the background and the evolution of the Reciprocity Functional Method are presented. In this chapter, special mention has been made on inverse convection heat transfer from the works already done in the literature that have a direct or indirect relation with this work.

The following chapter, Chapter 3, describes the physical problem and the mathematical formulation of the direct problem, both in transient and steady-state regimes. It also highlights the solution method used for solving the heat transfer equation in three-dimensional circular ducts.

In Chapter 4, we focus on the proper formulation of the Reciprocity Functional Method. At first, the method is formulated to use steady state temperature data on the external wall of the duct. Then, the second part is dedicated to the formulation of the version of the method that allows transient temperature data on the external wall as input data.

The experimental apparatus is described in Chapter 5, showing how the thermography data have been acquired through an infrared camera.

Chapter 6 shows the main results and discussion of this research. In this chapter, the numerical verification of the Reciprocity Functional Method and the experimental application of the methodology hereby developed are presented.

Finally, Chapter 7 concludes this document by summarizing the main results and observations, and proposing futures works that can be developed from now on.

Chapter 2

Literature Review

2.1 Generalities on Inverse Problems

Tasks consisting of estimating or finding an unknown property of some object or medium by studying their response to a field (electric, thermal, magnetic, gravitational, etc.) or probing signal are called inverse problems. This interesting subject has various applications in science and engineering. Therefore, inverse problems are widely used in thermal engineering (heat flux estimation, thermal property identification of some materials, inaccessible boundary heat transfer coefficient estimation), biomedical engineering (computerized tomography), aerospace engineering, astrophysics and geophysics [12].

In thermal engineering, inverse problems consist mainly on the estimate of unknown terms through measurements of temperature, heat flux, radiation intensity and so on. Unfortunately, inverse problems are mathematically ill-posed in the sense that they are highly sensitive to small fluctuations in input data, such as those caused by the inevitable experimental measurements noises [6]. A problem is mathematically well posed when the existence, the uniqueness and the stability of the solution are satisfied [13]. Therefore, if at least one of these properties is not satisfied, the problem is called ill-posed. For a long time, inverse problems in heat transfer were considered as problems without solutions due to the instability and the non-uniqueness of the solutions. To overcome the ill-posed characteristics of inverse problems, several techniques have been developed such as gradient based methods [1], methods based on Green's functions [2], regularization techniques [3], mollification algorithms [4], and Bayesian techniques [5, 6].

Generally, the estimates obtained by the solution of inverse heat conduction problems are achieved through the minimization of an objective function formulated on the hypotheses that the errors are additive, have Gaussian distribution, and are uncorrelated with zero mean [12].

2.2 Reciprocity Functional Method

The fundamental ideas of the Reciprocity Functional Method started with the formulation of the Reciprocity Gap by ANDRIEUX and ABDA [14], based on the reciprocity theorem of Maxwell-Betti [15], to identify flaws in materials. Consider a continuous and homogeneous medium Ω, submitted to two fields $\mathbf{T}$ (temperature for example) and Φ (an arbitrary field), both in equilibrium. According to the reciprocity theorem of Maxwell-Betti, Eq.(2.1) hold, where $\mathbf{Y}$ and $\mathbf{q}$ are respectively, potential measurements and fluxes on the external boundary S of Ω.

$$\int_S \mathbf{q}\Phi dS = \int_S \mathbf{Y}\nabla\Phi.\mathbf{n}dS \tag{2.1}$$

Therefore, the existence of some inhomogeneity in the medium Ω leads to the non nullity of the reciprocity gap functional $\mathfrak{R}(\Phi_{|S}, \mathbf{Y})$, defined by ANDRIEUX and ABDA [14] as:

$$\mathfrak{R}(\Phi_{|S}, \mathbf{Y}) = \int_S (\mathbf{q}\Phi - \mathbf{Y}\nabla\Phi.\mathbf{n})\, dS \tag{2.2}$$

This approach is a very interesting tool for identifying failures. It allows the identification of linear flaws in a body. To determine a failure, knowing a field and its flux on the surface of the body, in steady-state regime, it is necessary to define an arbitrary field and its auxiliary flux, and then formulate the Reciprocity Functional Gap, which involves only boundary integrals of known terms [16]. Therefore the main purpose of this formulation is to make measurements in the contour of a body and then be able to determine the characteristics of its interior. After the formulation of the Reciprocity Functional Gap by ANDRIEUX and ABDA [14, 16], several works have been dedicated to the application of similar ideas to other physical problems.

Based on the Reciprocity Functional Gap, BANNOUR *et al.* [17] identified cracks in a body by developing a 3D reconstruction algorithm. The algorithm could identify cracks with some limitations, such as being planar in the case of three-dimensional reconstruction and segments in the case of two-dimensional reconstruction.

As the previous works [14, 16, 17] were already able to identify the existence of cracks in a body, ABDA *et al.* [18] used the Reciprocity Functional Gap to identify the shape and the location of planar failures. Using the same idea, COLTON and HADDAR [19] combined the linear sampling method and the Reciprocity Functional Gap to identify the shape of an object buried in a body, such as earth, through measurement on its surface. By the same way it was possible to detect cancer in a human body such as breast cancer [20]. The Reciprocity Functional Gap has being used in a variety of works dealing with cracks and defects identification. Among them we can cite the work of ALVES *et al.* [21] and SHIFRIN and SHUSHPANNIKOV [22].

ROBERTY and ALVES [23] presented a methodology for shape reconstruction of an unknown characteristic source enclosed in a domain, based on the Reciprocity Functional. They considered a heat conduction problem in steady-state regime, where the heat source was the non-homogeneous characteristic function. In order to reconstruct the source shape, the Reciprocity Functional was used. The authors also formulated a numerical method based on an algebraic non-linear system of equations, which allowed the estimate of the boundary of the unknown source.

The formulation of the Reciprocity Functional Gap [14] was fundamental to the development of a non-intrusive inverse problem technique by COLAÇO and ALVES [24] in the field of thermal engineering, called Reciprocity Functional Method, to estimate thermal contact resistances between two materials. The methodology is very fast since it is non-iterative. The requirement was the solution of two auxiliary problems, which involved Cauchy boundary conditions. Therefore, to solve the direct problem and the subsequent auxiliary problems, the Method of Fundamental Solutions was used. The first auxiliary problem allowed the estimate of the temperature gradient in the contact interface and the second problem allowed the estimation of the temperature gap. Then, combining the temperature gradient and the temperature gap at the interface of the two materials, it was possible to estimate the thermal contact resistance.

In order to overcome the problems related to the Cauchy boundary condition appearing in the formulation of the Reciprocity Functional Method by COLAÇO and ALVES[24], ABREU *et al.* [25] developed a new version that removed the Cauchy boundary conditions. The methodology was used to estimate thermal contact resistances between two materials using temperature measurements without noise. The results were compared to those obtained by COLAÇO and ALVES[24] with good agreement.

PADILHA *et al.* [26] combined the Reciprocity Functional Method, formulated by ABREU *et al.* [25], with the Classical Integral Transform Technique (CITT) to estimate one-dimensional thermal contact conductances. The auxiliary problems were solved by CITT and, by choosing an adequate set of orthogonal basis, it was possible to reduce the resulting matrices of the linear systems appearing in the formulation into diagonal matrices. This strategy allowed an explicit expression of the thermal contact conductance, reducing significantly the computational time.

COLAÇO *et al.* [27] and COLAÇO and ALVES[28] developed a transient version of the Reciprocity Functional Method, where integrals involving transient terms appeared.

To reduce the computational time required to the transient estimate, TOUGRI *et al.* [11] formulated a transient Reciprocity Functional analysis based on the work of COLAÇO *et al.* [27], where the 3D integrals involving transient terms were trans-

formed into boundary integrals through the double application of the Reciprocity Functional. This modification removed the need for solving the direct problem in an iterative way, turning the method non-iterative. Therefore, the computational time was significantly reduced. The method was used to estimate thermal contact conductance with good accuracy, even when noisy temperature measurements were present. The results showed that it was possible to recover thermal contact conductances using a small number of measurements, without the need to reach the steady-state regime.

As the Reciprocity Functional Method has shown its ability to estimate, with quite satisfactory results, the thermal contact resistance between two bodies or identifying failures in a body, it has been used in some other works to estimate the heat transfer coefficient in circular ducts such as the work of COLAÇO *et al.* [7], TOUGRI and COLAÇO[9], TOUGRI *et al.* [8], TOUGRI *et al.* [10] and MOCERINO *et al.* [29].

2.3 Heat Transfer in Circular Ducts

The enhancement of convection processes in ducts has been a very interesting research topic in the heat transfer community [30, 31]. In fact, the use of convection processes has several applications in the industry, mainly as a tool to improve and take advantage of thermal energy. Heat exchangers are an example of an industrial application. Heat exchangers are found in a wide variety of geometries according to the application where they are required. Several studies, both experimental and computational, were made regarding techniques for improving convection heat transfer coefficient in circular ducts. Some industrial applications do not allow direct thermal measurements on the internal boundary of ducts, and, therefore, it is necessary to develop some estimation techniques. In this section we will show some works related to heat transfer in ducts, starting by works carried out with the objective of improving the convection until experimental measurements used for convection coefficient estimates through the solution of an inverse problem.

RAINIERI *et al.* [32] conducted an experimental investigation on forced convection heat transfer in straight and coiled tubes with smooth or corrugated inner walls. In their investigation, two fluids were used for two different ranges of Reynolds numbers. Glycerol was used for Reynolds numbers varying from 5 to 13, while Ethylene Glycol was used for the range between 15 and 1500. The objective of the work was to verify the passive heat transfer improvement techniques, when high viscosity fluids are used in ducts. Two types of straight tubes were used: tubes with smooth inner walls and tubes with corrugated inner walls. The results related to the use of glycerol as working fluid showed that for the lower Reynolds number the roughness

of the inner wall does not bring any benefit to the improvement of the convection coefficient. However, for high Reynolds numbers, the presence of roughness increased convection. Concerning coiled tubes, where the roughness was also tested, it was shown that the curvature of the tube with smooth inner wall causes a secondary flow to appear near the inner wall at the outside of the curvature due to the centrifugal forces. This phenomenon increased the convection rate in these areas. Under the same experimental conditions, results showed that with the roughened inner wall tube, the roughness removed the previously observed curvature effect. Therefore, the combination of roughness and curvature is not beneficial to the improvement of convection when high viscosity fluids are used. The curvature effect is already sufficient to improve the convection heat transfer coefficient compared to straight tubes. However, for Reynolds number up to 1000, the roughness began being beneficial, making the curvature-roughness combination advantageous.

In another work, RAINIERI *et al.* [33] continued their previous research [32] to further investigate the effect of the curvature-roughness combination on the heat transfer coefficient in ducts. When dealing with flow in the curved tubes, a dimensionless parameter, called Dean number is important. The Dean number is the product of the Reynolds number by the square root of the curvature ratio ($De = Re\sqrt{\delta}$). Therefore it caracterizes flow in coiled tubes. The investigation was made for the following ranges of Reynolds and Dean numbers: $70 \leq Re \leq 1200$ and $12 \leq De \leq 290$. The procedure adopted was to mantain the roughness fixed and test different values of the curvature ratio. The results showed that for low values of Dean number, the curvature effects are more important than the roughness effects. However, for high values of Dean number, the effects of roughness predominated, because reducing curvature ratio increases the appearance of the secondary flow. A critical value of $De = 120$ was found during the experiment. The authors found some correlations such as: for smooth inner wall tubes the relation $Nu = 1.168De^{0.47}Pr^{0.16}$ held for $12 \leq De \leq 280$ and $125 \leq Pr \leq 280$; while for rough inner wall pipes $Nu = 0.0191De^{1.36}Pr^{0.2}$ is valid for $120 \leq De \leq 290$ and $125 \leq Pr \leq 280$.

HUANG and CHEN [34] used the Conjugate Gradient Method (CGM) combined with the commercial software CFX-4.2 to estimate transient boundary heat flux in an irregular duct domain using synthetic temperature measurements acquired with sensors. Several duct shapes, duct thicknesses, inlet velocities, measurement errors and heat fluxes were investigated. The results highlighted that the solution remains stable and regular even when the noise in the measurements increased. The accuracy of the method regarding the boundary fluxes estimate was good, except for the inlet surface and final time.

BOZZOLI *et al.* [35] estimated the local heat transfer coefficient in coiled tubes through the Tikhonov regularization method in laminar flow. The procedure was

based on the solution of an inverse heat transfer problem in which the temperature field on the outer surface of the tube was the input data. The axial temperature gradient was neglected, so the problem was reduced to a 2D problem. Thus, the direct problem consisted in solving the energy equation in a section with convective boundary condition on the external surface of the tube and prescribed heat flux on the internal wall. The inverse problem consisted in estimating the heat flux through the temperature field on the outer surface, measured with an infrared camera. With the estimated heat flux, the convection coefficient was easily deduced due to fact that the value of the internal wall temperature was assumed to be known. Inverse problems are generally ill-posed, so it was necessary to use a regularization method to obtain a stable solution. Therefore, the Tikhonov regularization technique was used to estimate the local convection heat transfer coefficient with good accuracy by following the methodology developed by BAZAN and FRANCISCO[36] to choose the regularization parameter iteratively. The authors used their methodology to verify the experimental investigation in the work of RAINIERI *et al.* [33].

BOZZOLI *et al.* [37] adopted the filtering method to estimate the local convection coefficient in a duct. The duct used for the experiment had a thin thickness in such a way that it was possible to assume the hypothesis of concentrated parameters in the radial direction (due to Biot number being less than 0.1). Therefore, the temperature gradient was neglected in that direction, and the duct external surface temperature was taken as being equal to the internal surface temperature. Considering the Biot hypothesis in the radial direction and analizing the local energy balance in steady state in a volume element in the cylindrical coordinates, they formulated an explicit expression of the internal convection coefficient. This expression contained the Laplacians of the temperature in the angular and axial direction, making the problem highly sensible to small perturbations. It was necessary to filter the temperature data measured by an infrared camera to obtain a good accuracy in estimating the convection heat transfer coefficient. In fact, the filtering approach removed unwanted noises from the temperature measurements. Numerical temperature measurements on the external surface, with different internal convection profiles, were also used to estimate the heat transfer coefficient and the results showed a good agreement compared to the exact values.

YANG *et al.* [38] developed a thermo-elastic hyperbolic inverse problem to calculate thermal stresses and heat fluxes on the internal wall of a circular duct. The inverse problem, based on the conjugate gradient method, was formulated as an optimization problem together with the discrepancy principle. Numerical temperature measurements on the same inner wall of the duct were adopted as the input data to the method. The results regarding transient heat fluxes on the inner wall and temperature stresses within the duct were good.

An IHCP was solved in[39] to determine the heat flux on the outer surface of a control bar of a nuclear power plant. The control bar was modeled as a hollow cylinder in which circulated a fluid with high pressure and temperature. The objective was to develop a simple method to determine the heat flux temporal distribution on the external surface from its temperature measurements near the fluid-solid interface. The results were accurate compared to experimental data.

LU *et al.* [40] solved an inverse 2-D conduction problem to simultaneously estimate the convection coefficient, the bulk fluid and the internal wall temperature of an oil pipeline using temperature measurements on the external surface of the pipeline. The Finite Element Method was used to solve the direct problem, while the conjugate gradient method was used to solve the inverse problem. A cross-section of the pipeline was considered and four external temperature measurement points, located at 0^0, 90^0, 180^0 e 270^0, were used. The results were accurate to the analysis of the residual where the maximum value was less than 1%. The authors suggested to increase the number of sensors and to model the problem in three-dimensions to improve the results.

COLAÇO *et al.* [7] used the Reciprocity Functional Technique [14, 24, 26] to estimate the heat transfer coefficient in a duct. A 2D inverse conduction problem with heat generation in the whole domain was considered in their work [7]. Furthermore, the physical properties were supposed constants and known and the temperature of the fluid in contact with the internal wall was also considered known. The Reciprocity Functional Technique required only temperature measurements on the external wall to estimate the internal heat transfer coefficient. The methodology was verified numerically using synthetic temperature measurements by recovering different profiles for the heat transfer coefficient with good accuracy. Then, real temperature measurements, obtained through a thermographic camera, were also used to evaluate the technique's performance.

MIN *et al.* [41] presented a simplified conjugate gradient method to localize and calculate the distance between square ribs in a channel through the analysis of the estimated heat transfer on the channel wall. The results showed that the method was accurate and could be used to locate the optimal pitch ratio of the ribs. Nevertheless, the authors concluded that a three-dimensional analysis could be more meaningful.

DHIMAN and PRASAD [42] presented an inverse conduction problem, based on Levenberg-Marquardt approach for parametric estimation, to determine the surface heat flux of an initially heated cylinder under the cross-flow of air. To estimate the internal heat flux, temperature measurements were taken at some strategic points located in the cylinder using thermocouple. The heat flux was parameterized using some unknown trial functions, and the unknown parameters were determined by minimizing an ordinary-least-square norm. The methodology required also a sen-

sitivity analysis. The results regarding the heat transfer estimated by the method were considered good, since the average deviation was less than 1% compared to data available in the literatures.

NOH *et al.* [43] formulated a 3D IHCP to estimate a transient heat flux on the internal surface of a two-layer cylindrical duct using the Kalman filter. The first layer was made of chromium and the second of steel. The following assumptions were considered: the properties of both materials were constant and there was perfect thermal contact between the layers. Numerical external temperature measurements, obtained by a commercial software, were used as input data to the IHCP solution. However, the Thermal Resistance Network (TRN) method was adopted to solve the direct problem, which is part of the inverse problem technique, to reduce the computational time required for the estimate. Results regarding different profiles for the transient internal heat fluxes were good.

TOUGRI and COLAÇO [9] presented a three-dimensional version of the Reciprocity Functional Method used by COLAÇO *et al.* [7] to estimate the heat transfer coefficient in a duct using only synthetic temperature data. The methodology was verified using noisy temperature data as well as recovering complex heat transfer distributions. In order to overcome the ill-posed character of the problem, the Singular Value Decomposition (SVD) method was used. The results presented were satisfactory despite the massive computational costs principally due to the solution of some linear systems of equations.

TOUGRI *et al.* [8], based on the PADILHA *et al.* [26], with the main objective to overcome the computational time observed in [9], combined the Reciprocity Functional Method (RFM) and the Classical Integral Transform Technique (CITT) to estimate the heat transfer coefficient in a three-dimensional duct. The auxiliary problems, which appeared in the formulation of the method, were solved using CITT and the choice of an adequate orthonormal basis functions allowed an explicit expression of the heat transfer coefficient distribution. Only external wall temperature data were required for the estimate. Different heat transfer coefficient profiles were recovered using synthetic temperature measurement without noise, as well as noisy temperature measurements with good accuracy. In addition, real temperature measurements with an infrared camera were used to validate the robustness of the method.

The Reciprocity Functional Method, combined to the Filtering Approach and the Classical Integral Transform, was used by MOCERINO *et al.* [29] to estimate the internal heat transfer coefficient in a 2D duct. The use of CITT allowed a completely analytical solution, which significantly reduced the computational time required for the solution. Results showed that filtering the measurements noise increased the accuracy of the solution. Different synthetic profiles of the heat transfer

coefficient were recovered and solutions obtained by using the Truncated Singular Value Decomposition (TSVD) method were obtained with good accuracy. Real temperature measurements, obtained with a thermographic camera, were also used to test the robustness of the method.

There are several other works [44–49] in the literature dealing with heat transfer in circular ducts to estimate the heat flux, the temperature, or the convection coefficient on the internal surface of the duct. Inverse methods are used in most of the works and one of the main objectives is to develop some simple algorithms with low computational costs. However, most of them are either iterative or 2-D [7, 29]. Therefore, developing a faster 3-D non-iterative inverse problem method to estimate the spatial distribution of the heat transfer coefficient in circular ducts is a great contribution in thermal science.

2.4 Contribution of the Thesis

The literature review has shown the lack of fast inverse problem techniques able to accurately estimate the heat transfer coefficient in 3-D circular ducts through temperature measurements on the external wall. Therefore, the contribution of this thesis is the development of the Reciprocity Functional Method to estimate heat transfer coefficient in 3-D ducts using only temperature data on the external boundary. The algorithms developed in this work allow also the use of transient external temperature measurements to recover the internal transfer coefficient with good accuracy.

Concerning the steady state analysis of this work, TOUGRI and COLAÇO [9] presented a three-dimensional Reciprocity Functional analysis to estimate the heat transfer coefficient in a duct using only synthetic temperature data on the external surface. To overcome the ill-posed nature of the formulated inverse problem, the Singular Value Decomposition (SVD) method was used to solve it. Despite the massive computational costs, the results presented were satisfactory. To reduce the computational cost observed in [9], which was principally due to the solution of some linear systems of equations, TOUGRI *et al.* [8] combined the Reciprocity Functional Method (RFM) and the Classical Integral Transform Technique (CITT) to calculate the heat transfer coefficient in three-dimensional ducts. The method required only the temperature data on the outer wall of the tube to estimate the heat transfer coefficient on the inner wall. The methodology was numerically verified and real temperature measurements with an infrared camera were used to validate the robustness of the method.

For the transient estimate, TOUGRI *et al.* [10] based on the work of TOUGRI *et al.* [11], formulated a Time Depending Reciprocity Functional Method, also com-

bined with the CITT, to estimate heat transfer coefficients in three-dimensional ducts, using transient temperature measurements taken on the external wall.

Chapter 3

Physical Problem and Solution of the Direct Problem

3.1 Physical Problem Description

In this work, the physical model is a cylindrical tube in which we have some fluid flow. The tube is subjected to heat transfer by convection on both internal and external walls. This kind of situation is found in many engineering applications such as refrigeration devices, heat exchangers, oil pipelines, etc. Therefore, a hollow cylinder is used to represent the physical problem in this work as it is shown on Fig.3.1.

The hollow cylinder considered here has a length L, an internal radius r_0 and an external radius r_1. The surfaces Γ_0 and Γ_1 of the cylinder, respectively at $z = 0$ and $z = L$, are maintained insulated, while the curved walls (internal and external) S_0 and S_1 are subjected to convection heat transfer with heat transfer coefficients h_0 and h_1 respectively. The external environment temperature is T_{env} and the internal fluid temperature is T_b. Given the boundary conditions and the heat source $g(r, \theta, z)$ in the entire domain, the goal of the direct problem is to find the temperature profile in the whole domain.

3.2 Mathematical Formulation of the Physical Problem

The physical problem, as described above, can be modelled as a heat conduction equation [50]. As in this work we are interested both in steady and transient regimes, the mathematical formulation presents both cases. In steady-state analysis, Eq.(3.1) represents the mathematical formulation, while Eq.(3.2) describes the mathematical formulation of the problem hereby stated in transient regime. The coefficient K is

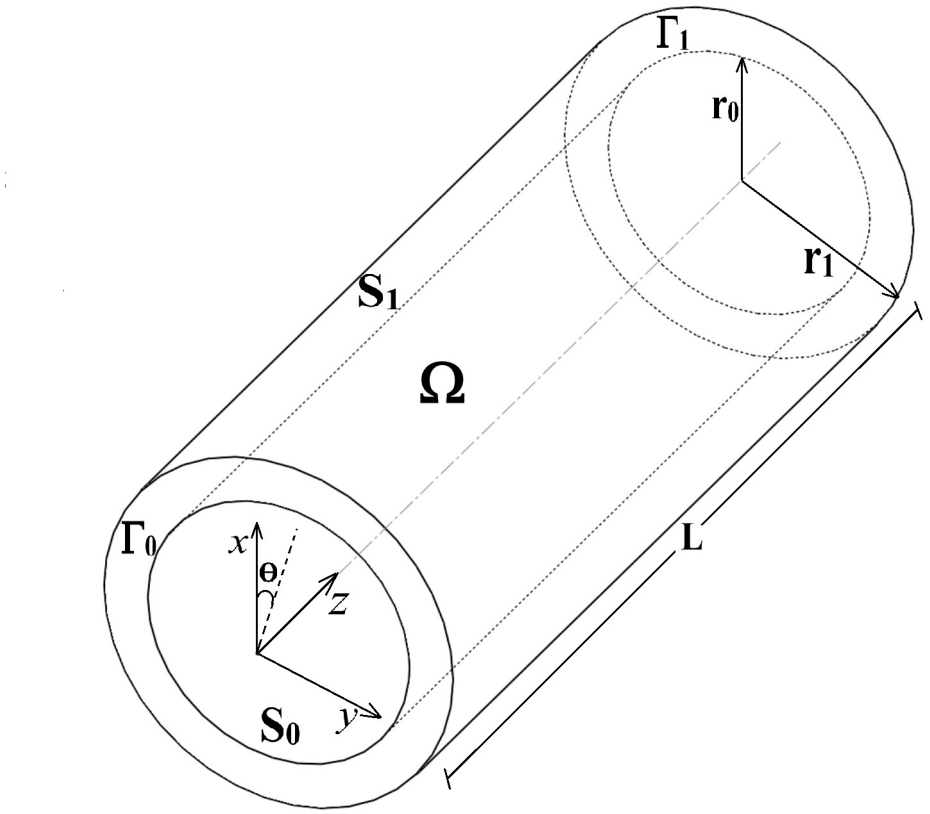

Figure 3.1: Physical geometry

the thermal conductivity of the hollow cilinder.

$$\nabla^2 T = -\frac{g}{K} \qquad \text{in} \quad \Omega \tag{3.1a}$$

$$-K\frac{\partial T}{\partial \mathbf{n}} = h_0(T - T_b) \qquad \text{on} \quad S_0 \tag{3.1b}$$

$$-K\frac{\partial T}{\partial \mathbf{n}} = h_1(T - T_{env}) \qquad \text{on} \quad S_1 \tag{3.1c}$$

$$\frac{\partial T}{\partial \mathbf{n}} = 0 \qquad \text{on} \quad \Gamma_0 \tag{3.1d}$$

$$\frac{\partial T}{\partial \mathbf{n}} = 0 \qquad \text{on} \quad \Gamma 1 \tag{3.1e}$$

$$\frac{1}{\alpha}\frac{\partial T}{\partial t} = \nabla^2 T + \frac{g}{K} \qquad \text{in} \quad \Omega \tag{3.2a}$$

$$-K\frac{\partial T}{\partial \mathbf{n}} = h_0(T - T_b) \qquad \text{on} \quad S_0 \tag{3.2b}$$

$$-K\frac{\partial T}{\partial \mathbf{n}} = h_1(T - T_{env}) \qquad \text{on} \quad S_1 \tag{3.2c}$$

$$\frac{\partial T}{\partial \mathbf{n}} = 0 \qquad \text{on} \quad \Gamma_0 \tag{3.2d}$$

$$\frac{\partial T}{\partial \mathbf{n}} = 0 \qquad \text{on} \quad \Gamma 1 \tag{3.2e}$$

$$T(r, \theta, z, t = 0) = T_0 \qquad \text{in} \quad \Omega, \quad \text{for} \quad t = 0 \tag{3.2f}$$

3.3 Solution of the Direct Problem

The direct problem in this work consists in determining the temperature profile in the entire tube, solving the equations presented in the previous section. The main goal of the direct problem in this work is to generate simulated temperature measurements, which are taken as the input data for inverse problem solution. It is important to highlight that the direct problem is not necessary if temperature measurements are available. The inverse methodology developed in this work does not require the solution of the direct problem as part of its formulation. Therefore, for real experiments, no direct problem solution is needed to estimate the convection heat transfer coefficient in a tube through the inverse problem algorithm developed in this work. However, for synthetic temperature measurements, the direct problem is solved in steady and transient regime to generate these input data.

To solve the direct problem in transient regime, Eq.(3.2) was numerically discretized using the Alternating Direction Implicit (ADI) Finite Difference method [51–55]. The ADI method is based on a scanning in different directions of space using the implicit scheme successively, while the other directions are discretized explicitly. In this way, the Thomas and Thomas cyclic algorithm can be applied at each time step, since the discretization leads to a tridiagonal system in the radial and longitudinal directions, and to a tridiagonal cyclic system in the angular direction. It is worth notifying that this method, applied to a three-dimensional problems, is conditionally stable. The stability is guaranteed when the condition (3.3) is satisfied [53].

$$\left[\frac{\alpha\Delta t}{\Delta r^2} + \frac{\alpha\Delta t}{(r\Delta\theta)^2} + \frac{\alpha\Delta t}{\Delta z^2}\right] \leq \frac{3}{2} \tag{3.3}$$

Therefore, the grid convergence was achieved while remaining in the limit of the stability. The conditional stability of the ADI method, when applied to a three-

dimensional problems makes it very time consuming to reach the steady-state regime via a transient simulation. Computational time would be higher than programming a suitable method for this type of problem. Due to this reason, the Gauss-Seidel method [52, 54, 55], which is an appropriate iterative method for this type of problem was used to solve the direct problem in steady-state. In addition to the over relaxation, the use of the line-by-line Gauss-Seidel algorithm improved considerably the computational time. This gain, in terms of computational time, is due to the fact that the line-by-line Gauss-Seidel method admits the use of Thomas algorithm. In this case, the equations were discretized following the centered differences scheme. The convergence was achieved when the condition (3.4) was verified, where ε is a small number. In this criteria, j the iteration number.

$$E = \frac{\| \mathbf{T}^{j} - \mathbf{T}^{j-1} \|}{\| \mathbf{T}^{j-1} \|} \leq \varepsilon \tag{3.4}$$

3.4 Code Verification

The computational code used for solving the direct problem in this work was fully developed in FORTRAN 90. In order to verify this code, some test cases were compared to results obtained by COMSOL Multiphysics. A constant internal heat transfer coefficient (h_0) was used to solve Eqs.(3.1) and (3.2). Tab.3.1 shows the tube dimension and the parameters used for this verification. The bulk temperature T_b and the environment temperature T_{env} were considered equal to 20 ^oC. The mesh was refined until its convergence and the solutions were compared to the COMSOL Multiphysics simulation in the same conditions with regular mesh.

Table 3.1: Geometry data and parameters used to verify the computational code

r_0[m]	r_1[m]	L[m]	h_0[W/(m^2 ^{o}C)]	h_1[W/(m^2 ^{o}C)]	g[W/m^3]	K[W/(m ^{o}C)]
0.02	0.03	0.2	600	5	10^6	15

Starting with the steady-state solution, Fig.3.2 shows the temperature distribution in the whole domain calculated by the Finite Difference Method [51, 53], while Fig.3.3 shows the solution obtained by COMSOL Multiphysics. The solutions are almost the same; however, in order to better analyze the agreement between the simulations, the relative errors were computed. Fig.3.4 shows that the maximum error between the solution obtained by the Finite Difference Method and the one obtained by the COMSOL Multiphysics is less than 0.4%.

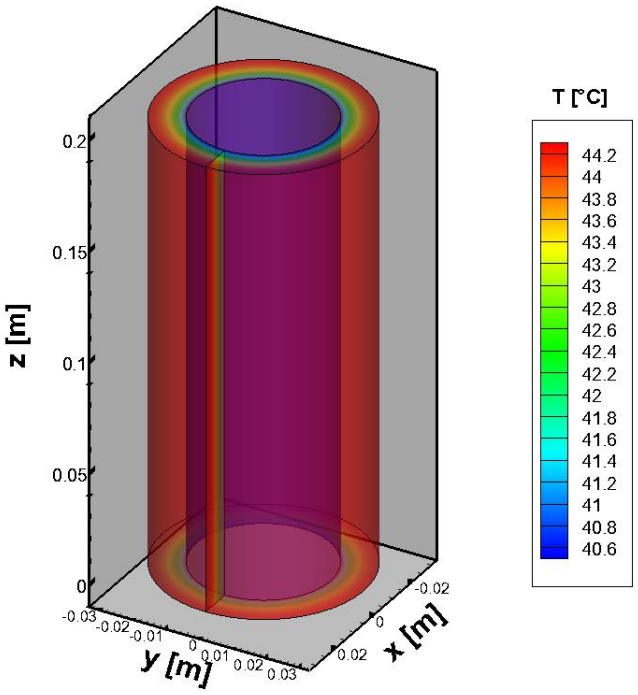

Figure 3.2: Temperature profile in steady-state calculated by the Finite Difference Method

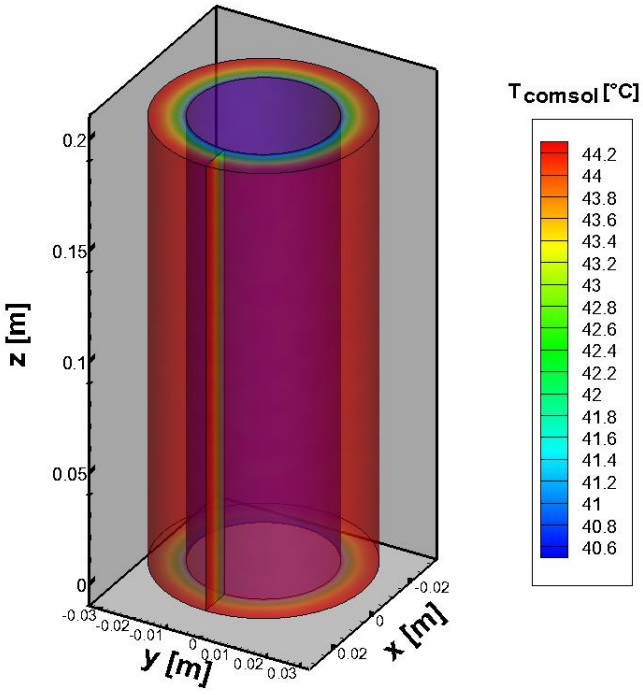

Figure 3.3: Temperature profile in steady-state calculated by COMSOL Multiphysics

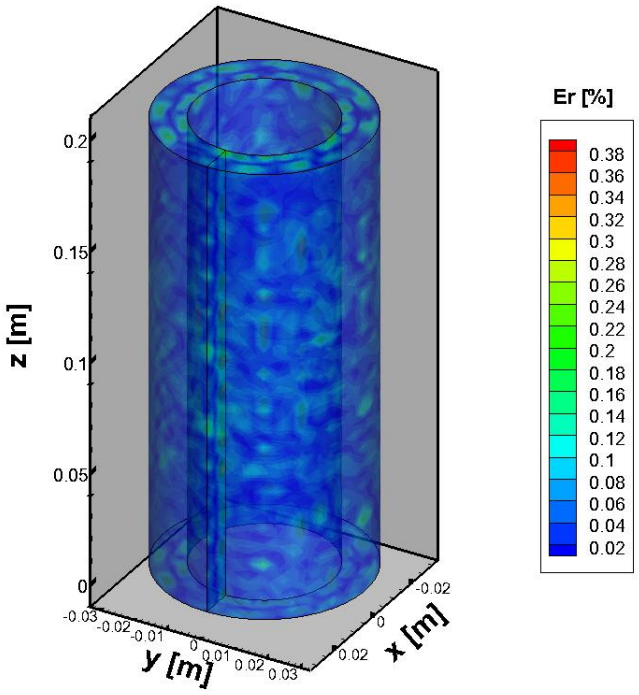

Figure 3.4: Relative Errors between Finite Difference Method and COMSOL Multiphysics

Similarly to the steady-state, the transient code was also verified comparing its solution to the one calculated by COMSOL Multiphysics. In both simulations, the time step Δt used was 10^3 second. Fig.3.5 shows the temperature profile in the tube calculated by the Finite Difference Method, while Fig.3.6 shows the solution obtained by the COMSOL Multiphysics. The solutions are also in good agreement, since the maximum error between them is less than 1.4%, as it can be seen in Fig.3.7.

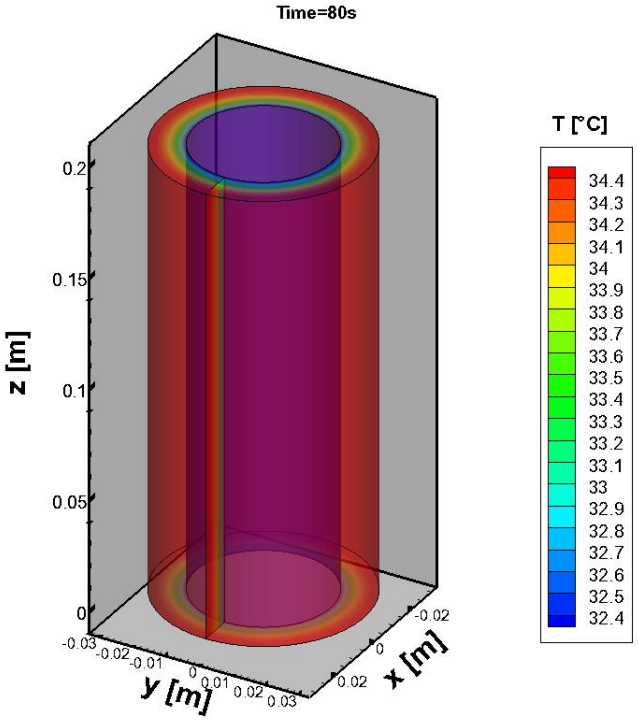

Figure 3.5: Temperature profile calculated by Finit Difference Method at 80 seconds

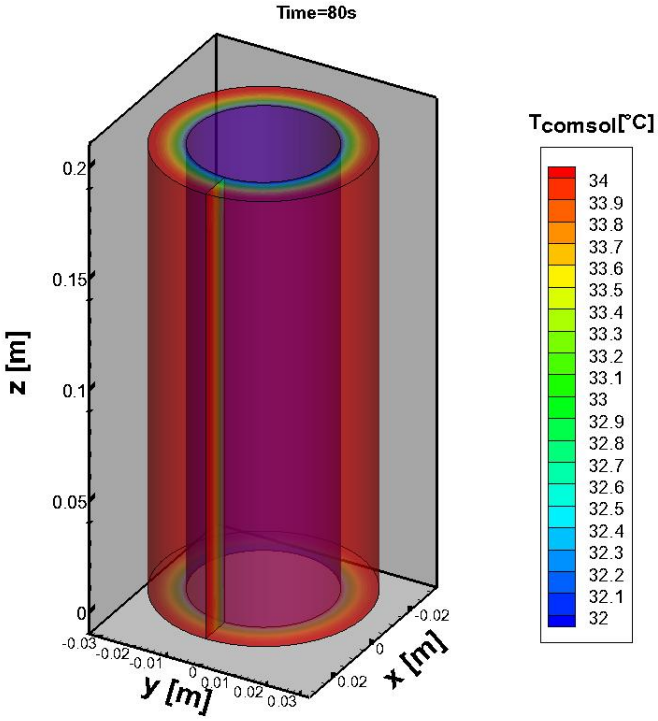

Figure 3.6: Temperature profile calculated by COMSOL Multiphysics at 80 seconds

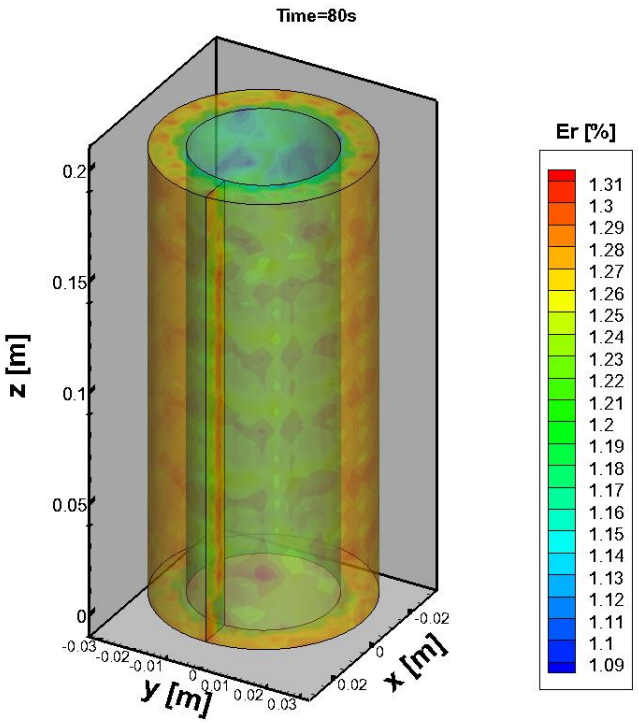

Figure 3.7: Relative Errors between Finit Difference Method and COMSOL Multiphysics at 80 seconds

Chapter 4

Inverse Problem

For the inverse problem considered in this work, the temperature distribution on the external wall S_1 (see Fig.3.1) is considered to be known and the internal wall heat transfer coefficient distribution h_0 has to be estimated. Three cases are considered in this work:

• (i) steady state synthetic temperature data, obtained by the solution of the direct problem given by Eqs.(3.1) with a known distribution of the heat transfer coefficient;

• (ii) steady state real experimental temperature measurements acquired by an infrared camera;

• (iii) transient synthetic temperature data, obtained by the solution of the direct problem given by Eqs.(3.2) with a known distribution of the heat transfer coefficient.

The Reciprocity Functional Method [7–11, 26], used in this work, requires two auxiliary problems as shown in Eqs.(4.1) and (4.2). One is used to estimate the internal heat flux and the other for estimating the internal surface temperature.

The functions $f_p(\theta, z)$, appearing on Eqs.(4.1c) and (4.2c), are a set of orthonormal basis functions on the external radius of the duct. Eq.(4.3) shows how these functions are constructed. In order to take advantage of the orthogonality properties of the functions appearing in Eqs.(4.1c) and (4.2c), the Classical Integral Transform Technique (CITT) [50] can be used to solve Eqs.(4.1) and (4.2), as it will be shown next. The internal heat transfer coefficient (h_0) will be obtained by supposing available the thermal conductivity K of the material and the bulk temperature T_b of the fluid.

$$\nabla^2 \Phi_p = 0 \qquad \text{in} \quad \Omega \tag{4.1a}$$

$$\frac{\partial \Phi_p}{\partial \mathbf{n}} = 0 \qquad \text{on} \quad S_0 \tag{4.1b}$$

$$\Phi_p = f_p(\theta, z) \qquad \text{on} \quad S_1 \tag{4.1c}$$

$$\frac{\partial \Phi_p}{\partial \mathbf{n}} = 0 \qquad \text{on} \quad \Gamma_0 \tag{4.1d}$$

$$\frac{\partial \Phi_p}{\partial \mathbf{n}} = 0 \qquad \text{on} \quad \Gamma 1 \tag{4.1e}$$

$$\nabla^2 \Psi_p = 0 \qquad \text{in} \quad \Omega \tag{4.2a}$$

$$\Psi_p = 0 \qquad \text{on} \quad S_0 \tag{4.2b}$$

$$\Psi_p = f_p(\theta, z) \qquad \text{on} \quad S_1 \tag{4.2c}$$

$$\frac{\partial \Psi_p}{\partial \mathbf{n}} = 0 \qquad \text{on} \quad \Gamma_0 \tag{4.2d}$$

$$\frac{\partial \Psi_p}{\partial \mathbf{n}} = 0 \qquad \text{on} \quad \Gamma 1 \tag{4.2e}$$

4.1 Complete Orthonormal Basis

The functions used on Eqs.(4.1c) and (4.2c) need to form a complete orthonormal base system in $L^2(S_1)$ [7] as it will be shown during the derivation of the analytical treatment of the Reciprocity Functional approach. Such a basis is a Hilbert's basis [56]. It should be noticed that the product of systems of orthonormal and complete functions leads to a system of orthonormal and complete functions [56]. Thanks to this property of Complete Orthonormal System, we can combine two one-dimensional basis functions to construct the two-dimensional basis function f appearing in the auxiliaries problems above mentioned. The first is a function of the angular variable θ and the second is a z depending function. Therefore, using a Complete Orthonormal System (CON) in $L^2(0, 2\pi)$ and another CON in $L^2(0, L)$, one can construct a Complete Orthonormal System in $L^2(S_1)$. Hence, the orthonormal and complete set of functions f_p shown by Eq.(4.3) is constructed by multiplying a CON of functions f_k in $L^2(0, 2\pi)$ by a CON of functions f_l in $L^2(0, L)$ such as $f_p = f_k \otimes f_l$ [56].

$$f_{p=0,1,..,N_\theta N_z}(\theta,z) = f_{k=0,1,..,N_\theta}(\theta) f_{l=0,1,..,N_z}(z) \tag{4.3a}$$

$$\Rightarrow \left\{ \begin{array}{r} f_0(\theta,z) \\ f_1(\theta,z) \\ f_2(\theta,z) \\ ... \\ f_{N_\theta}(\theta,z) \\ f_{N_\theta+1}(\theta,z) \\ f_{N_\theta+2}(\theta,z) \\ f_{N_\theta+3}(\theta,z) \\ ... \\ ... \\ f_{N_\theta N_z-1}(\theta,z) \\ f_{N_\theta N_z}(\theta,z) \end{array} \right\} = \left\{ \begin{array}{c} f_0(\theta)f_0(z) \\ f_0(\theta)f_1(z) \\ f_0(\theta)f_2(z) \\ ... \\ f_0(\theta)f_{N_z}(z) \\ f_1(\theta)f_0(z) \\ f_1(\theta)f_1(z) \\ f_1(\theta)f_2(z) \\ ... \\ ... \\ f_{N_\theta}(\theta)f_{N_z-1}(z) \\ f_{N_\theta}(\theta)f_{N_z}(z) \end{array} \right\} \tag{4.3b}$$

Following HIGGINS [56], and considering an interval $[a,b]$; $\forall\ a,b \in \mathbb{R}$, the following sequences or a combination of these sequences forms an Orthonormal and Complete basis in $L^2(a,b)$:

$$\left\{ \left(\frac{2}{b-a}\right)^{\frac{1}{2}} \sin\left[n\pi\frac{(x-a)}{(b-a)}\right], ... \right\} \qquad n = 1,2,3,.....\forall x \in [a,b] \tag{4.4}$$

$$\left\{ \left(\frac{1}{b-a}\right)^{\frac{1}{2}}, \left(\frac{2}{b-a}\right)^{\frac{1}{2}} \cos\left[n\pi\frac{(x-a)}{(b-a)}\right], ... \right\} \qquad n = 1,2,3,.....\forall x \in [a,b] \tag{4.5}$$

4.2 Reciprocity Function Analysis for Estimating the Internal Heat Flux through Steady Temperature Data on the External Boundary

In order to estimate the internal heat flux, the Reciprocity Functional Method, formulated according to the references [7–11, 26], was adopted in this work. Similarly to the procedure presented in TOUGRI *et al.* [8] and COLAÇO *et al.* [7], we can multiply Eq.(3.1a) by Φ_p and Eq.(4.1a) by (-T), and the sum of the resulting equations can be integrated over the entire domain Ω in order to obtain:

$$\int_\Omega \left(\Phi_p \nabla^2 T - T\nabla^2\Phi_p\right) d\Omega = \int_\Omega \left(-\Phi_p \frac{g}{K}\right) d\Omega \tag{4.6}$$

Using Green's second identity, Eq.(4.6) becomes:

$$\begin{aligned}&\int_{S_0}\left(\Phi_p\tfrac{\partial T}{\partial \mathbf{n}}-T\tfrac{\partial \Phi_p}{\partial \mathbf{n}}\right)dS_0+\int_{S_1}\left(\Phi_p\tfrac{\partial T}{\partial \mathbf{n}}-T\tfrac{\partial \Phi_p}{\partial \mathbf{n}}\right)dS_1+\\&+\int_{\Gamma_0}\left(\Phi_p\tfrac{\partial T}{\partial \mathbf{n}}-T\tfrac{\partial \Phi_p}{\partial \mathbf{n}}\right)d\Gamma_0+\int_{\Gamma_1}\left(\Phi_p\tfrac{\partial T}{\partial \mathbf{n}}-T\tfrac{\partial \Phi_p}{\partial \mathbf{n}}\right)d\Gamma_1\\&=\int_{\Omega}\left(-\Phi_p\tfrac{g}{K}\right)d\Omega\end{aligned}\tag{4.7}$$

Then, considering the boundary conditions (3.1d), (3.1e), (4.1b), (4.1d) and (4.1e), Eq.(4.7) can be rearranged as:

$$\int_{S_0}\left(\Phi_p\frac{\partial T}{\partial \mathbf{n}}\right)dS_0+\int_{S_1}\left(\Phi_p\frac{\partial T}{\partial \mathbf{n}}-T\frac{\partial \Phi_p}{\partial \mathbf{n}}\right)dS_1=\int_{\Omega}\left(-\Phi_p\frac{g}{K}\right)d\Omega\tag{4.8}$$

Using Eqs.(3.1c) and (4.1c), and replacing the temperature T on the external boundary S_1 by some temperature measurements Y, we obtain:

$$\int_{S_0}\left(\Phi_p\frac{\partial T}{\partial \mathbf{n}}\right)dS_0+\int_{S_1}\left[-f_p\frac{h_{env}(Y-T_{env})}{K}-Y\frac{\partial \Phi_p}{\partial \mathbf{n}}\right]dS_1=\int_{\Omega}\left(-\Phi_p\frac{g}{K}\right)d\Omega\tag{4.9}$$

Therefore, it is possible to define the Reciprocity Functional with respect to Φ_p as:

$$\Re(\Phi_p)=\int_{S_1}\left[-f_p\frac{h_{env}(Y-T_{env})}{K}-Y\frac{\partial \Phi_p}{\partial \mathbf{n}}\right]dS_1\tag{4.10}$$

and the integral of the heat source as:

$$\mathbb{Q}(\Phi_p)=\int_{\Omega}\left(\Phi_p\frac{g}{K}\right)d\Omega\tag{4.11}$$

Hence, substituting Eqs.(4.10) and (4.11) into Eq. (4.9) and defining the potential Φ_p on the boundary S_0 as μ_p we have:

$$-\Re(\Phi_p)-\mathbb{Q}(\Phi_p)=\int_{S_0}\left(\Phi_p\frac{\partial T}{\partial \mathbf{n}}\right)dS_0=\left\langle\mu_p,\frac{\partial T}{\partial \mathbf{n}}\right\rangle_{L^2(S_0)}\tag{4.12}$$

As $f_p(\theta,z)$ is an orthogonal basis, its projection on the boundary S_0, defined as μ_p, is also orthogonal [7, 8]. Consequently, we can write the temperature gradient on the internal boundary S_0 as the following linear combination of the orthogonal functions μ_p as:

$$\frac{\partial T}{\partial \mathbf{n}}|_{S_0} = \sum_{q=0}^{(N_\theta N_z)} \mu_q \alpha_q \tag{4.13}$$

where $(N_\theta + 1)$ and $(N_z + 1)$ are the number of orthonormal basis functions used in the angular and longitudinal direction, respectively. The α_q coefficients need to be determined, as it will be shown later. Replacing Eq.(4.13) into Eq.(4.12) we obtain:

$$-\Re(\Phi_p) - \mathbb{Q}(\Phi_p) = \left\langle \mu_p, \sum_{q=0}^{(N_\theta N_z)} \mu_q \alpha_q \right\rangle_{L^2(S_0)} \tag{4.14}$$

Eq.(4.14) is reformulated as the linear system (4.15), whose solution is the vector α_p. Once α_p is found, the temperature gradient on the inner surface S_0 can be easily calculated using Eq. (4.13).

$$\sum_{q=0}^{(N_\theta N_z)} \langle \mu_p, \mu_q \rangle_{L^2(S_0)} \alpha_q = -\Re(\Phi_p) - \mathbb{Q}(\Phi_p); \qquad p = 0, 1, 2, 3, ... \tag{4.15}$$

4.3 Reciprocity Function Analysis for Estimating the Internal Wall Temperature through Steady Temperature Data on the External Boundary

Analogous to the heat flux estimation, the Reciprocity Function Method can also be used to estimate the temperature on the internal surface S_0. Once again, following the procedure outlined by TOUGRI *et al.* [8] and COLAÇO *et al.* [7], multiplying Eq.(3.1a) by Ψ_p and Eq.(4.2a) by $(-T)$ and summing up the resulting expressions, it is possible to write the following integral over the entire domain Ω:

$$\int_\Omega \left(\Psi_p \nabla^2 T - T \nabla^2 \Psi_p\right) d\Omega = \int_\Omega \left(-\Psi_p \frac{g}{K}\right) d\Omega \tag{4.16}$$

Then, using Green's second identity, Eq.(4.16) becomes:

$$\begin{aligned} &\int_{S_0} \left(\Psi_p \tfrac{\partial T}{\partial \mathbf{n}} - T \tfrac{\partial \Psi_p}{\partial \mathbf{n}}\right) dS_0 + \int_{S_1} \left(\Psi_p \tfrac{\partial T}{\partial \mathbf{n}} - T \tfrac{\partial \Psi_p}{\partial \mathbf{n}}\right) dS_1 + \\ &+ \int_{\Gamma_0} \left(\Psi_p \tfrac{\partial T}{\partial \mathbf{n}} - T \tfrac{\partial \Psi_p}{\partial \mathbf{n}}\right) d\Gamma_0 + \int_{\Gamma_1} \left(\Psi_p \tfrac{\partial T}{\partial \mathbf{n}} - T \tfrac{\partial \Psi_p}{\partial \mathbf{n}}\right) d\Gamma_1 \\ &= \int_\Omega \left(-\Psi_p \tfrac{g}{K}\right) d\Omega \end{aligned} \tag{4.17}$$

It is possible to reduce Eq.(4.17), adopting the boundary conditions given by

Eqs.(3.1d), (3.1e), (4.2b), (4.2d) and (4.2e) as the following:

$$\int_{S_0}\left(-T\frac{\partial\Psi_p}{\partial\mathbf{n}}\right)dS_0+\int_{S_1}\left(\Psi_p\frac{\partial T}{\partial\mathbf{n}}-T\frac{\partial\Psi_p}{\partial\mathbf{n}}\right)dS_1=\int_{\Omega}\left(-\Psi_p\frac{g}{K}\right)d\Omega \tag{4.18}$$

Using Eqs.(3.1c) and (4.2c), and considering some temperature measurements Y on the external boundary S_1, it results:

$$\int_{S_0}\left(-T\frac{\partial\Psi_p}{\partial\mathbf{n}}\right)dS_0+\int_{S_1}\left[-f_p\frac{h_{env}(Y-T_{env})}{K}-Y\frac{\partial\Psi_p}{\partial\mathbf{n}}\right]dS_1=\int_{\Omega}\left(-\Psi_p\frac{g}{K}\right)d\Omega \tag{4.19}$$

Consequently, it is possible to write the Reciprocity Functional with respect to Ψ_p as follows:

$$\Re(\Psi_p)=\int_{S_1}\left[-f_p\frac{h_{env}(Y-T_{env})}{K}-Y\frac{\partial\Psi_p}{\partial\mathbf{n}}\right]dS_1 \tag{4.20}$$

Similarly, to Eq.(4.11), the integral of the internal heat generation with respect to Ψ_p can be written as:

$$\mathbb{Q}(\Psi_p)=\int_{\Omega}\left(\Psi_p\frac{g}{K}\right)d\Omega \tag{4.21}$$

Therefore, defining the projection of the orthonormal basis f_p, defined on the boundary S_1, on the internal surface S_0 as $\xi_p=\frac{\partial\Psi_p}{\partial\mathbf{n}}|_{S_0}$ it follows:

$$\Re(\Psi_p)+\mathbb{Q}(\Psi_p)=\int_{S_0}\left(\frac{\partial\Psi_p}{\partial\mathbf{n}}T\right)dS_0=\langle\xi_p,T\rangle_{L^2(S_0)} \tag{4.22}$$

Similarly, to Eq.(4.13) we can assume that the temperature on the inner boundary S_0 can be written as a linear combination of the basis function ξ_p as

$$T|_{S_0}=\sum_{q=0}^{(M_\theta M_z)}\xi_q\beta_q \tag{4.23}$$

where $(M_\theta+1)$ and (M_z+1) are, respectively, the number of orthonormal basis functions used in angular and longitudinal direction. Replacing Eq.(4.23) into Eq.(4.22) we have:

$$\Re(\Psi_p)+\mathbb{Q}(\Psi_p)=\left\langle\xi_p,\sum_{q=0}^{(M_\theta M_z)}\xi_q\beta_q\right\rangle_{L^2(S_0)} \tag{4.24}$$

Eq.(4.24) can be rearranged in a form of a linear system (4.25), whose solution will allow to obtain the β_q coefficients.

$$\sum_{q=0}^{(M_\theta M_z)} \langle \xi_p, \xi_q \rangle_{L^2(S_0)} \beta_q = \Re(\Psi_p) + \mathbb{Q}(\Psi_p); \qquad p = 0, 1, 2, 3, ... \tag{4.25}$$

Once β_q is known, the temperature on the inner surface S_0 can be obtained after using Eq. (4.23).

4.4 Reciprocity Function Analysis for Estimating the Internal Heat Flux through Transient Temperature Data on the External Boundary

The internal heat flux can also be estimated using transient temperature data. For this purpose, the Reciprocity Functional method, formulated according to TOUGRI *et al.* [10, 11], is adopted in this work to estimate the internal heat flux. Following the procedure presented in [10, 11], which is similar to the previous sections at the beginning, we can multiply Eq.(3.2a) by Φ_p and Eq.(4.1a) by $(-T)$, add them together and integrate the result over the entire domain Ω , in order to obtain:

$$\int_\Omega \left(\Phi_p \frac{1}{\alpha} \frac{\partial T}{\partial t} \right) d\Omega = \int_\Omega \left(\Phi_p \nabla^2 T - T \nabla^2 \Phi_p \right) d\Omega + \int_\Omega \left(\Phi_p \frac{g}{K} \right) d\Omega \tag{4.26}$$

Using Green's second identity, Eq.(4.26) becomes:

$$\begin{aligned} &\int_\Omega \left(\Phi_p \tfrac{1}{\alpha} \tfrac{\partial T}{\partial t} \right) d\Omega = \int_{S_0} \left(\Phi_p \tfrac{\partial T}{\partial \mathbf{n}} - T \tfrac{\partial \Phi_p}{\partial \mathbf{n}} \right) dS_0 + \int_{S_1} \left(\Phi_p \tfrac{\partial T}{\partial \mathbf{n}} - T \tfrac{\partial \Phi_p}{\partial \mathbf{n}} \right) dS_1 + \\ &+ \int_{\Gamma_0} \left(\Phi_p \tfrac{\partial T}{\partial \mathbf{n}} - T \tfrac{\partial \Phi_p}{\partial \mathbf{n}} \right) d\Gamma_0 + \int_{\Gamma_1} \left(\Phi_p \tfrac{\partial T}{\partial \mathbf{n}} - T \tfrac{\partial \Phi_p}{\partial \mathbf{n}} \right) d\Gamma_1 + \int_\Omega \left(\Phi_p \tfrac{g}{K} \right) d\Omega \end{aligned} \tag{4.27}$$

Then, considering the boundary conditions (3.2d), (3.2e), (4.1b), (4.1d) and (4.1e), Eq.(4.27) can be reduced to:

$$\int_\Omega \left(\Phi_p \frac{1}{\alpha} \frac{\partial T}{\partial t} \right) d\Omega = \int_{S_0} \left(\Phi_p \frac{\partial T}{\partial \mathbf{n}} \right) dS_0 + \int_{S_1} \left(\Phi_p \frac{\partial T}{\partial \mathbf{n}} - T \frac{\partial \Phi_p}{\partial \mathbf{n}} \right) dS_1 + \int_\Omega \left(\Phi_p \frac{g}{K} \right) d\Omega \tag{4.28}$$

Using Eqs.(3.2c) and (4.2c), and replacing the temperature T on the external boundary S_1 by some temperature measurements $Y(t)$, we have:

$$\begin{aligned}&\int_\Omega \left(\Phi_p \tfrac{1}{\alpha}\tfrac{\partial T}{\partial t}\right) d\Omega = \int_{S_0} \left(\Phi_p \tfrac{\partial T}{\partial \mathbf{n}}\right) dS_0 + \\ &+ \int_{S_1} \left[-f_p \tfrac{h_{env}(Y(t)-T_{env})}{K} - Y(t)\tfrac{\partial \Phi_p}{\partial \mathbf{n}}\right] dS_1 + \int_\Omega \left(\Phi_p \tfrac{g(t)}{K}\right) d\Omega\end{aligned} \tag{4.29}$$

Therefore, similar to the previous analysis, it is possible to define the time-depending Reciprocity Functional with respect to Φ_p, solution of the first auxiliary problem, as:

$$\Re(\Phi_p, t) = \int_{S_1} \left[-f_p \frac{h_{env}(Y(t) - T_{env})}{K} - Y(t)\frac{\partial \Phi_p}{\partial \mathbf{n}}\right] dS_1 \tag{4.30}$$

and the integral of the, possibly time-depending, heat source as:

$$\mathbb{Q}(\Phi_p, t) = \int_\Omega \left(\Phi_p \frac{g(t)}{K}\right) d\Omega \tag{4.31}$$

Consequently, substituting Eqs.(4.30) and (4.31) into Eq.(4.29) we have:

$$\int_\Omega \left(\Phi_p \frac{1}{\alpha}\frac{\partial T}{\partial t}\right) d\Omega = \int_{S_0} \left(\Phi_p \frac{\partial T}{\partial \mathbf{n}}\right) dS_0 + \Re(\Phi_p, t) + \mathbb{Q}(\Phi_p, t) \tag{4.32}$$

The first transient term in Eq.(4.32) can be replaced by the Laplacian at the previous time steps, similarly to the explicit finite-difference scheme, using Eq.(3.2a) as the following:

$$\frac{1}{\alpha}\frac{\partial T^{m+1}}{\partial t} = \nabla^2 T^m + \frac{g^m}{K} \tag{4.33}$$

where m is the time step. Therefore, replacing Eq.(4.33) into Eq.(4.32), it can be rewritten as the following:

$$\int_\Omega \left(\Phi_p \nabla^2 T^m\right) d\Omega + \int_\Omega \left(\Phi_p \frac{g^m}{K}\right) d\Omega = \int_{S_0} \left(\Phi_p \frac{\partial T^{m+1}}{\partial \mathbf{n}}\right) dS_0 + \Re^{m+1}(\Phi_p, t) + \mathbb{Q}^{m+1}(\Phi_p, t) \tag{4.34}$$

where the remaining terms were calculated at time step $m + 1$.

Applying Green's theorem to the first term of Eq. (4.34) we can derive the following expression:

$$\int_\Omega \left(\Phi_p \nabla^2 T^m\right) d\Omega = \int_S \left(\Phi_p \frac{\partial T^m}{\partial \mathbf{n}} - T^m \frac{\partial \Phi_p}{\partial \mathbf{n}}\right) dS + \int_\Omega \left(T^m \nabla^2 \Phi_p\right) d\Omega \tag{4.35}$$

where $S = (S_0 \bigcup S_1 \bigcup \Gamma_0 \bigcup \Gamma_1)$. Then, considering the boundary conditions (3.2d), (3.2e), (4.1b), (4.1d) , (4.1e) and (4.1a), Eq.(4.35) can be reduced as:

$$\int_{\Omega} \left(\Phi_p \nabla^2 T^m\right) d\Omega = \int_{S_0} \left(\Phi_p \frac{\partial T^m}{\partial \mathbf{n}} - T^m \frac{\partial \Phi_p}{\partial \mathbf{n}}\right) dS_0 + \int_{S_1} \left(\Phi_p \frac{\partial T^m}{\partial \mathbf{n}} - T^m \frac{\partial \Phi_p}{\partial \mathbf{n}}\right) dS_1 \tag{4.36}$$

Using Eqs.(3.2c), (4.1b) and (4.1c), and replacing the temperature T^m on the external boundary S_1 by some temperature measurements Y^m we have:

$$\int_{\Omega} \left(\Phi_p \nabla^2 T^m\right) d\Omega = \int_{S_0} \left(\Phi_p \frac{\partial T^m}{\partial \mathbf{n}}\right) dS_0 + \int_{S_1} \left[-f_p \frac{h_{env}(Y^m - T_{env})}{K} - Y^m \frac{\partial \Phi_p}{\partial \mathbf{n}}\right] dS_1 \tag{4.37}$$

Therefore, it is possible to define the time-depending Reciprocity Functional with respect to Φ_p at the time step m as:

$$\Re^m(\Phi_p, t) = \int_{S_1} \left[-f_p \frac{h_{env}(Y(t)^m - T_{env})}{K} - Y(t)^m \frac{\partial \Phi_p}{\partial \mathbf{n}}\right] dS_1 \tag{4.38}$$

In order to simplify the notation, the time-depending Reciprocity Functionals will be written without the explicit time dependence from now on.

Then we have:

$$\int_{\Omega} \left(\Phi_p \nabla^2 T^m\right) d\Omega = \int_{S_0} \left(\Phi_p \frac{\partial T^m}{\partial \mathbf{n}}\right) dS_0 + \Re^m(\Phi_p) \tag{4.39}$$

Replacing Eq.(4.39) into Eq.(4.34) it results:

$$\int_{S_0} \left(\Phi_p \frac{\partial T^m}{\partial \mathbf{n}}\right) dS_0 + \Re^m(\Phi_p) + \mathbb{Q}^m(\Phi_p) = \int_{S_0} \left(\Phi_p \frac{\partial T^{m+1}}{\partial \mathbf{n}}\right) dS_0 + \Re^{m+1}(\Phi_p) + \mathbb{Q}^{m+1}(\Phi_p) \tag{4.40}$$

Eq.(4.40) can be rewrite as:

$$\Re^{m+1}(\Phi_p) - \Re^m(\Phi_p) + \mathbb{Q}^{m+1}(\Phi_p) - \mathbb{Q}^m(\Phi_p) = \int_{S_0} \left[\Phi_p \left(\frac{\partial T^{m+1}}{\partial \mathbf{n}} - \frac{\partial T^m}{\partial \mathbf{n}}\right)\right] dS_0 \tag{4.41}$$

and defining the potential Φ_p on the boundary S_0 as μ_p we have:

$$\Re^{m+1}(\Phi_p) - \Re^m(\Phi_p) + \mathbb{Q}^{m+1}(\Phi_p) - \mathbb{Q}^m(\Phi_p) = \left\langle \mu_p, \left(\frac{\partial T^{m+1}}{\partial \mathbf{n}} - \frac{\partial T^m}{\partial \mathbf{n}}\right)\right\rangle_{L^2(S_0)} \tag{4.42}$$

Therefore, $\frac{\partial T}{\partial n}|_{S_0}$, in steady state is computed by taking the sum $(\frac{\partial T^{m+1}}{\partial \mathbf{n}} - \frac{\partial T^m}{\partial \mathbf{n}})|_{S_0}$ as m goes to infinite (or sufficiently large to achieve the steady state) as the following:

$$\frac{\partial T}{\partial \mathbf{n}}|_{S_0} = \sum_{m=0}^{N_t} \left(\frac{\partial T^{m+1}}{\partial \mathbf{n}}|_{S_0} - \frac{\partial T^m}{\partial \mathbf{n}}|_{S_0}\right) \tag{4.43}$$

where N_t is the number of time steps used for the estimation. A finite number of time steps N_t is sufficient for the estimation. Therefore, it is not necessary to reach the steady-state. The solution of the first auxiliary problem for some orthogonal functions f_p allows the computation of the corresponding μ_p, which forms a generic basis function that can be used to represent the temperature gradient variation $(\frac{\partial T^{m+1}}{\partial \mathbf{n}} - \frac{\partial T^{m}}{\partial \mathbf{n}})|_{S_0}$ on the boundary S_0 as the following linear combination of the orthogonal functions μ_p:

$$\left(\frac{\partial T^{m+1}}{\partial \mathbf{n}} - \frac{\partial T^{m}}{\partial \mathbf{n}}\right)|_{S_0} = \sum_{q=0}^{(N_\theta N_z)} \mu_q \alpha_q^m \tag{4.44}$$

Replacing Eqs.(4.44) into Eq.(4.42), we obtain the following linear system, whose solution is α_q^m

$$\Re^{m+1}(\Phi_p) - \Re^{m}(\Phi_p) + \mathbb{Q}^{m+1}(\Phi_p) - \mathbb{Q}^{m}(\Phi_p) = \sum_{q=0}^{(N_\theta N_z)} \langle \mu_p, \mu_q \rangle_{L^2(S_0)} \alpha_q^m \tag{4.45}$$

Once the coefficients α_q^m are calculated, the temperature gradient variation $(\frac{\partial T^{m+1}}{\partial \mathbf{n}} - \frac{\partial T^{m}}{\partial \mathbf{n}})|_{S_0}$ on the boundary S_0, at each time step m, can be obtained using Eq. (4.44), and finally the total temperature gradient can be estimated through Eq. (4.43).

4.5 Reciprocity Function Analysis for Estimating the Internal Wall Temperature through Transient Temperature Data on the External Boundary

Similarly to the estimation of the heat flux, the internal wall temperature can also be computed using transient temperature measurement on the external boundary. Following again the methodology developed by TOUGRI *et al.* [10, 11], we can multiply Eq.(3.2a) by Ψ_p and Eq.(4.2a) by $(-T)$, add them together and integrate the result over the entire domain Ω in order to obtain:

$$\int_\Omega \left(\Psi_p \frac{1}{\alpha}\frac{\partial T}{\partial t}\right) d\Omega = \int_\Omega \left(\Psi_p \nabla^2 T - T\nabla^2 \Psi_p\right) d\Omega + \int_\Omega \left(\Psi_p \frac{g}{K}\right) d\Omega \tag{4.46}$$

Using Green's second identity, Eq.(4.46) becomes:

$$\int_\Omega \left(\Psi_p \tfrac{1}{\alpha}\tfrac{\partial T}{\partial t}\right) d\Omega = \int_{S_0} \left(\Psi_p \tfrac{\partial T}{\partial \mathbf{n}} - T\tfrac{\partial \Psi_p}{\partial \mathbf{n}}\right) dS_0 + \int_{S_1} \left(\Psi_p \tfrac{\partial T}{\partial \mathbf{n}} - T\tfrac{\partial \Psi_p}{\partial \mathbf{n}}\right) dS_1 +$$

$$+ \int_{\Gamma_0} \left(\Psi_p \tfrac{\partial T}{\partial \mathbf{n}} - T\tfrac{\partial \Psi_p}{\partial \mathbf{n}}\right) d\Gamma_0 + \int_{\Gamma_1} \left(\Psi_p \tfrac{\partial T}{\partial \mathbf{n}} - T\tfrac{\partial \Psi_p}{\partial \mathbf{n}}\right) d\Gamma_1 + \int_\Omega \left(\Psi_p \tfrac{g}{K}\right) d\Omega \tag{4.47}$$

Then, considering the boundary conditions (3.2d), (3.2e), (4.2b), (4.2d) and (4.2e), Eq.(4.47) can be rearranged as:

$$\int_\Omega \left(\Psi_p \frac{1}{\alpha}\frac{\partial T}{\partial t}\right) d\Omega = \int_{S_0} \left(-T\frac{\partial \Psi_p}{\partial \mathbf{n}}\right) dS_0 + \int_{S_1} \left(\Psi_p \frac{\partial T}{\partial \mathbf{n}} - T\frac{\partial \Psi_p}{\partial \mathbf{n}}\right) dS_1 + \int_\Omega \left(\Psi_p \frac{g}{K}\right) d\Omega \tag{4.48}$$

Using Eqs. (3.2c) and (4.2c), and replacing the temperature T on the external boundary S_1 by some temperature measurements $Y(t)$ we have:

$$\begin{aligned} &\int_\Omega \left(\Psi_p \tfrac{1}{\alpha}\tfrac{\partial T}{\partial t}\right) d\Omega = \int_{S_0} \left(-T\tfrac{\partial \Psi_p}{\partial \mathbf{n}}\right) dS_0 + \\ &+ \int_{S_1} \left[-f_p \tfrac{h_{env}(Y(t)-T_{env})}{K} - Y(t)\tfrac{\partial \Psi_p}{\partial \mathbf{n}}\right] dS_1 + \int_\Omega \left(\Psi_p \tfrac{g(t)}{K}\right) d\Omega \end{aligned} \tag{4.49}$$

Therefore, it is possible to define the time-depending Reciprocity Functional with respect to Ψ_p as:

$$\Re(\Psi_p, t) = \int_{S_1} \left[-f_p \frac{h_{env}(Y(t) - T_{env})}{K} - Y(t)\frac{\partial \Psi_p}{\partial \mathbf{n}}\right] dS_1 \tag{4.50}$$

and the integral of the, possibly time-depending, heat source as:

$$\mathbb{Q}(\Psi_p, t) = \int_\Omega \left(\Psi_p \frac{g(t)}{K}\right) d\Omega \tag{4.51}$$

Consequently, substituting Eqs.(4.50) and (4.51) into Eq.(4.49) we have:

$$\int_\Omega \left(\Psi_p \frac{1}{\alpha}\frac{\partial T}{\partial t}\right) d\Omega = \int_{S_0} \left(-T\frac{\partial \Psi_p}{\partial \mathbf{n}}\right) dS_0 + \Re(\Psi_p, t) + \mathbb{Q}(\Psi_p, t) \tag{4.52}$$

The transient term in Eq.(4.52) can be replaced by the Laplacian at the previous time step, similarly to the explicit finite difference approximation, using Eq.(3.2a) as the following:

$$\frac{1}{\alpha}\frac{\partial T^{m+1}}{\partial t} = \nabla^2 T^m + \frac{g^m}{K} \tag{4.53}$$

where m is the time step. Therefore, replacing Eq.(4.53) into Eq.(4.52), it can be rewritten as the following, where the explicit dependence of $\Re$ and $\mathbb{Q}$ with time was

dropped for simplicity.

$$\int_{\Omega}\left(\Psi_p\nabla^2 T^m\right)d\Omega+\int_{\Omega}\left(\Psi_p\frac{g^m}{K}\right)d\Omega=\int_{S_0}\left(-T^{m+1}\frac{\partial\Psi_p}{\partial\mathbf{n}}\right)dS_0+\Re^{m+1}(\Psi_p)+\mathbb{Q}^{m+1}(\Psi_p) \tag{4.54}$$

Applying the Green's theorem to the first term of Eq.(4.54) we can derive the following expressions:

$$\int_{\Omega}\left(\Psi_p\nabla^2 T^m\right)d\Omega=\int_{S}\left(\Psi_p\frac{\partial T^m}{\partial\mathbf{n}}-T^m\frac{\partial\Psi_p}{\partial\mathbf{n}}\right)dS+\int_{\Omega}\left(T^m\nabla^2\Psi_p\right)d\Omega \tag{4.55}$$

with $S=(S_0\bigcup S_1\bigcup\Gamma_0\bigcup\Gamma_1)$. Then considering the boundary conditions (3.2d), (3.2e), (4.2b), (4.2d) , (4.2e) and (4.2a), Eq.(4.55) can be rearranged as:

$$\int_{\Omega}\left(\Psi_p\nabla^2 T^m\right)d\Omega=\int_{S_0}\left(\Psi_p\frac{\partial T^m}{\partial\mathbf{n}}-T^m\frac{\partial\Psi_p}{\partial\mathbf{n}}\right)dS_0+\int_{S_1}\left(\Psi_p\frac{\partial T^m}{\partial\mathbf{n}}-T^m\frac{\partial\Psi_p}{\partial\mathbf{n}}\right)dS_1 \tag{4.56}$$

Using Eqs.(3.2c), (4.2b) and (4.2c), and replacing the temperature T^m on the external boundary S_1 by some temperature measurements Y^m we have:

$$\int_{\Omega}\left(\Psi_p\nabla^2 T^m\right)d\Omega=\int_{S_0}\left(-T^m\frac{\partial\Psi_p}{\partial\mathbf{n}}\right)dS_0+\int_{S_1}\left[-f_p\frac{h_{env}(Y^m-T_{env})}{K}-Y^m\frac{\partial\Psi_p}{\partial\mathbf{n}}\right]dS_1 \tag{4.57}$$

Therefore, it is possible to define the time-depending Reciprocity Functional with respect to Ψ_p at the time step m as:

$$\Re^m(\Psi_p)=\int_{S_1}\left[-f_p\frac{h_{env}(Y^m-T_{env})}{K}-Y^m\frac{\partial\Psi_p}{\partial\mathbf{n}}\right]dS_1 \tag{4.58}$$

Then we have:

$$\int_{\Omega}\left(\Psi_p\nabla^2 T^m\right)d\Omega=\int_{S_0}\left(-T^m\frac{\partial\Psi_p}{\partial\mathbf{n}}\right)dS_0+\Re^m(\Psi_p) \tag{4.59}$$

Replacing Eq.(4.59) into Eq.(4.54) we have:

$$\begin{aligned}\textstyle\int_{S_0}\left(-T^m\frac{\partial\Psi_p}{\partial\mathbf{n}}\right)dS_0+\Re^m(\Psi_p)+\mathbb{Q}^m(\Psi_p)=\int_{S_0}\left(-T^{m+1}\frac{\partial\Psi_p}{\partial\mathbf{n}}\right)dS_0+\\ +\Re^{m+1}(\Psi_p)+\mathbb{Q}^{m+1}(\Psi_p)\end{aligned} \tag{4.60}$$

Eq.(4.60) can be rewritten as:

$$\Re^{m+1}(\Psi_p)-\Re^m(\Psi_p)+\mathbb{Q}^{m+1}(\Psi_p)-\mathbb{Q}^m(\Psi_p)=\int_{S_0}\left[\frac{\partial\Psi_p}{\partial\mathbf{n}}\left(T^{m+1}-T^m\right)\right]dS_0 \tag{4.61}$$

Defining the potential $\frac{\partial \Psi_p}{\partial n}$ on the boundary S_0 as ξ_p we have:

$$\Re^{m+1}(\Psi_p) - \Re^m(\Psi_p) + \mathbb{Q}^{m+1}(\Psi_p) - \mathbb{Q}^m(\Psi_p) = \left\langle \xi_p, \left(T^{m+1} - T^m\right)\right\rangle_{L^2(S_0)} \tag{4.62}$$

Therefore, $T_{|S_0}$ in steady-state is computed by taking the sum $(T^{m+1} - T^m)_{|S_0}$ as m goes to infinity (or sufficiently large to achieve the steady-state) as the following:

$$T_{|S_0} = \sum_{m=0}^{N_t} \left(T^{m+1} - T^m\right)_{|S_0} \tag{4.63}$$

where N_t is the number of time steps used for calculation. A finite number of time steps N_t is also sufficient in this case for the estimation. Therefore, it is not necessary to reach steady-state. The solution of the second auxiliary problem for some orthogonal functions f_p allows the computation of the corresponding ξ_p, which forms a generic basis function that can be used to represent the temperature difference at two successive time steps $(T^{m+1} - T^m)$ on the boundary S_0 as the following linear combination of the orthogonal functions ξ_p:

$$\left(T^{m+1} - T^m\right)|_{S_0} = \sum_{q=0}^{(N_\theta N_z)} \xi_q \beta_q^m \tag{4.64}$$

Replacing Eq.(4.64) into Eq.(4.62), we obtain the following linear system, whose solution is β_q^m

$$\Re^{m+1}(\Psi_p) - \Re^m(\Psi_p) + \mathbb{Q}^{m+1}(\Psi_p) - \mathbb{Q}^m(\Psi_p) = \sum_{q=0}^{(N_\theta N_z)} \langle \xi_p, \xi_q \rangle_{L^2(S_0)} \beta_q^m \tag{4.65}$$

Once the coefficients β_q^m are calculated, the temperature variation $(T^{m+1} - T^m)$ on the boundary S_0 at each time step can be obtained using Eq. (4.64), and finally the total temperature in steady state on the internal wall S_0 can be estimated through Eq.(4.63).

4.6 Analytical Solution of the Auxiliary Problems

The auxiliary problems given by Eqs. (4.1) and (4.2) can be solved by the Classical Integral Transform Technique (CITT), following OZISIK [50]. As it will be shown, this approach simplifies the entire procedure by avoiding the solution of the linear systems achieved by the above formulation of the Reciprocity Functional Method.

4.6.1 Solution of the Auxiliary Problem used for the Estimation of the Internal Heat Flux

The first auxiliary problem, given by Eqs.(4.1), can be written in cylindrical coordinates as:

$$\frac{\partial^2\Phi_p}{\partial r^2}+\frac{1}{r}\frac{\partial\Phi_p}{\partial r}+\frac{1}{r^2}\frac{\partial^2\Phi_p}{\partial\theta^2}+\frac{\partial^2\Phi_p}{\partial z^2}=0 \qquad \text{in} \quad \Omega \tag{4.66a}$$

$$\frac{\partial\Phi_p}{\partial r}=0 \qquad \text{on} \quad r=r_0 \tag{4.66b}$$

$$\Phi_p=f_p(\theta,z) \qquad \text{on} \quad r=r_1 \tag{4.66c}$$

$$\frac{\partial\Phi_p}{\partial z}=0 \qquad \text{on} \quad z=0 \tag{4.66d}$$

$$\frac{\partial\Phi_p}{\partial z}=0 \qquad \text{on} \quad z=L \tag{4.66e}$$

$$\Phi_p(r,0,z)=\Phi_p(r,2\pi,z) \tag{4.66f}$$

$$\frac{\partial\Phi_p}{\partial\theta}|_{\theta=0}=\frac{\partial\Phi_p}{\partial\theta}|_{\theta=2\pi} \tag{4.66g}$$

where Eqs.(4.66f) and (4.66g) are respectively the potential and flux continuity equations.

The above equations can be solved using the Classical Integral Transform Technique [50]. The dependence on the z direction can be removed by using the following Integral-Transform pair [50]:

$$\overline{\Phi}_p(r,\theta,\lambda_m)=\int_0^L Z(z,\lambda_m)\Phi_p(r,\theta,z)dz \tag{4.67a}$$

$$\Phi_p(r,\theta,z)=\sum_{m=0}^{\infty}\frac{Z(z,\lambda_m)}{\mathbb{N}(\lambda_m)}\overline{\Phi}_p(r,\theta,\lambda_m) \tag{4.67b}$$

where $Z(z,\lambda_m)$ are the eigenfunctions and λ_m the eigenvalues of an associated eigenvalue problem, and $\mathbb{N}$ is the norm [50].

Similarly, the dependence on the θ direction can be transformed by the following Integral-Transform pair [50]:

$$\overline{\overline{\Phi}}_p(r,\nu,\lambda_m)=\int_0^{2\pi}\cos\nu(\theta-\theta')\overline{\Phi}_p(r,\theta',\lambda_m)d\theta' \tag{4.68a}$$

$$\overline{\Phi}_p(r,\theta,\lambda_m)=\frac{1}{2\pi}\overline{\overline{\Phi}}_p(r,0,\lambda_m)+\sum_{\nu=1}^{\infty}\frac{1}{\pi}\overline{\overline{\Phi}}_p(r,\nu,\lambda_m) \tag{4.68b}$$

When the z and θ dependencies are successively transformed, the following or-

dinary differential equation is obtained:

$$\frac{d^2\overline{\overline{\Phi}}_p}{dr^2} + \frac{1}{r}\frac{d\overline{\overline{\Phi}}_p}{dr} - \left(\frac{\nu^2}{r^2} + \lambda_m\right)\overline{\overline{\Phi}}_p = 0 \quad \text{in} \quad r_0 < r < r_1 \tag{4.69a}$$

$$\frac{d\overline{\overline{\Phi}}_p}{dr} = 0 \quad \text{on} \quad r = r_0 \tag{4.69b}$$

$$\overline{\overline{\Phi}}_p = \overline{\overline{f}}_{m,\nu}(\theta) \quad \text{on} \quad r = r_1 \tag{4.69c}$$

where $\overline{\overline{f}}_{m,\nu}(\theta)$ is the transformed boundary condition on $r = r_1$.

The solution of Eq.(4.69) is a combination of modified Bessel functions of first kind $I_\nu(\lambda_m r)$ and second kind $K_\nu(\lambda_m r)$ of order ν, subjected to the proper boundary conditions. Therefore, the solution is presented in the following form:

$$\overline{\overline{\Phi}}_p(r,\nu,\lambda_m) = \overline{\overline{f}}_{m,\nu}(\theta)\left[A_{\nu,m}I_\nu(\lambda_m r) + B_{\nu,m}K_\nu(\lambda_m r)\right] \tag{4.70}$$

where it can be shown that

$$A_{\nu,m} = \frac{\left[\frac{\partial K_\nu(\lambda_m r)}{\partial r}\right]_{r=0}}{I_\nu(\lambda_m r_1)\left[\frac{\partial K_\nu(\lambda_m r)}{\partial r}\right]_{r=0} - \left[\frac{\partial I_\nu(\lambda_m r)}{\partial r}\right]_{r=0} K_\nu(\lambda_m r_1)} \tag{4.71a}$$

$$B_{\nu,m} = \frac{\left[\frac{\partial I_\nu(\lambda_m r)}{\partial r}\right]_{r=0}}{I_\nu(\lambda_m r_1)\left[\frac{\partial K_\nu(\lambda_m r)}{\partial r}\right]_{r=0} - \left[\frac{\partial I_\nu(\lambda_m r)}{\partial r}\right]_{r=0} K_\nu(\lambda_m r_1)} \tag{4.71b}$$

and

$$\frac{\partial I_\nu(\lambda_m r)}{\partial r} = \lambda_m I_{\nu+1}(\lambda_m r) + \frac{\nu}{r}I_\nu(\lambda_m r) \tag{4.72a}$$

$$\frac{\partial K_\nu(\lambda_m r)}{\partial r} = -\lambda_m K_{\nu+1}(\lambda_m r) + \frac{\nu}{r}K_\nu(\lambda_m r) \tag{4.72b}$$

For $\lambda_0 = 0$ and $\nu \neq 0$, Eq.(4.72) reduces to:

$$\overline{\overline{\Phi}}_p(r,\nu,\lambda_0) = \overline{\overline{f}}_{0,\nu}(\theta)\frac{\cosh\left[\nu(\log r - \log r_0)\right]}{\cosh\left[\nu(\log r_1 - \log r_0)\right]} \tag{4.73}$$

Similarly, for $\lambda_0 = 0$ and $\nu = 0$ it follows:

$$\overline{\overline{\Phi}}_p(r,0,\lambda_0) = \overline{\overline{f}}_{0,0}(\theta) \tag{4.74}$$

Using Eqs.(4.67b) and (4.68b), we can obtain

$$\Phi_p(r,\theta,z) = \sum_{m=0}^{\infty}\frac{Z(z,\lambda_m)}{\mathbb{N}(\lambda_m)}\left[\frac{1}{2\pi}\overline{\overline{\Phi}}_p(r,0,\lambda_m) + \sum_{\nu=1}^{\infty}\frac{1}{\pi}\overline{\overline{\Phi}}_p(r,\nu,\lambda_m)\right] \tag{4.75}$$

and, after some rearrangement,

$$\begin{aligned}\Phi_p(r,\theta,z) = \tfrac{Z(z,\lambda_0)}{\mathbb{N}(\lambda_0)}\left[\tfrac{1}{2\pi}\overline{\overline{\Phi}}_p(r,0,\lambda_0) + \textstyle\sum_{\nu=1}^{\infty}\tfrac{1}{\pi}\overline{\overline{\Phi}}_p(r,\nu,\lambda_0)\right] + \\ + \textstyle\sum_{m=1}^{\infty}\tfrac{Z(z,\lambda_m)}{\mathbb{N}(\lambda_m)}\left[\tfrac{1}{2\pi}\overline{\overline{\Phi}}_p(r,0,\lambda_m) + \textstyle\sum_{\nu=1}^{\infty}\tfrac{1}{\pi}\overline{\overline{\Phi}}_p(r,\nu,\lambda_m)\right]\end{aligned} \tag{4.76}$$

From Eq.(4.76) it follows:

$$\begin{aligned}\Phi_p(r,\theta,z) = \tfrac{Z(z,\lambda_0)}{\mathbb{N}(\lambda_0)}\tfrac{1}{2\pi}\overline{\overline{\Phi}}_p(r,0,\lambda_0) + \tfrac{Z(z,\lambda_0)}{\mathbb{N}(\lambda_0)}\textstyle\sum_{\nu=1}^{\infty}\tfrac{1}{\pi}\overline{\overline{\Phi}}_p(r,\nu,\lambda_0) + \\ + \textstyle\sum_{m=1}^{\infty}\tfrac{Z(z,\lambda_m)}{\mathbb{N}(\lambda_m)}\tfrac{1}{2\pi}\overline{\overline{\Phi}}_p(r,0,\lambda_m) + \textstyle\sum_{m=1}^{\infty}\sum_{\nu=1}^{\infty}\tfrac{1}{\pi}\tfrac{Z(z,\lambda_m)}{\mathbb{N}(\lambda_m)}\overline{\overline{\Phi}}_p(r,\nu,\lambda_m)\end{aligned} \tag{4.77}$$

In the above equations, the transformed function $\overline{\overline{f}}_{m,\nu}(\theta)$ is written as:

$$\begin{aligned}\overline{\overline{f}}_{m,\nu}(\theta) = \cos\nu\theta\textstyle\int_0^{2\pi}\cos\nu\theta' f_k(\theta')d\theta'\int_0^L Z(z,\lambda_m)f_l(z)dz + \\ + \sin\nu\theta\textstyle\int_0^{2\pi}\sin\nu\theta' f_k(\theta')d\theta'\int_0^L Z(z,\lambda_m)f_l(z)dz\end{aligned} \tag{4.78}$$

Substituting $\overline{\overline{f}}_{m,\nu}(\theta)$ and $\overline{\overline{\Phi}}_p(\theta)$ into Eq.(4.77) we finally obtain Eq.(4.79) in which the index p is related to k and l according to the Eq.(4.3).

$$\Phi_{p_{k,l}}(r,\theta,z) = \frac{Z(z,\lambda_0)}{\mathbb{N}(\lambda_0)}\frac{1}{2\pi}\int_0^{2\pi} f_k(\theta')d\theta' \int_0^L Z(z,\lambda_0) f_l(z)dz +$$

$$+\frac{Z(z,\lambda_0)}{\mathbb{N}(\lambda_0)}\sum_{\nu=1}^{\infty}\frac{1}{\pi}\left\{\frac{\cosh\left[\nu(\log r - \log r_0)\right]}{\cosh\left[\nu(\log r_1 - \log r_0)\right]}\right\}$$

$$\left[\cos\nu\theta\int_0^{2\pi}\cos\nu\theta' f_k(\theta')d\theta' \int_0^L Z(z,\lambda_m) f_l(z)dz +\right.$$

$$\left.+\sin\nu\theta\int_0^{2\pi}\sin\nu\theta' f_k(\theta')d\theta' \int_0^L Z(z,\lambda_m) f_l(z)dz\right] +$$

$$+\sum_{m=1}^{\infty}\frac{Z(z,\lambda_m)}{\mathbb{N}(\lambda_m)}\frac{1}{2\pi}\left[A_{0,m}I_0(\lambda_m r) + B_{0,m}K_0(\lambda_m r)\right] \tag{4.79}$$

$$\int_0^{2\pi} f_k(\theta')d\theta' \int_0^L Z(z,\lambda_0) f_l(z)dz +$$

$$+\sum_{m=1}^{\infty}\sum_{\nu=1}^{\infty}\frac{1}{\pi}\frac{Z(z,\lambda_m)}{\mathbb{N}(\lambda_m)}\left[A_{\nu,m}I_\nu(\lambda_m r) + B_{\nu,m}K_\nu(\lambda_m r)\right]$$

$$\left[\cos\nu\theta\int_0^{2\pi}\cos\nu\theta' f_k(\theta')d\theta' \int_0^L Z(z,\lambda_m) f_l(z)dz +\right.$$

$$\left.+\sin\nu\theta\int_0^{2\pi}\sin\nu\theta' f_k(\theta')d\theta' \int_0^L Z(z,\lambda_m) f_l(z)dz\right]$$

The orthogonal functions f_k and f_l can be chosen to be orthogonal to $\cos(\nu\theta)$ and $Z(z,\lambda_m)$, respectively, in order to eliminate the different summations in Eq. (4.79), as shown by TOUGRI *et al.* [8]. In this work we will extend the orthogonal functions f_k to be also orthogonal to $\sin(\nu\theta)$. Therefore, the orthonormal functions f_k and f_l are chosen as follows [56]:

$$f_k(\theta) = \sqrt{\frac{1}{2\pi r_1}} \qquad \text{for} \quad k = 0 \tag{4.80a}$$

$$f_k(\theta) = \sqrt{\frac{2}{\pi r_1}}\cos\left(\frac{k}{2}\theta\right) \qquad \text{for} \quad k = 2,4,6,... \tag{4.80b}$$

$$f_k(\theta) = \sqrt{\frac{2}{\pi r_1}}\sin\left(\frac{k-1}{2}\theta\right) \qquad \text{for} \quad k = 3,5,7,... \tag{4.80c}$$

and

$$f_l(z) = \sqrt{\frac{1}{L}} \qquad \text{for} \quad l = 0 \tag{4.81a}$$

$$f_l(z) = \sqrt{\frac{2}{L}} \cos\left(l\frac{\pi}{L}z\right) \qquad \text{for} \quad l = 1, 2, 3, ... \tag{4.81b}$$

The Eq.(4.80) is the set of the following orthonormal basis:

$$\left\{\sqrt{\frac{1}{2\pi r_1}}, \sqrt{\frac{2}{\pi r_1}}\cos(\theta), \sqrt{\frac{2}{\pi r_1}}\sin(\theta), \sqrt{\frac{2}{\pi r_1}}\cos(2\theta), \sqrt{\frac{2}{\pi r_1}}\sin(2\theta), ...\right\}$$

That means

$$f_k(\theta) = \begin{cases} \sqrt{\frac{1}{2\pi r_1}} & \text{for} \quad k = 0 \\ \sqrt{\frac{2}{\pi r_1}}\cos(\theta) & \text{for} \quad k = 1 \\ \sqrt{\frac{2}{\pi r_1}}\sin(\theta) & \text{for} \quad k = 2 \\ \sqrt{\frac{2}{\pi r_1}}\cos(2\theta) & \text{for} \quad k = 3 \\ \sqrt{\frac{2}{\pi r_1}}\sin(2\theta) & \text{for} \quad k = 4 \\ \sqrt{\frac{2}{\pi r_1}}\cos(3\theta) & \text{for} \quad k = 5 \\ .... & ... \quad ... \\ .... & ... \quad ... \\ .... & ... \quad ... \end{cases} \tag{4.82}$$

Therefore, it results:

$$\Phi_{p_{k,l}}(r,\theta,z) = \begin{cases} \sqrt{\frac{1}{2\pi L r_1}} & \text{for} \quad k=l=0 \\ \\ \sqrt{\frac{2}{\pi L r_1}} \left\{ \frac{\cosh\left[k(\log r - \log r_0)\right]}{\cosh\left[k(\log r_1 - \log r_0)\right]} \right\} \cos(k\theta) \quad \text{or} \\ \sqrt{\frac{2}{\pi L r_1}} \left\{ \frac{\cosh\left[k(\log r - \log r_0)\right]}{\cosh\left[k(\log r_1 - \log r_0)\right]} \right\} \sin(k\theta) & \text{for} \quad k \geq 1, l=0 \\ \\ \sqrt{\frac{2}{\pi L r_1}} \left[A_{0,l} I_0(\lambda_l r) + B_{0,l} K_0(\lambda_l r)\right] \cos\left(l\frac{\pi}{L} z\right) & \text{for} \quad k=0, l \geq 1 \\ \\ \sqrt{\frac{2}{\pi L r_1}} \left[A_{k,l} I_k(\lambda_m r) + B_{k,l} K_k(\lambda_l r)\right] \cos(k\theta) \cos\left(l\frac{\pi}{L} z\right) \quad \text{or} \\ \sqrt{\frac{2}{\pi L r_1}} \left[A_{k,l} I_k(\lambda_l r) + B_{k,l} K_k(\lambda_l r)\right] \sin(k\theta) \cos\left(l\frac{\pi}{L} z\right) & \text{for} \quad k \geq 1, l \geq 1 \end{cases} \tag{4.83}$$

Consequently, it is possible to write:

$$\mu_p = \begin{cases} \sqrt{\frac{1}{2\pi L r_1}} & \text{for} \quad k=l=0 \\ \\ \sqrt{\frac{2}{\pi L r_1}} \left\{ \frac{1}{\cosh\left[k(\log r_1 - \log r_0)\right]} \right\} \cos(k\theta) \quad \text{or} \\ \sqrt{\frac{2}{\pi L r_1}} \left\{ \frac{1}{\cosh\left[k(\log r_1 - \log r_0)\right]} \right\} \sin(k\theta) & \text{for} \quad k \geq 1, l=0 \\ \\ \sqrt{\frac{2}{\pi L r_1}} \left[A_{0,l} I_0(\lambda_l r_0) + B_{0,l} K_0(\lambda_l r_0)\right] \cos\left(l\frac{\pi}{L} z\right) & \text{for} \quad k=0, l \geq 1 \\ \\ \sqrt{\frac{2}{\pi L r_1}} \left[A_{k,l} I_k(\lambda_l r_0) + B_{k,l} K_k(\lambda_l r_0)\right] \cos(k\theta) \cos\left(l\frac{\pi}{L} z\right) \quad \text{or} \\ \sqrt{\frac{2}{\pi L r_1}} \left[A_{k,l} I_k(\lambda_l r_0) + B_{k,l} K_k(\lambda_l r_0)\right] \sin(k\theta) \cos\left(l\frac{\pi}{L} z\right) & \text{for} \quad k \geq 1, l \geq 1 \end{cases} \tag{4.84}$$

This result will be used in Eq.(4.15), as well as in its derivative. Taking the

derivative of Eq.(4.83) with respect to r we obtain:

$$\frac{\partial \Phi_{p_{k,l}}(r,\theta,z)}{\partial r} = \begin{cases} 0 \qquad\qquad \text{for} \quad k=l=0 \\ \\ \sqrt{\frac{2}{\pi L r_1}} \left\{ \dfrac{k \sinh\left[k(\log r - \log r_0)\right]}{r \cosh\left[k(\log r_1 - \log r_0)\right]} \right\} \cos(k\theta) \quad \text{or} \\ \sqrt{\frac{2}{\pi L r_1}} \left\{ \dfrac{k \sinh\left[k(\log r - \log r_0)\right]}{r \cosh\left[k(\log r_1 - \log r_0)\right]} \right\} \sin(k\theta) \text{ for} \quad k \geq 1, l=0 \\ \\ \sqrt{\frac{2}{\pi L r_1}} \left[A_{0,l} \lambda_l I_1(\lambda_l r) - B_{0,l} \lambda_l K_{k+1}(\lambda_l r) \right] \cos\left(l \frac{\pi}{L} z\right) \\ \qquad\qquad\qquad\qquad\qquad\qquad \text{for} \quad k=0, l \geq 1 \\ \\ \sqrt{\frac{2}{\pi L r_1}} \left\{ A_{k,l} \left[\lambda_l I_{k+1}(\lambda_l r) + \frac{k}{r} I_k(\lambda_l r) \right] + B_{k,l} \left[-\lambda_l K_{k+1}(\lambda_l r) + \right.\right. \\ \qquad\qquad \left.\left. + \frac{k}{r} K_k(\lambda_l r) \right] \right\} \cos(k\theta) \cos\left(l \frac{\pi}{L} z\right) \quad \text{or} \\ \sqrt{\frac{2}{\pi L r_1}} \left\{ A_{k,l} \left[\lambda_l I_{k+1}(\lambda_l r) + \frac{k}{r} I_k(\lambda_l r) \right] + B_{k,l} \left[-\lambda_l K_{k+1}(\lambda_l r) + \right.\right. \\ \qquad\qquad \left.\left. + \frac{k}{r} K_k(\lambda_l r) \right] \right\} \sin(k\theta) \cos\left(l \frac{\pi}{L} z\right) \qquad \text{for} \quad k \geq 1, l \geq 1 \end{cases} \tag{4.85}$$

It can easily be shown that:

$$\left\langle \Phi_{p_{k,l}}, \Phi_{q_{n,m}} \right\rangle_{L^2(S_0)} = \left\langle \Phi_{p_{k,l}}, \Phi_{p_{k,l}} \right\rangle_{L^2(S_0)} = \left\langle \mu_p, \mu_p \right\rangle_{L^2(S_0)} \tag{4.86}$$

Then we have:

$$\left\langle \mu_p, \mu_p \right\rangle_{L^2(S_0)} = \begin{cases} \frac{r_0}{r_1} & \text{for} \quad k=l=0 \\ \\ \frac{r_0}{r_1} \left\{ \dfrac{1}{\cosh\left[k(\log r_1 - \log r_0)\right]} \right\}^2 & \text{for} \quad k \geq 1, l=0 \\ \\ \frac{r_0}{r_1} \left[A_{0,l} I_0(\lambda_l r) + B_{0,l} K_0(\lambda_l r) \right]^2 & \text{for} \quad k=0, l \geq 1 \\ \\ \frac{r_0}{r_1} \left[A_{k,l} I_k(\lambda_l r) + B_{k,l} K_k(\lambda_l r) \right]^2 & \text{for} \quad k \geq 1, l \geq 1 \end{cases} \tag{4.87}$$

The above equation shows that the matrices of the linear systems given by Eqs.(4.15) and (4.25) are diagonal. Therefore, the unknowns α_p^m can be computed

explicitly, which is the main advantage of this new procedure. Then we have:

$$\alpha_p = \begin{cases} \frac{r_1}{r_0}\int_0^L\int_0^{2\pi}\left[f_0(\theta)f_0(z)\dfrac{h_{env}(Y-T_{env})}{K}+Y\dfrac{\partial\Phi_{p_{0,0}}(r_0,\theta,z)}{\partial r}\right]r_0 d\theta dz + \\ -\frac{r_1}{r_0}\int_{r_0}^{r_1}\int_0^L\int_0^{2\pi}\left[\Phi_{p_{0,0}}(r,\theta,z)\dfrac{g}{K}\right]r dr d\theta dz \qquad \text{for} \quad k=l=0 \\ \\ \dfrac{r_1\left\{\int_0^L\int_0^{2\pi}\left[f_k(\theta)f_0(z)\dfrac{h_{env}(Y-T_{env})}{K}+Y\dfrac{\partial\Phi_{p_{k,0}}(r_0,\theta,z)}{\partial r}\right]r_0 d\theta dz\right\}}{r_0\left\{\dfrac{1}{\cosh\left[k(\log r_1-\log r_0)\right]}\right\}^2} \\ \qquad\qquad \text{for} \quad k\geq 1, l=0 \\ \\ \dfrac{r_1\left\{\int_0^L\int_0^{2\pi}\left[f_0(\theta)f_l(z)\dfrac{h_{env}(Y-T_{env})}{K}+Y\dfrac{\partial\Phi_{p_{0,l}}(r_0,\theta,z)}{\partial r}\right]r_0 d\theta dz\right\}}{r_0\left[A_{0,l}I_0(\lambda_l r_0)+B_{0,l}K_0(\lambda_l r_0)\right]^2} \\ \qquad\qquad \text{for} \quad k=0, l\geq 1 \\ \\ \dfrac{r_1\left\{\int_0^L\int_0^{2\pi}\left[f_k(\theta)f_l(z)\dfrac{h_{env}(Y-T_{env})}{K}+Y\dfrac{\partial\Phi_{p_{k,l}}(r_0,\theta,z)}{\partial r}\right]r_0 d\theta dz\right\}}{r_0\left[A_{k,l}I_k(\lambda_l r_0)+B_{k,l}K_k(\lambda_l r_0)\right]^2} \\ \qquad\qquad \text{for} \quad k\geq 1, l\geq 1 \end{cases} \tag{4.88}$$

Finally, with the value of α_p, α_p^m and μ_p, the temperature gradient on the internal boundary surface can be computed using Eq.(4.13) or (4.43), as a simple algebraic equation. Notice that this same result can be used for the transient estimation, since the auxiliary problem used in both cases is the same.

4.6.2 Solution of the Auxiliary Problem Used for the Estimation of the Internal Temperature

The second auxiliary problem, given by Eqs.(4.2), can also been written in cylindrical coordinates, according to Eqs.(4.89):

$$\frac{\partial^2\Psi_p}{\partial r^2}+\frac{1}{r}\frac{\partial\Psi_p}{\partial r}+\frac{1}{r^2}\frac{\partial^2\Psi_p}{\partial\theta^2}+\frac{\partial^2\Psi_p}{\partial z^2}=0 \qquad \text{in} \qquad \Omega \tag{4.89a}$$

$$\Psi_p=0 \qquad \text{on} \qquad r=r_0 \tag{4.89b}$$

$$\Psi_p=f_p(\theta,z) \qquad \text{on} \qquad r=r_1 \tag{4.89c}$$

$$\frac{\partial\Psi_p}{\partial z}=0 \qquad \text{on} \qquad z=0 \tag{4.89d}$$

$$\frac{\partial\Psi_p}{\partial z}=0 \qquad \text{on} \qquad z=L \tag{4.89e}$$

$$\Psi_p(r,0,z)=\Psi_p(r,2\pi,z) \tag{4.89f}$$

$$\frac{\partial\Psi_p}{\partial\theta}|_{\theta=0}=\frac{\partial\Psi_p}{\partial\theta}|_{\theta=2\pi} \tag{4.89g}$$

where Eqs.(4.89f) and (4.89g) are the potential and the flux continuity equations.

The Classical Integral Transform Technique [50] can also be used to solve it. Therefore, the dependence on the z direction is removed by using the following Integral-Transform pair [50]:

$$\overline{\Psi}_p(r,\theta,\lambda_m)=\int_0^L Z(z,\lambda_m)\Psi_p(r,\theta,z)dz \tag{4.90a}$$

$$\Psi_p(r,\theta,z)=\sum_{m=0}^{\infty}\frac{Z(z,\lambda_m)}{\mathbb{N}(\lambda_m)}\overline{\Psi}_p(r,\theta,\lambda_m) \tag{4.90b}$$

where $Z(z,\lambda_m)$ are the eigenfunctions and λ_m the eigenvalues of an associated eigenvalue problem, and $\mathbb{N}$ is the norm [50]. Similarly, the dependence on the θ direction can be transformed by the following Integral-Transform pair [50]:

$$\overline{\overline{\Psi}}_p(r,\theta,\lambda_m)=\int_0^{2\pi}\cos\nu(\theta-\theta')\overline{\Psi}_p(r,\theta',\lambda_m)d\theta' \tag{4.91a}$$

$$\overline{\Psi}_p(r,\nu,\lambda_m)=\frac{1}{2\pi}\overline{\overline{\Psi}}_p(r,0,\lambda_m)+\sum_{\nu=1}^{\infty}\frac{1}{\pi}\overline{\overline{\Psi}}_p(r,\nu,\lambda_m) \tag{4.91b}$$

When the z and θ dependencies are successively transformed, the following ordinary differential equation is obtained:

$$\frac{d^2\overline{\overline{\Psi}}_p}{dr^2}+\frac{1}{r}\frac{d\overline{\overline{\Psi}}_p}{dr}-\left(\frac{\nu^2}{r^2}+\lambda_m\right)\overline{\overline{\Psi}}_p=0 \qquad \text{in} \qquad r_0<r<r_1 \tag{4.92a}$$

$$\overline{\overline{\Psi}}_p=0 \qquad \text{on} \qquad r=r_0 \tag{4.92b}$$

$$\overline{\overline{\Psi}}_p=\overline{\overline{f}}_{m,\nu}(\theta) \qquad \text{on} \qquad r=r_1 \tag{4.92c}$$

where $\overline{\overline{f}}_{m,\nu}(\theta)$ is the transformed boundary condition on $r=r_1$.

The solution of Eq.(4.92) is a combination of modified Bessel functions of first

kind $I_\nu(\lambda_m r)$ and second kind $K_\nu(\lambda_m r)$ of order ν, subjected to the proper boundary conditions. Therefore, the solution is presented in the following form:

$$\overline{\overline{\Psi}}_p(r,\nu,\lambda_m) = \overline{\overline{f}}_{m,\nu}(\theta)\left[C_{\nu,m} I_\nu(\lambda_m r) + D_{\nu,m} K_\nu(\lambda_m r)\right] \tag{4.93}$$

where the coefficients $C_{\nu,m}$ and $D_{\nu,m}$ are determined using the Eqs.(4.92a) and (4.92b) as follows

$$C_{\nu,m} = \frac{\left[K_\nu(\lambda_m r)\right]_{r=0}}{I_\nu(\lambda_m r_1)\left[K_\nu(\lambda_m r)\right]_{r=0} - \left[I_\nu(\lambda_m r)\right]_{r=0} K_\nu(\lambda_m r_1)} \tag{4.94a}$$

$$D_{\nu,m} = -\frac{\left[I_\nu(\lambda_m r)\right]_{r=0}}{I_\nu(\lambda_m r_1)\left[K_\nu(\lambda_m r)\right]_{r=0} - \left[I_\nu(\lambda_m r)\right]_{r=0} K_\nu(\lambda_m r_1)} \tag{4.94b}$$

For $\lambda_0 = 0$ and for $\nu \neq 0$ Eq.(4.93) reduces to:

$$\overline{\overline{\Psi}}_p(r,\nu,\lambda_0) = \overline{\overline{f}}_{0,\nu}(\theta)\frac{\sinh\left[\nu(\log r - \log r_0)\right]}{\sinh\left[\nu(\log r_1 - \log r_0)\right]} \tag{4.95}$$

Similarly, for $\lambda_0 = 0$ and $\nu = 0$ it follows:

$$\overline{\overline{\Psi}}_p(r,0,\lambda_0) = \overline{\overline{f}}_{0,0}(\theta)\frac{\log\left(\frac{r}{r_0}\right)}{\log\left(\frac{r_1}{r_0}\right)} \tag{4.96}$$

Using Eqs.(4.90b) and (4.91b), we can obtain

$$\Psi_p(r,\theta,z) = \sum_{m=0}^{\infty} \frac{Z(z,\lambda_m)}{\mathbb{N}(\lambda_m)}\left[\frac{1}{2\pi}\overline{\overline{\Psi}}_p(r,0,\lambda_m) + \sum_{\nu=1}^{\infty}\frac{1}{\pi}\overline{\overline{\Psi}}_p(r,\nu,\lambda_m)\right] \tag{4.97}$$

and, after some rearrangement,

$$\begin{aligned}\Psi_p(r,\theta,z) = {} & \frac{Z(z,\lambda_0)}{\mathbb{N}(\lambda_0)}\left[\tfrac{1}{2\pi}\overline{\overline{\Psi}}_p(r,0,\lambda_0) + \sum_{\nu=1}^{\infty}\frac{1}{\pi}\overline{\overline{\Psi}}_p(r,\nu,\lambda_0)\right] + \\ & + \sum_{m=1}^{\infty}\frac{Z(z,\lambda_m)}{\mathbb{N}(\lambda_m)}\left[\frac{1}{2\pi}\overline{\overline{\Psi}}_p(r,0,\lambda_m) + \sum_{\nu=1}^{\infty}\frac{1}{\pi}\overline{\overline{\Psi}}_p(r,\nu,\lambda_m)\right]\end{aligned} \tag{4.98}$$

From Eq.(4.98) it follows:

$$\Psi_p(r,\theta,z) = \frac{Z(z,\lambda_0)}{\mathbb{N}(\lambda_0)}\frac{1}{2\pi}\overline{\overline{\Psi}}_p(r,0,\lambda_0) + \frac{Z(z,\lambda_0)}{\mathbb{N}(\lambda_0)}\sum_{\nu=1}^{\infty}\frac{1}{\pi}\overline{\overline{\Psi}}_p(r,\nu,\lambda_0) + \\ + \sum_{m=1}^{\infty}\frac{Z(z,\lambda_m)}{\mathbb{N}(\lambda_m)}\frac{1}{2\pi}\overline{\overline{\Psi}}_p(r,0,\lambda_m) + \sum_{m=1}^{\infty}\sum_{\nu=1}^{\infty}\frac{1}{\pi}\frac{Z(z,\lambda_m)}{\mathbb{N}(\lambda_m)}\overline{\overline{\Psi}}_p(r,\nu,\lambda_m) \tag{4.99}$$

In the above equations, the transformed function $\overline{\overline{f}}_{m,\nu}(\theta)$ is written as:

$$\overline{\overline{f}}_{m,\nu}(\theta) = \cos\nu\theta\int_0^{2\pi}\cos\nu\theta' f_k(\theta')d\theta'\int_0^{L} Z(z,\lambda_m)f_l(z)dz + \\ + \sin\nu\theta\int_0^{2\pi}\sin\nu\theta' f_k(\theta')d\theta'\int_0^{L} Z(z,\lambda_m)f_l(z)dz \tag{4.100}$$

Substituting $\overline{\overline{f}}_{m,\nu}(\theta)$ and $\overline{\overline{\Psi}}_p(\theta)$ into Eq.(4.99) we finally obtain Eq.(4.101) in

which the index p is related to k and l according to the Eq.(4.3).

$$\Psi_{p_{k,l}}(r,\theta,z) = \frac{Z(z,\lambda_0)}{\mathbb{N}(\lambda_0)}\frac{1}{2\pi}\frac{\log\left(\frac{r}{r_0}\right)}{\log\left(\frac{r_1}{r_0}\right)}\int_0^{2\pi} f_k(\theta')d\theta' \int_0^L Z(z,\lambda_0)f_l(z)dz+$$

$$+\frac{Z(z,\lambda_0)}{\mathbb{N}(\lambda_0)}\sum_{\nu=1}^{\infty}\frac{1}{\pi}\left\{\frac{\sinh\left[\nu(\log r-\log r_0)\right]}{\sinh\left[\nu(\log r_1-\log r_0)\right]}\right\}$$

$$\left[\cos\nu\theta\int_0^{2\pi}\cos\nu\theta' f_k(\theta')d\theta' \int_0^L Z(z,\lambda_m)f_l(z)dz+\right.$$

$$\left.+\sin\nu\theta\int_0^{2\pi}\sin\nu\theta' f_k(\theta')d\theta' \int_0^L Z(z,\lambda_m)f_l(z)dz\right]+$$

$$+\sum_{m=1}^{\infty}\frac{Z(z,\lambda_m)}{\mathbb{N}(\lambda_m)}\frac{1}{2\pi}\left[C_{0,m}I_0(\lambda_m r)+D_{0,m}K_0(\lambda_m r)\right]$$

$$\int_0^{2\pi} f_k(\theta')d\theta' \int_0^L Z(z,\lambda_0)f_l(z)dz+$$

$$+\sum_{m=1}^{\infty}\sum_{\nu=1}^{\infty}\frac{1}{\pi}\frac{Z(z,\lambda_m)}{\mathbb{N}(\lambda_m)}\left[C_{\nu,m}I_\nu(\lambda_m r)+D_{\nu,m}K_\nu(\lambda_m r)\right]$$

$$\left[\cos\nu\theta\int_0^{2\pi}\cos\nu\theta' f_k(\theta')d\theta' \int_0^L Z(z,\lambda_m)f_l(z)dz+\right.$$

$$\left.+\sin\nu\theta\int_0^{2\pi}\sin\nu\theta' f_k(\theta')d\theta' \int_0^L Z(z,\lambda_m)f_l(z)dz\right] \tag{4.101}$$

Using the orthonormal basis functions given by Eqs.(4.80) and (4.81) and taking

the advantage of the orthogonality properties, Eq.(4.101) turns into:

$$\Psi_{p_{k,l}}(r,\theta,z)=\begin{cases}\sqrt{\frac{1}{2\pi Lr_1}}\dfrac{\log\left(\frac{r}{r_0}\right)}{\log\left(\frac{r_1}{r_0}\right)} & \text{for} \quad k=l=0\\[2ex] \sqrt{\frac{2}{\pi Lr_1}}\left\{\dfrac{\sinh\left[k(\log r-\log r_0)\right]}{\sinh\left[k(\log r_1-\log r_0)\right]}\right\}\cos\left(k\theta\right) \quad \text{or}\\ \sqrt{\frac{2}{\pi Lr_1}}\left\{\dfrac{\sinh\left[k(\log r-\log r_0)\right]}{\sinh\left[k(\log r_1-\log r_0)\right]}\right\}\sin\left(k\theta\right) & \text{for} \quad k\geq 1, l=0\\[2ex] \sqrt{\frac{2}{\pi Lr_1}}\left[C_{0,l}I_0(\lambda_l r)+D_{0,l}K_0(\lambda_l r)\right]\cos\left(l\frac{\pi}{L}z\right) & \text{for} \quad k=0, l\geq 1\\[2ex] \sqrt{\frac{2}{\pi Lr_1}}\left[C_{k,l}I_k(\lambda_m r)+D_{k,l}K_k(\lambda_l r)\right]\cos\left(k\theta\right)\cos\left(l\frac{\pi}{L}z\right) \quad \text{or}\\ \sqrt{\frac{2}{\pi Lr_1}}\left[C_{k,l}I_k(\lambda_l r)+D_{k,l}K_k(\lambda_l r)\right]\sin\left(k\theta\right)\cos\left(l\frac{\pi}{L}z\right)\\ \qquad\qquad\qquad\

Then, it is possible to write:

$$\xi_p = \begin{cases} \sqrt{\frac{1}{2\pi L r_1}} \dfrac{1}{\log\left(\frac{r_1}{r_0}\right)} & \text{for} \quad k=l=0 \\ \\ \sqrt{\frac{2}{\pi L r_1}} \left\{ \dfrac{k}{r \sinh\left[k(\log r_1 - \log r_0)\right]} \right\} \cos(k\theta) \quad \text{or} \\ \sqrt{\frac{2}{\pi L r_1}} \left\{ \dfrac{k}{r \sinh\left[k(\log r_1 - \log r_0)\right]} \right\} \sin(k\theta) & \text{for} \quad k \geq 1, l=0 \\ \\ \sqrt{\frac{2}{\pi L r_1}} \left[C_{0,l}\lambda_l I_1(\lambda_l r_0) - D_{0,l}\lambda_l K_1(\lambda_l r_0) \right] \cos\left(l\frac{\pi}{L}z\right) & \text{for} \quad k=0, l \geq 1 \\ \\ \sqrt{\frac{2}{\pi L r_1}} \Big\{ A_{k,l} \left[\lambda_l I_{k+1}(\lambda_l r_0) + \frac{k}{r_0} I_k(\lambda_l r_0) \right] + B_{k,l} \left[-\lambda_l K_{k+1}(\lambda_l r_0) + \right. \\ \left. + \frac{k}{r_0} K_k(\lambda_l r_0) \right] \Big\} \cos(k\theta) \cos\left(l\frac{\pi}{L}z\right) \quad \text{or} \\ \sqrt{\frac{2}{\pi L r_1}} \Big\{ A_{k,l} \left[\lambda_l I_{k+1}(\lambda_l r_0) + \frac{k}{r_0} I_k(\lambda_l r_0) \right] + B_{k,l} \left[-\lambda_l K_{k+1}(\lambda_l r_0) + \right. \\ \left. + \frac{k}{r_0} K_k(\lambda_l r_0) \right] \Big\} \sin(k\theta) \cos\left(l\frac{\pi}{L}z\right) & \text{for} \quad k \geq 1, l \geq 1 \end{cases} \tag{4.104}$$

It can also be easily shown that:

$$\left\langle \frac{\partial \Psi_{p_{k,l}}}{\partial r}, \frac{\partial \Psi_{q_{m,n}}}{\partial r} \right\rangle_{L^2(S_0)} = \left\langle \frac{\partial \Psi_{p_{k,l}}}{\partial r}, \frac{\partial \Psi_{p_{k,l}}}{\partial r} \right\rangle_{L^2(S_0)} = \langle \xi_p, \xi_p \rangle_{L^2(S_0)} \tag{4.105}$$

Then it follows:

$$\langle \xi_p, \xi_p \rangle_{L^2(S_0)} = \begin{cases} \frac{r_0}{r_1} \left[\dfrac{1}{\log\left(\frac{r_1}{r_0}\right)} \right]^2 & \text{for} \quad k=l=0 \\ \\ \frac{r_0}{r_1} \left\{ \dfrac{k}{r_0 \sinh\left[k(\log r_1 - \log r_0)\right]} \right\}^2 & \text{for} \quad k \geq 1, l=0 \\ \\ \frac{r_0}{r_1} \left[C_{0,l}\lambda_l I_0(\lambda_l r_0) - D_{0,l}\lambda_l K_0(\lambda_l r_0) \right]^2 & \text{for} \quad k=0, l \geq 1 \\ \\ \frac{r_0}{r_1} \Big\{ C_{k,l} \left[\lambda_l I_{k+1}(\lambda_l r_0) + \frac{k}{r_0} I_k(\lambda_l r_0) \right] + \\ \\ + D_{k,l} \left[-\lambda_l K_{k+1}(\lambda_l r_0) + \frac{k}{r_0} K_k(\lambda_l r_0) \right] \Big\}^2 & \text{for} \quad k \geq 1, l \geq 1 \end{cases} \tag{4.106}$$

Equation(4.106) shows that the matrices of the linear systems given by Eqs.(4.25) and (4.65) are diagonal. Therefore, the unknowns β_p and β_p^m can be computed

explicitly, which is the main advantage of this new procedure. Then we have:

$$\beta_p = \begin{cases} -\frac{r_1}{r_0}\left[\log\left(\frac{r_1}{r_0}\right)\right]^2 \left\{\int_0^L \int_0^{2\pi} \left[f_0(\theta) f_0(z) \frac{h_{env}(Y - T_{env})}{K} + \right.\right. \\ \qquad \left. + Y \frac{\partial \Psi_{p_{0,0}}(r_0, \theta, z)}{\partial r}\right] r_0 d\theta dz + \\ \left. - \int_{r_0}^{r_1} \int_0^L \int_0^{2\pi} \left[\Psi_{p_{0,0}}(r, \theta, z) \frac{g}{K}\right] r dr d\theta dz \right\} \quad \text{for} \quad k = l = 0 \\ \\ -\dfrac{r_1 \left\{\int_0^L \int_0^{2\pi} \left[f_k(\theta) f_0(z) \dfrac{h_{env}(Y - T_{env})}{K} + Y \dfrac{\partial \Psi_{p_{k,0}}(r_0, \theta, z)}{\partial r}\right] r_0 d\theta dz\right\}}{r_0 \left\{\dfrac{k}{\sinh\left[k(\log r_1 - \log r_0)\right]}\right\}^2} \\ \qquad \text{for} \quad k \geq 1, l = 0 \\ \\ -\dfrac{r_1 \left\{\int_0^L \int_0^{2\pi} \left[f_0(\theta) f_l(z) \dfrac{h_{env}(Y - T_{env})}{K} + Y \dfrac{\partial \Psi_{p_{0,l}}(r_0, \theta, z)}{\partial r}\right] r_0 d\theta dz\right\}}{r_0 \left[C_{0,l} \lambda_l I_1(\lambda_l r_0) - D_{0,l} \lambda_l K_1(\lambda_l r_0)\right]^2} \\ \qquad \text{for} \quad k = 0, l \geq 1 \\ \\ -\dfrac{r_1 \left\{\int_0^L \int_0^{2\pi} \left[f_k(\theta) f_l(z) \dfrac{h_{env}(Y - T_{env})}{K} + Y \dfrac{\partial \Psi_{p_{k,l}}(r_0, \theta, z)}{\partial r}\right] r_0 d\theta dz\right\}}{r_0 \left\{C_{k,l}\left[\lambda_l I_{k+1}(\lambda_l r_0) + \frac{k}{r_0} I_k(\lambda_l r_0)\right] + D_{k,l}\left[-\lambda_l K_{k+1}(\lambda_l r_0) + \frac{k}{r_0} K_k(\lambda_l r_0)\right]\right\}^2} \\ \qquad \text{for} \quad k \geq 1, l \geq 1 \end{cases} \tag{4.107}$$

Finally, with the value of β_p, β_p^m and ξ_p, the temperature on the internal boundary surface can be computed using Eqs.(4.23) or (4.63), as a simple algebraic equation.

4.7 Estimation of the Internal Convection Heat Transfer Coefficient

According to the heat transfer theory, in a situation such as natural convection, boiling, condensation and radiation, the heat flux on the internal wall is not proportional to the temperature gap ΔT between the fluid and the wall, even if the fluid parameters are kept constant [57]. However, in case of single-phase forced convection, the heat flux is assumed to be proportional to the temperature gap according to the Newton's Law of Cooling. In this work, the numerical and real experiments

we have done allowed the use of the Newton's Law of Cooling. Therefore, the internal heat transfer coefficient is computed as the ratio of the internal heat flux and the temperature difference between the internal surface and the bulk fluid. For the numerical point of view, the bulk fluid temperature is supposed known and it is going to be measured through thermocouples in this work at the experimental analysis. Equation(4.108) gives the expression for $h_{|S_0}$, where N and M are the number of orthonormal basis functions used when steady state external temperature data are used.

$$h_{|S_0} = \frac{q_{|S_0}}{\Delta T} = \frac{-K\frac{\partial T}{\partial \mathbf{n}}}{T_{S_0} - T_b} = \frac{-K\sum_{q=0}^{(N_\theta N_z)} \mu_q \alpha_q}{\left[\sum_{q=0}^{(M_\theta M_z)} \xi_q \beta_q - T_b\right]} \tag{4.108}$$

However, when transient external temperature data are used to estimate the convection heat transfer, the expression of $h_{|S_0}$ is given by Eq.(4.109), where N_t is the finit number of time steps mentioned in the previous sections.

$$h_{|S_0} = \frac{q_{|S_0}}{\Delta T} = \frac{-K\frac{\partial T}{\partial \mathbf{n}}}{T_{S_0} - T_b} = \frac{-K\sum_{m=0}^{N_t}\sum_{q=0}^{(N_\theta N_z)} \mu_q \alpha_q^m}{\left[\sum_{m=0}^{N_t}\sum_{q=0}^{(M_\theta M_z)} \xi_q \beta_q^m - T_b\right]} \tag{4.109}$$

Chapter 5

Experimental Setup

This chapter is devoted to the description of the experimental procedure used to validate the methodologies developed in this thesis. The experiment setup employed in this work allowed the use of non-intrusive temperature measurements on the external wall of a duct by means of an infrared camera. These temperature measurements were considered as input data to the inverse problem formulated, in order to estimate the convection heat transfer coefficient. These experiments were realized by the student at the University of Parma in the Department of Industrial and Mechanical Engineering.

5.1 Infrared Thermography

Thermal measurements obtained by contact probes or sensores like thermocouples are often difficult to realize. In many cases, the insertion of these sensors causes disturbances, which can increase the difficulties associated to the analysis of the thermal problems investigated. Therefore, a technique that allows a contactless thermal measurement is of great advantage. The best methodology to this is the infrared thermography.

Infrared thermography originated in the 1800s when the English physicist William Herschel discovered thermal radiation outside the deep red in the visible electromagnetic spectrum of visible light, which was later called infrared.

In fact, this technique allows the remote detection of thermal energy in form of radiation emitted by any object in one of the InfraRed (IR) bands of the electromagnetic spectrum. By transforming this energy into a video signal, it is possible to obtain a surface temperature map representation of such object [58]. Thermal radiation can be observed from any solid, liquid or gas due to the fact that all materials at a temperature above the absolute zero (273 K) emit energy by means of electromagnetic waves.

Infrared thermography possesses, a great advantage over other techniques in

many application fields and for many different purposes, due to the fact that temperature variations are involved. Among the different Infrared Thermography applications fields, we can cite medicine, architecture, and maintenance, where it can be used for several types of diagnosis, material characterization, and assessment of procedures [59]. The aim of this chapter is to present how to exploit thermographic measurements on the external wall of a duct in order to evaluate the internal wall convective heat transfer through the solution of an inverse problem.

5.2 Description of the Experiment

In this work, the internal heat transfer coefficient of a pipe will be investigated under conditions of enhanced heat transfer. In order to increase the heat flux on the internal wall of the duct, some butterfly-shaped devices, as shematically shown on Fig.5.1, are inserted in the duct. A real picture of one of these devices is shown in Fig.5.2. This device is characterized by two "wings" and two "indentions", with a maximum diameter of 13 mm. The devices were positioned inside a stainless steel duct with 13 mm of internal diameter and 1.0 mm of wall thickness. The duct was three meters long and the butterfly-shaped devices were positioned at a distance of 300 mm one from each other, in order to not override the effects of two consequential inserts. The devices were maintained in a prescribed position through a central stick, as shown on Fig.5.3.

In this experiment, water was used as the working fluid. The stainless-steel pipe contained two fin electrodes, which were connected to a power supply. Through this, it was possible to investigate the heat transfer performance of the tube under a prescribed condition of uniform heat generated by the Joule effect in the wall. In order to minimize the heat transfer to the environment, the external wall of the tube was kept thermally insulated. The inlet fluid temperature was measured by a thermocouple placed before the heated section of the tube.

In order to create a test section for the thermographic measurements, a small portion of the external wall, around the position of the insert, was made accessible to a thermal imaging camera by removing the thermally insulating layer. The portion was coated with a thin film of high emissivity paint, increasing its emissivity near a black body. This thin paint layer changes the surface emissivity without affecting the heat conduction in the tube wall. The surface temperature distribution was acquired by a FLIR SC7000 camera, with a 640 x 512 pixel detector array, shown in Fig.5.4. Its thermal sensitivity, as reported by the instrument manufacturer, is 20 mK at 303 K, while its accuracy is ± 1 K. A schematic view of the infrared thermographic system arrangement is shown in Fig.5.5 .

To measure the temperature distribution around the test section surface, six

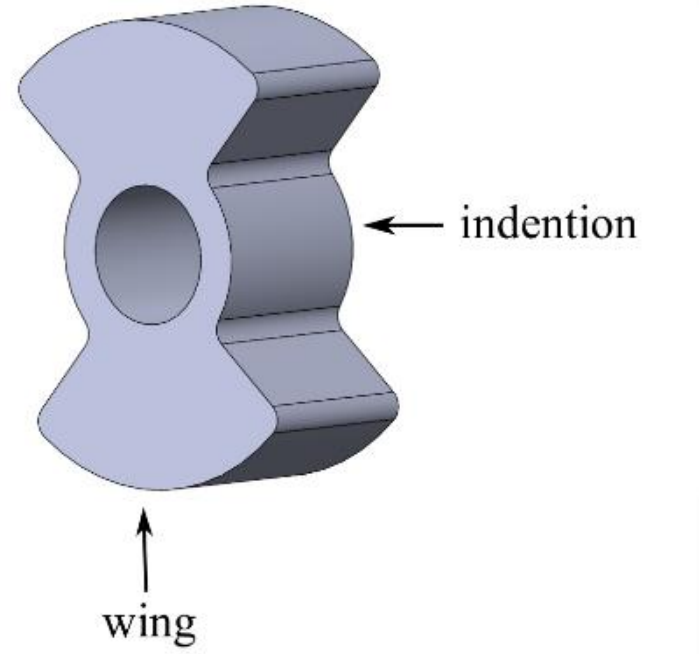

Figure 5.1: Schematic representation of one butterfly-shaped device

Figure 5.2: Real picture of the butterfly-shaped device

images were acquired, moving the infrared camera around the tube axis, as it can be seen in Fig.5.7. The camera was conveniently fixed on a support, in order to keep

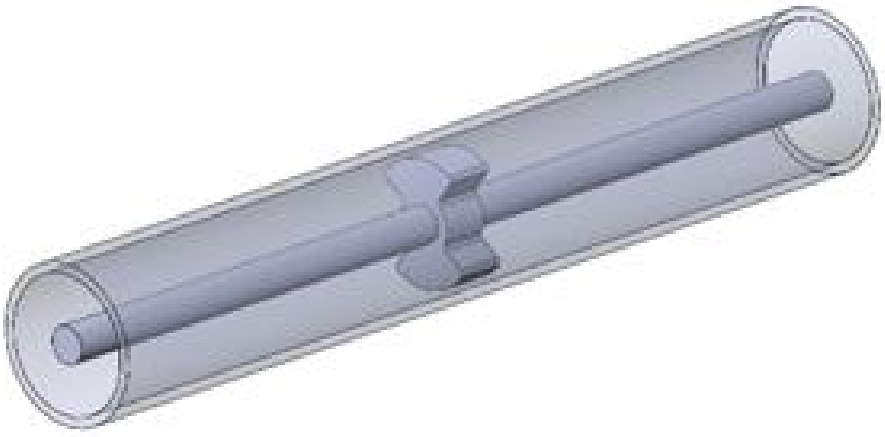

Figure 5.3: The butterfly-shaped device inserted into the duct

Figure 5.4: Infrared thermographic camera FLIR SC7000

the optical axis normal to the tube axis, therefore minimizing perspective artifacts. Fig.5.6 shows the different positions of the camera on the support which allowed the image acquisition around the tube. In the present experimental setup, to limit the viewing angle to be less than 30°, the surface was considered as a diffuse grey emitter [58]. The effective emissivity of the coating was estimated in situ by shooting a target at different known temperatures, and the value 0.99 was found.

The image processing procedure was complex by the fact that the observed target surface is not flat: common photo-plans can be produced from images of planar objects by image processing tools based on well-known equations of central projection, but this is not really an easy task when dealing with curved objects [60]. The image processing procedure adopted in this work was presented in [37]. It allows the rectification of optical deformations of the collected images caused by surface curvature: the acquired images were unwrapped and, thanks to adequate position references, fixed on the tube wall, were cropped and merged together to obtain

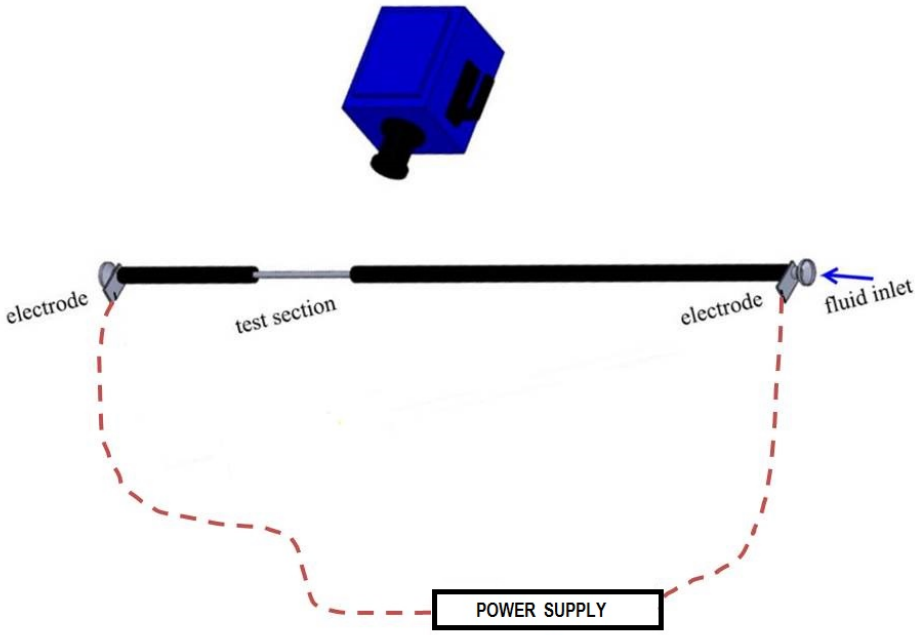

Figure 5.5: Sketch of the portion of the experimental setup

continuous temperature map on the tube wall. Fig.5.8 shows the final continuous temperature map.

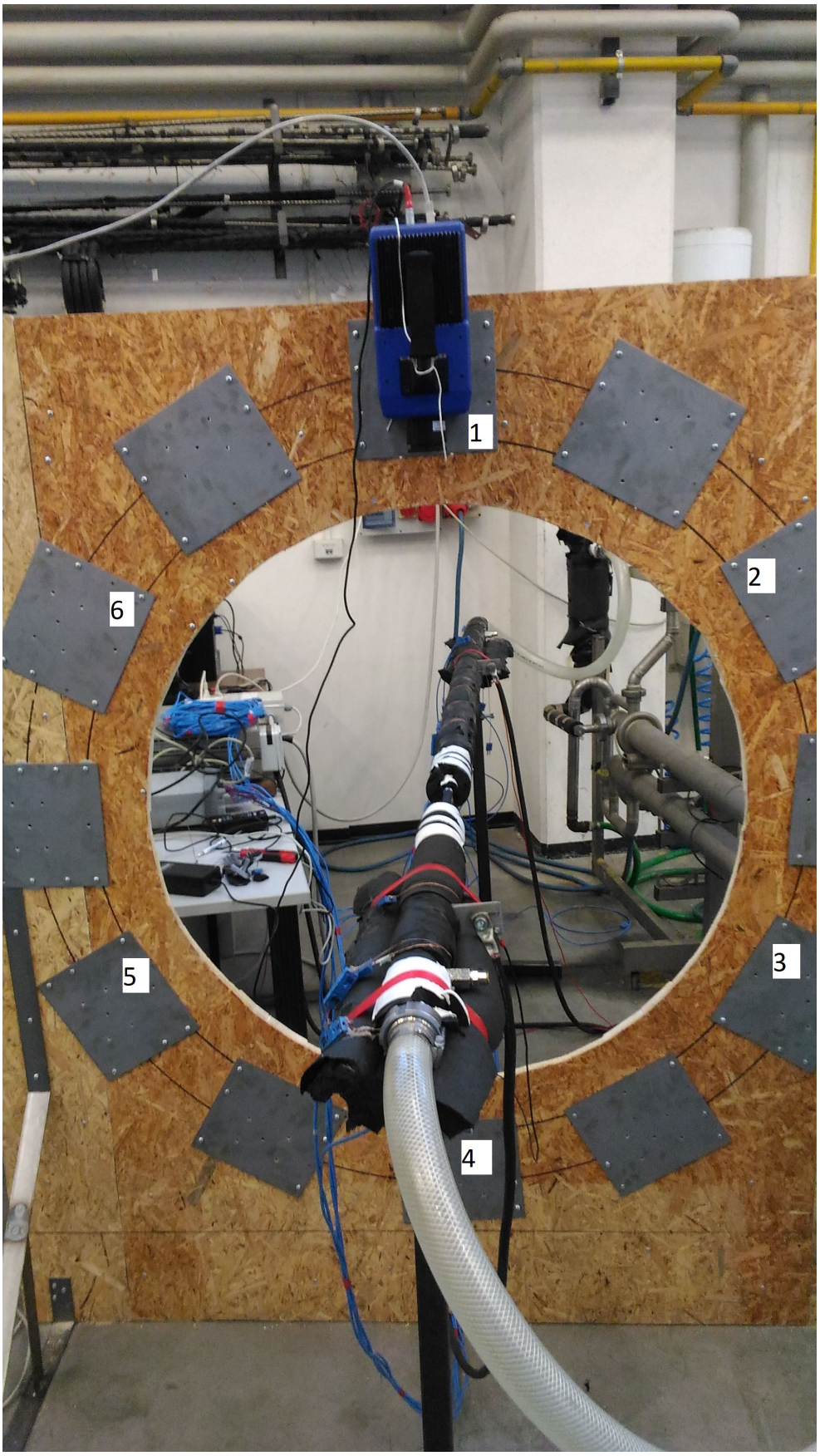

Figure 5.6: Camera mounted on the experimental structure to acquire the images.

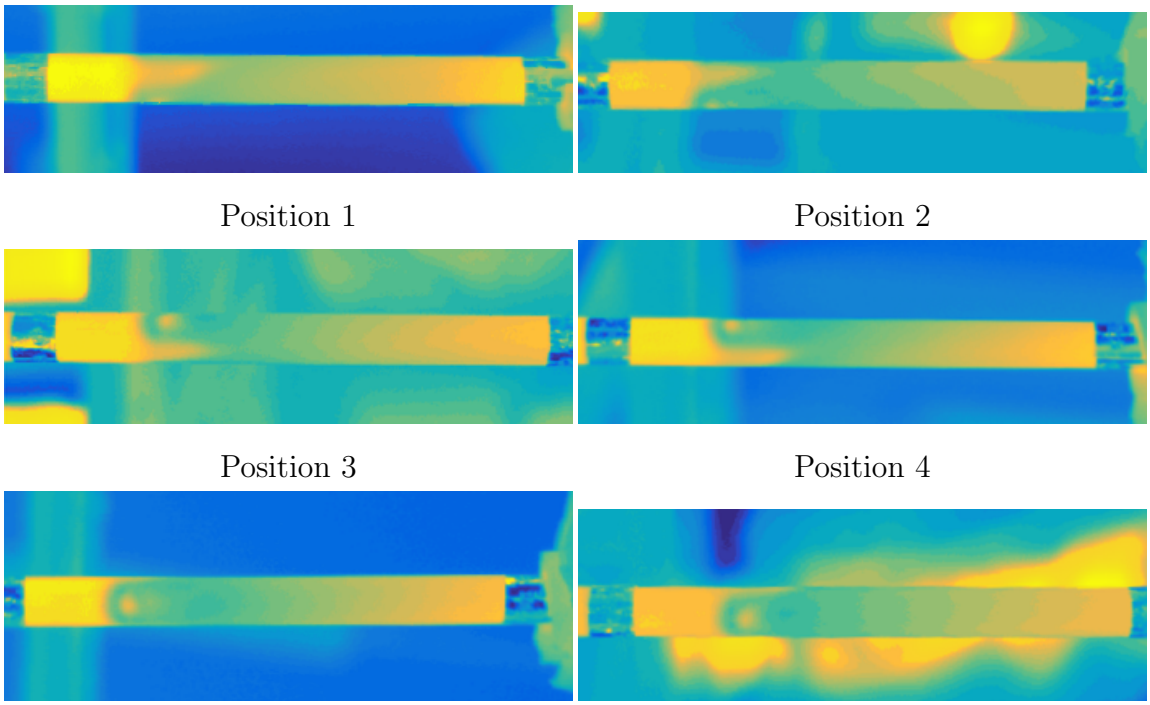

Figure 5.7: Six (6) images acquired by the camera, where the positions are identified in Fig.5.6.

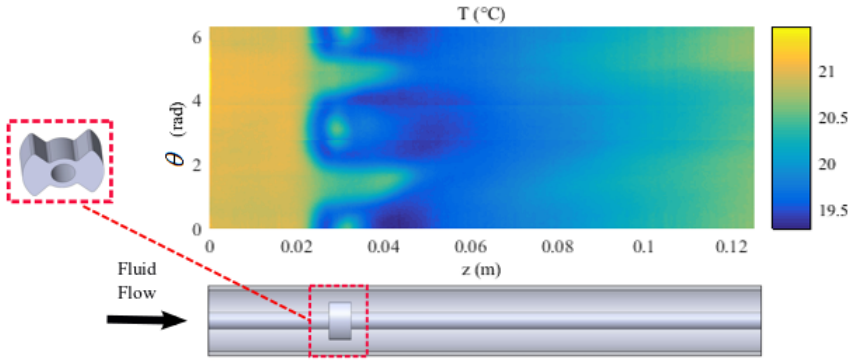

Figure 5.8: The final continuous temperature map.

In order to measure the inlet and outlet temperature through thermocouple, a data acquisition system was necessary. The comercial software LabVIEW was used for this purpose. Fig.5.9 shows the data acquisition set up, where the different components are:

(a) Computer;

(b) Interface of LabVIEW National Instruments;

(c) Temperature reference point device;

(d) Power supply;

(e) DAEQ National Instruments.

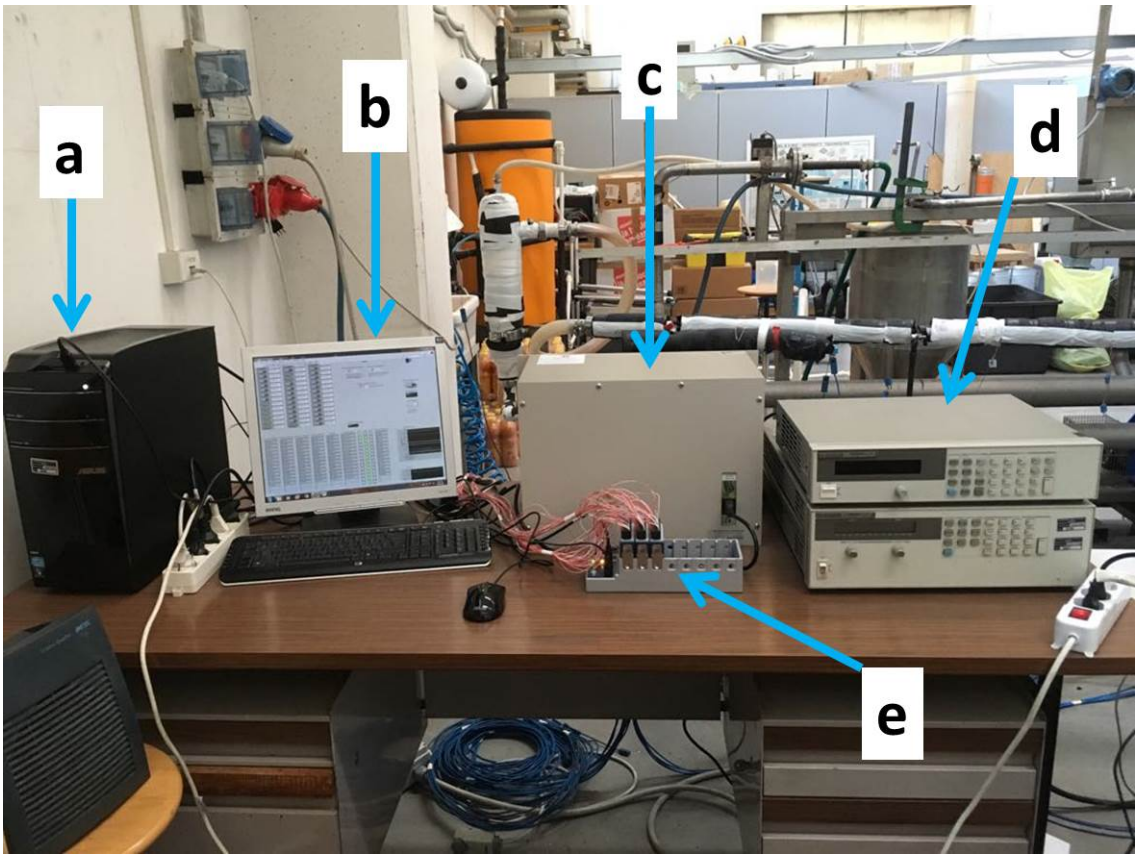

Figure 5.9: Data acquisition

Chapter 6

Results and Discussion

6.1 Steady State Numerical Verification Using Synthetic Data

Up to now the Reciprocity Functional Method is applicable to linear problems. Therefore, the material considered in this work, to numerically verify the method, is supposed to have a constant thermal conductivity in order to turn the problem linear. In fact, we considered a hollow cylinder of length L and internal and external radius are r_0 and r_1. The cylinder was made of stainless-steel (AISI 304), whose thermal conductivity is 15W/(m ^{o}C). Synthetic measurements were generated by solving the direct problem with different shapes for the unknown function. The presence of discontinuities in the profile of the convection heat transfer coefficient to be estimated is essential to the verication of the methodology hereby developed. So, Tab.6.1 and Fig.6.1 show different distributions of the local convective heat transfer coefficient and their analytical formulation tested in this work. In fact, we have tested heat transfer coefficient profiles which contain from one to three discontinuities (**h1**, **h2**, **h3**) and also profiles with smooth distributions (**h4**, **h5**). The effectiveness of the inverse problem solution methods depends highly on the kind of function that has to be estimated. consequently, testing the proposed approach for different profiles is fundamental for performing a robust comparison.

The external temperature T_{env} and the bulk internal temperature T_b were considered known and equal to 20^oC, while the external heat transfer coefficient h_1 was considered known and equal to 5.0W/(m^2 ^{o}C).

Table 6.1: Parameters of the problem for different tests cases.

Test case	g[W/m^3]	h_{env} [W/(m^2 ^{o}C)]	h_0 [W/(m^2 ^{o}C)]
h1	1x10^6	5	600 $\begin{cases} \text{for } \theta \in]2\pi/3, 4\pi/3] \\ \text{and } z \in [L/3, 2L/3] \end{cases}$ 120 $\begin{cases} \text{for } \theta \in]0, 2\pi/3] \bigcup]4\pi/3, 2\pi] \\ z \in]0, L/3] \bigcup]2L/3, L] \end{cases}$
h2	1x10^6	5	600 $\begin{cases} \begin{cases} \text{for } \theta \in]\pi/4, \pi/2] \\ \text{and } z \in [3L/4, 7L/8] \end{cases} \\ \text{or} \\ \begin{cases} \theta \in]3\pi/2, 7\pi/4] \\ \text{and } z \in [L/8, L/4] \end{cases} \end{cases}$ 120 $\begin{cases} \text{for } \theta \in]0, \pi/4] \bigcup]\pi/2, 3\pi/2] \bigcup]7\pi/4, 2\pi] \\ \text{and } z \in]0, L/8] \bigcup]L/4, 3L/4] \bigcup]7L/8, L] \end{cases}$
h3	1x10^6	5	600 $\begin{cases} \begin{cases} \text{for } (\theta \in]2\pi/17, 4\pi/17] \\ \text{and } z \in [L/8, L/4] \end{cases} \\ \text{or} \\ \begin{cases} \theta \in]16\pi/17, 18\pi/17] \\ \text{e } z \in [3L/4, 7L/8] \end{cases} \\ \text{or} \\ \begin{cases} \theta \in]30\pi/17, 32\pi/17] \\ \text{and } z \in [L/8, L/4] \end{cases} \end{cases}$ 120 $\begin{cases} \text{for } \theta \in]0, 2\pi/17] \bigcup]4\pi/17, 16\pi/17] \\ \bigcup]18\pi/17, 30\pi/17] \bigcup]32\pi/17, 2\pi] \\ \\ \text{and } z \in]0, L/8] \bigcup]L/4, 3L/4] \bigcup]7L/8, L] \end{cases}$
h4	1x10^6	5	$-480(\theta^2/(2\pi^2) + 2z^2/L^2) + 960\theta/(2\pi)$ $+z/l + 120$
h5	2x10^6	5	$-4880(\theta^2/(2\pi^2) + 2z^2/L^2) + 9760\theta/(2\pi)$ $+z/l + 120$

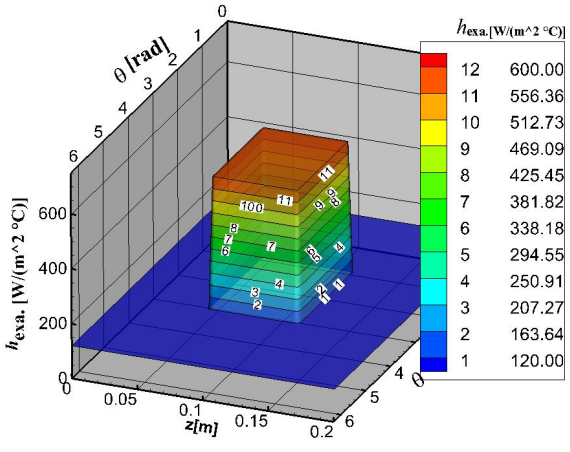

(**h1**)

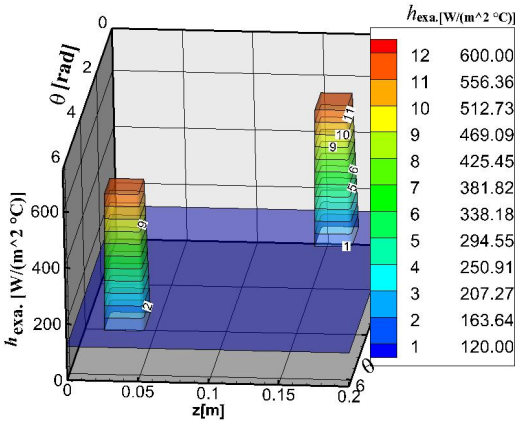

(**h2**)

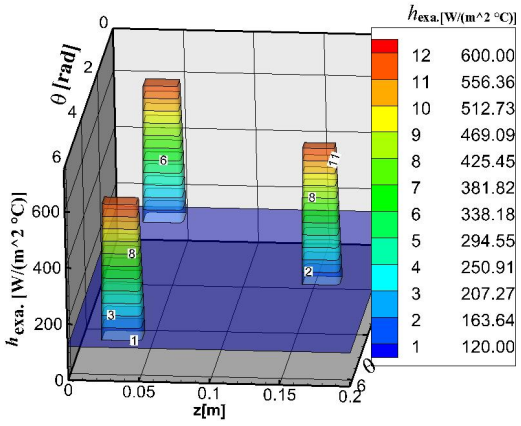

(**h3**)

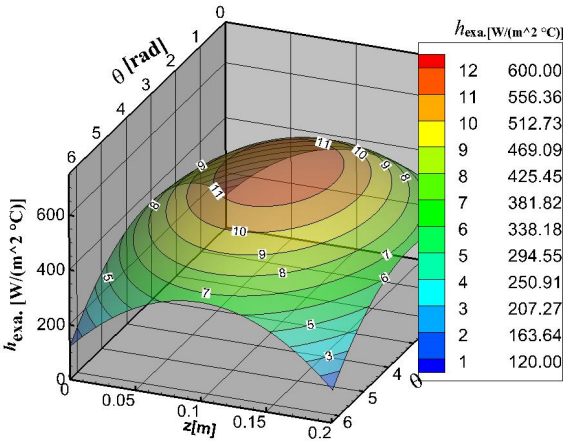

(**h4**)

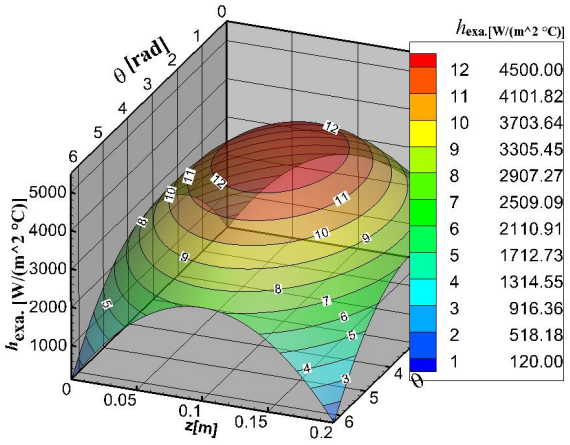

(**h5**)

Figure 6.1: Profiles of the convection heat transfer coefficient h_0 analyzed in the thesis for different tests cases

Regarding to the sensitivity analysis performed for an analogous case previously studied in [35], the main contributions to uncertainties in this problem are the conduction heat transfer coefficient K and the heat source g, while the uncertainties in h_1 and T_{env} are almost insignificant. In other words, the heat exchanged between the tube wall and the environment is negligible in comparison to that exchanged between the tube wall and the working fluid.

6.1.1 The Choice of the Number of Orthonormal Basis Functions

In the Reciprocity Functional Method, the number of orthonormal functions used in Eq.(4.108) and Eq.(4.109) is an important parameter, since it affects the smoothness of the solution. The choice of this number is similar to the selection of the optimal regularization parameters when dealing with the classical regularization methods for inverse problem solution [2, 3]. This work follows the discrepancy principle [3] analysis. In fact, the discrepancy principle states that the inverse problem solution is considered to be sufficiently accurate when the root mean square of the difference between the estimated and measured temperatures is close to the standard deviation of the noise in the raw measurements. This difference R is computed through Eq.(6.1) where M_{meas} is the number of measurements.

$$R = \frac{\|\mathbf{Y} - \mathbf{T}\|_2}{\sqrt{M_{meas}}} \tag{6.1}$$

The effectiveness of the Reciprocity Functional Method is also quantified in this work by analyzing the residual through the computation of the estimation error defined by Eq.(6.2). The values obtained for the cases tested in this work are reported in Tab.6.2, for synthetic measurements with and without Gaussian noises with standard deviation σ.

$$Er = \frac{\|(h)_{estimated} - (h)_{exact}\|_2}{\|(h)_{exact}\|_2} \tag{6.2}$$

In order to avoid checking the number of orthonormal basis function in each direction, the number of harmonics N_θ was chosen in relation to the number of harmonics N_z. That means that the characteristic wavelength of the highest harmonic along z coordinate has to be similar to the one of the highest harmonics along θ. Consequently, using Eqs.(4.80) and (4.81), we can derive the relation given by Eq.(6.3).

$$N_\theta \cong \frac{\pi r_1}{L} N_z \tag{6.3}$$

Finally, the criterion for choosing the right number of harmonics was based on the

Table 6.2: Relative error analysis for different test cases.

Test cases	**h1**	**h2**	**h3**	**h4**	**h5**
$Er_{h(\sigma=0^{\circ}\mathrm{C})}[\%]$	21.59	21.78	22.78	2.61	2.87
$Er_{h(\sigma=0.1^{\circ}\mathrm{C})}[\%]$	23.17	26.59	27.59	4.07	3.76
$Er_{h(\sigma=0.3^{\circ}\mathrm{C})}[\%]$	27.56	29.00	31.00	4.18	4.97
$Er_{h(\sigma=0.5^{\circ}\mathrm{C})}[\%]$	31.40	32.10	35.20	4.25	5.35

analysis of the root mean square of the temperature residuals and the estimation error distributions, as defined by Eq.(6.1) and Eq.(6.2) respectively, against the number of orthonormal functions along θ. An exemple for the test case **h5**, when the noise level in the measured temperature Y was 0.1°C is shown in Fig.6.2. The analysis in this case confirms that the number of harmonics ($N_\theta \approx 4$) chosen by the adopted criterion, established by assuming an accurate solution when R, given by Eq.(6.1), is equal to the standard deviation of the measurements, enables to minimize the estimation error given by Eq.(6.2). Therefore, this criterion is used to choose the number of orthonormal functions for all the cases tested in this work.

6.1.2 Steady-state Estimate without Noise in the Synthetic Data

To calculate the convection heat transfer coefficient using simulated temperature measurements without noise, different convection coefficient profiles (**h1,h2,...,h5**) were used to solve the direct problem, according to Tab.6.1. The solution of the direct problem allows to generate the synthetic temperature measurement on the outer wall of the tube, which is the input data to the Reciprocity Functional Method hereby formulated. A grid convergence analysis was performed, and the synthetic data were generated for the converged grid. The generated synthetic data were then considered to be the exact measured temperatures, $Y = T_{exa}$, on the external radius in order to estimate $h_{|S_0}$. Tab.6.3 presents the computational time for the solution of the direct and inverse problem for the test cases analyzed in this work. All the codes were built with FORTRAN 90 using some IMSL routines [61–63], on an Intel(R) Core(TM)i7-6700K CPU 4.00GHz Computer with 8.00GB RAM, working on a Windows7 64-bit System.

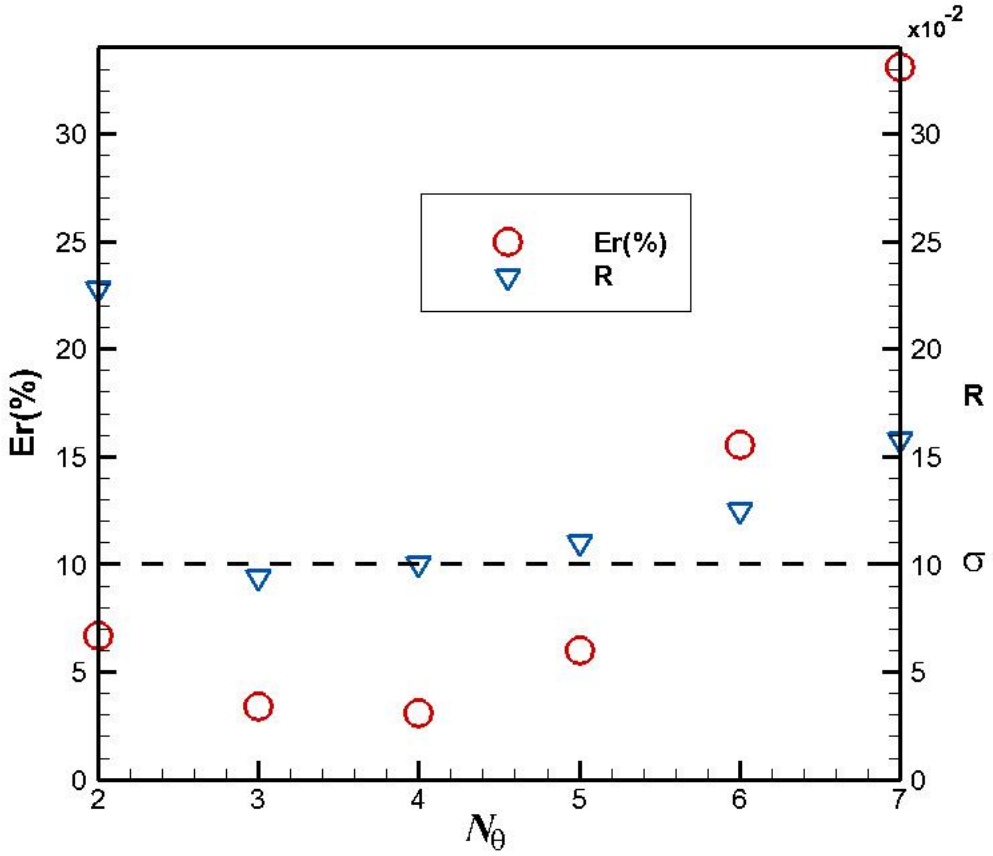

Figure 6.2: Root mean square of the difference between restored and measured temperatures ▽ and estimation error distributions ◯ against the number of orthonormal functions for case **h5** and standard deviation of measurements equal to 0.1°C.

Table 6.3: Computational time of the different test cases.

	CPU time the for direct problem [s]	CPU time for the inverse problem [s]
h1	15921	5
h2	15925	5
h3	15930	5
h4	15910	5
h5	15912	5

Case with One Discontinuity(h1)

The solution of Eq.(3.1), which is the direct problem, using the heat transfer distribution **h1**, as specified in the Tab.6.1, allows to generate the synthetic temperature measurements Y on the external wall.

These temperature data were used initially to estimate the internal heat flux $q_{|S_0}$. Fig.6.3a shows the estimated heat flux and Fig.6.3b represents its exact value. The comparison between the estimated and the exact values shows a good agreement as it can be observed.

In the sequence, the measurements Y were used to estimate the internal wall temperature $T_{|S_0}$. According to Fig.6.5a and Fig.6.5b, which are respectively the estimated and the exact internal wall temperatures, the estimates can also be considered good.

Then, using Eq.(4.108), the convection heat transfer h_{S_0} can be computed as it can be seen in Fig.6.7a (Fig.6.7b shows the exact value of h_0).

A quantitative comparison between the exact and estimated value of the heat flux, temperature and heat transfer coefficient on the inner radius can be observed in Figs.6.4, 6.6 and 6.8, where the absolute errors are shown. As it can be seen, the estimates are very good. From Tab.6.2, the overall relative error in this case was of 22%, with a computational time of 5 seconds perform the estimate.

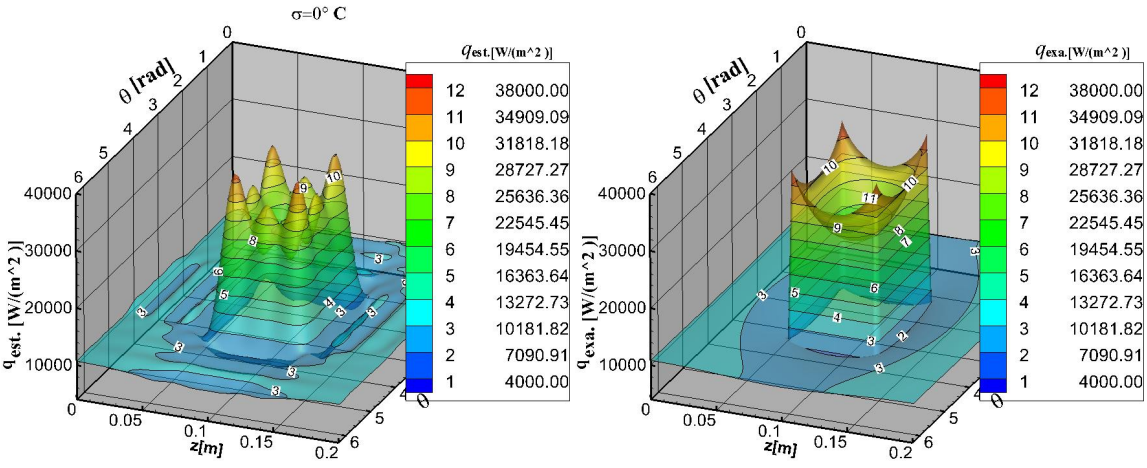

(a) (b)

Figure 6.3: (a)Estimated heat flux on S_0 (h1); (b)Exact heat flux on S_0 (h1)

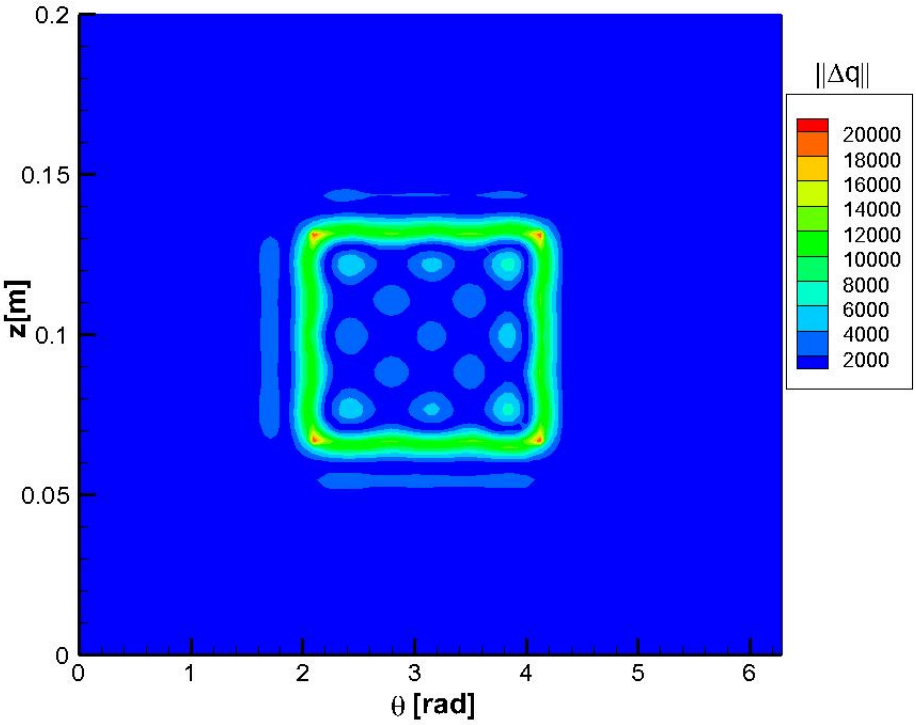

Figure 6.4: Absolute error between the exact and estimated heat flux for case h1

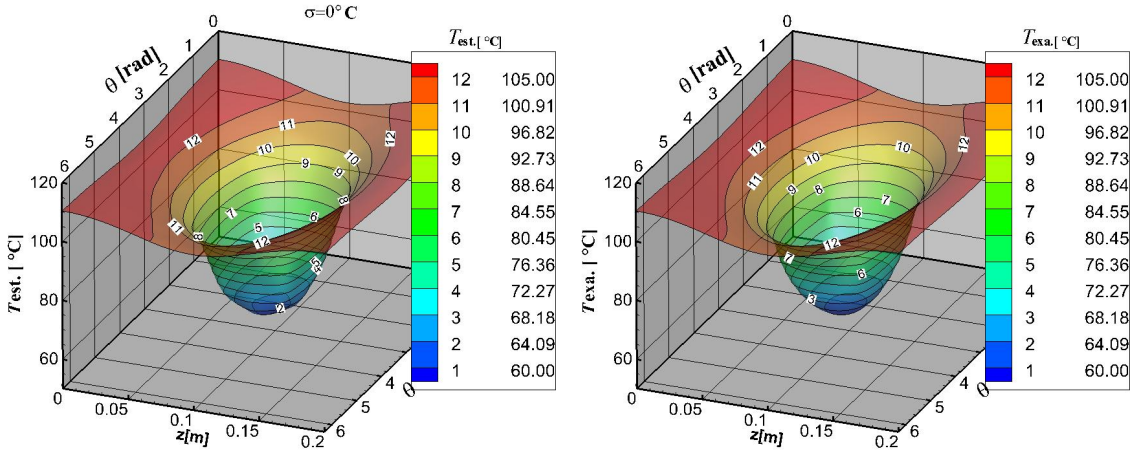

(a) (b)

Figure 6.5: (a)Estimated temperature on S_0 (h1); (b)Exact temperature on S_0 (h1)

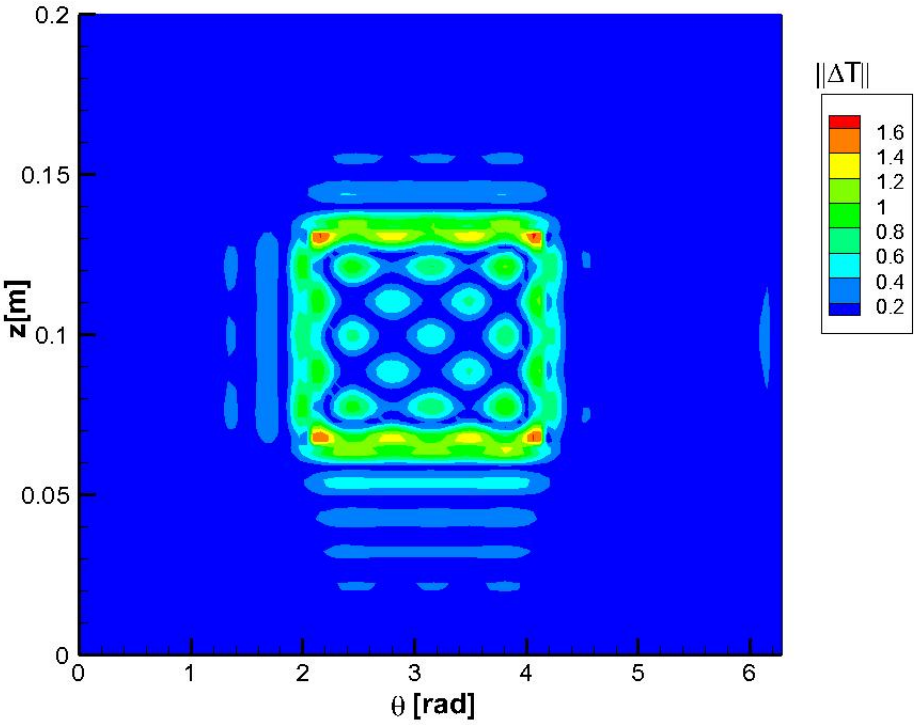

Figure 6.6: Absolute error between the exact and estimated temperature for case h1

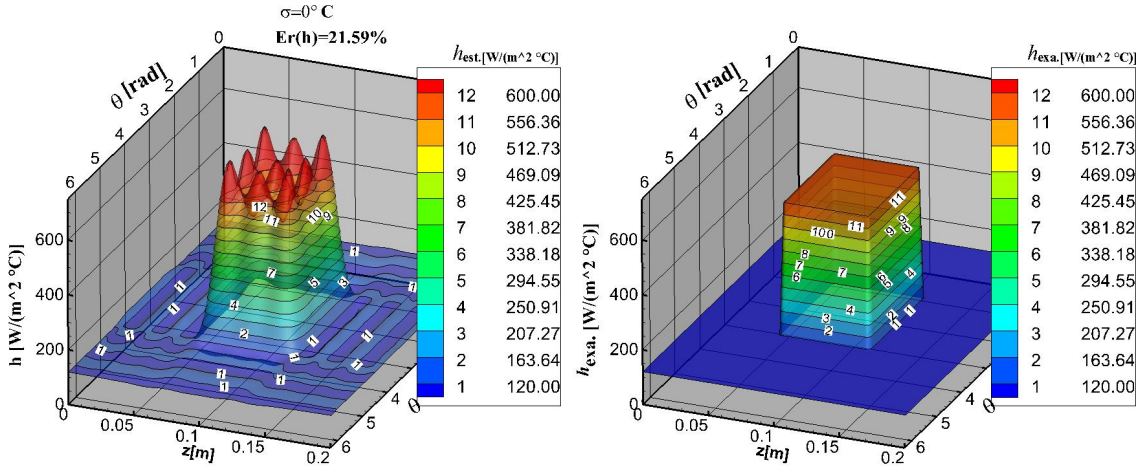

(a) (b)

Figure 6.7: (a)Estimated heat transfer coefficient h_0 on S_0 (h1); (b)Exact heat transfer coefficient h_0 on S_0 (h1)

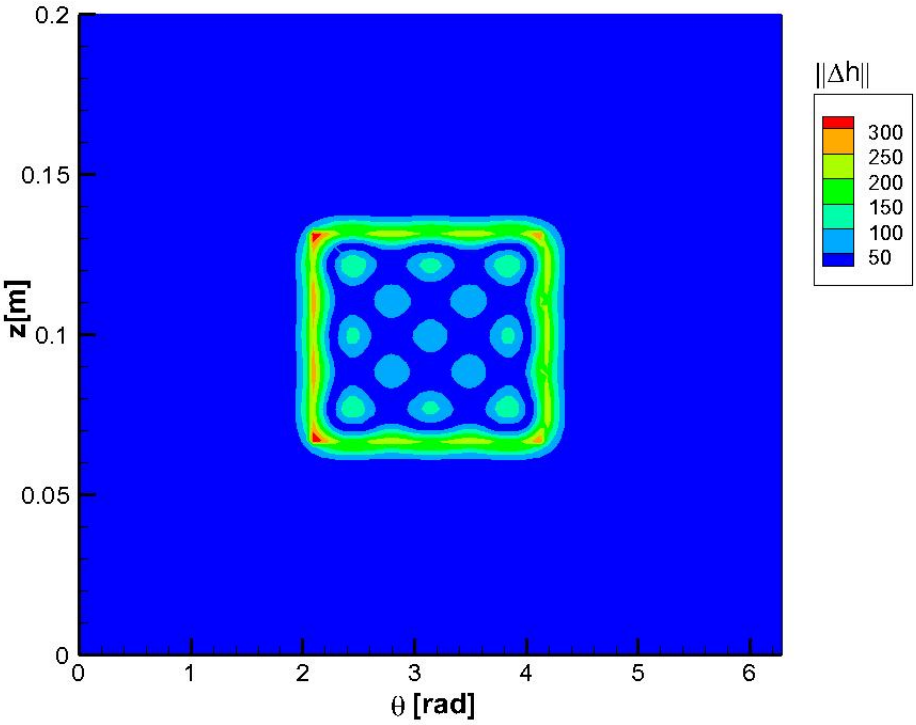

Figure 6.8: Absolute error between the exact and estimated heat transfer coefficient for case h1

Case with Two Discontinuities(h2)

In this section it will be shown the results regarding the test case with two discontinuities in the heat transfer coefficient profile. This profile was chosen to verify how the Reciprocity Functional Approach deals with the estimation of asymmetric functions. In fact, the profile distribution h2, as specified in Tab.6.1, is used for the solution of Eq.(3.1) in order to generate synthetic temperature measurements Y. The measurements Y are used as input to the RFM to estimate the heat flux and the internal wall temperature in order to compute the convection heat transfer. Fig.6.9 compares the estimated heat flux to its exact value while Fig.6.11 compares the estimated and exact internal wall temperature. These figures highlight a good estimate of both functions. In fact, Figs.6.10 and 6.12 present the absolute errors for the internal heat flux and temperature, where it can be seen that the estimates are good considering the high discontinuities in the function. As the heat flux and the internal wall temperature are available, the convection heat transfer in this test case can be calculated using Eq.(4.108). Fig.6.13 shows the estimated and exact profiles for this case. It can be seen that the two peaks are recovered, confirming the capability of the method to estimate these types of function. In fact, according to Tab.6.2, the overall relative error in this case is of 22%, which can be considered

good considering the non-intrusive character of the method as well as its very low computational time (5 seconds) to recover a highly discontinuous function. Fig.6.14 also shows the absolute error regarding the estimate of h for this case, where it can be seen that the results are good.

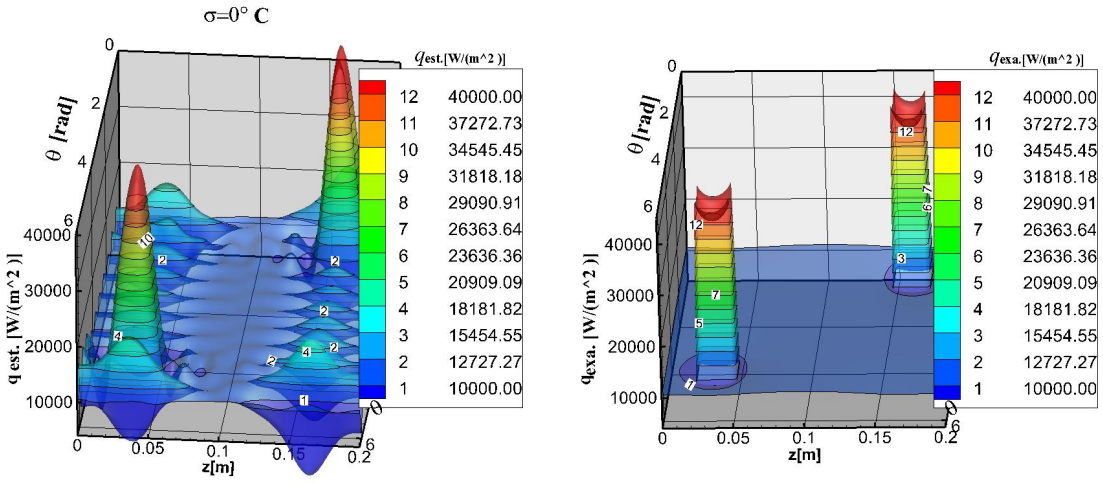

(a) (b)

Figure 6.9: (a) Estimated heat flux on S_0 (h2) ; (b)Exact heat flux on S_0 (h2)

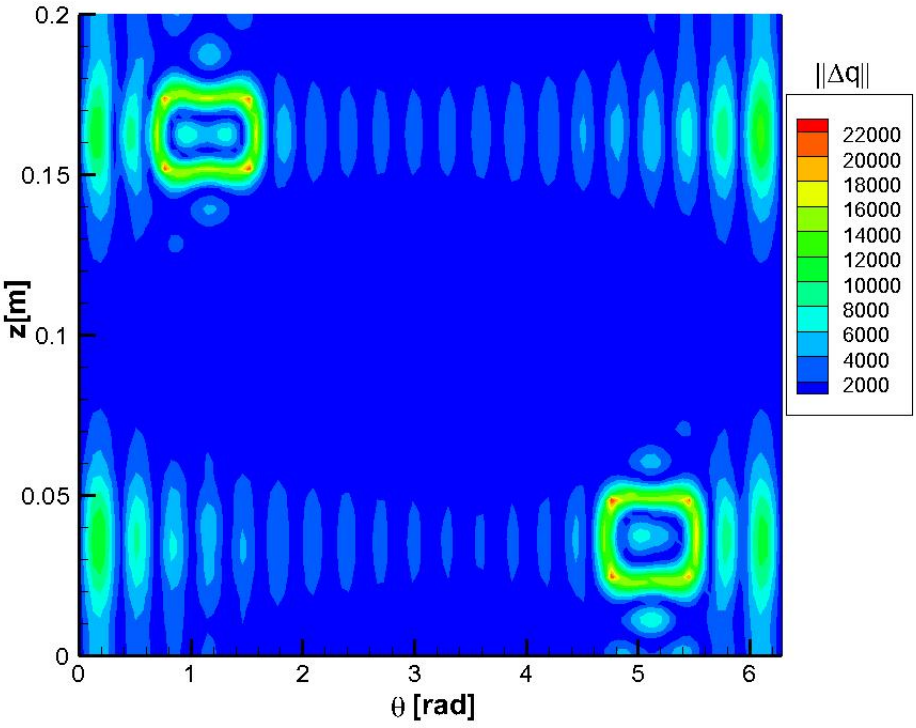

Figure 6.10: Absolute error between the exact and estimated heat flux for case h2

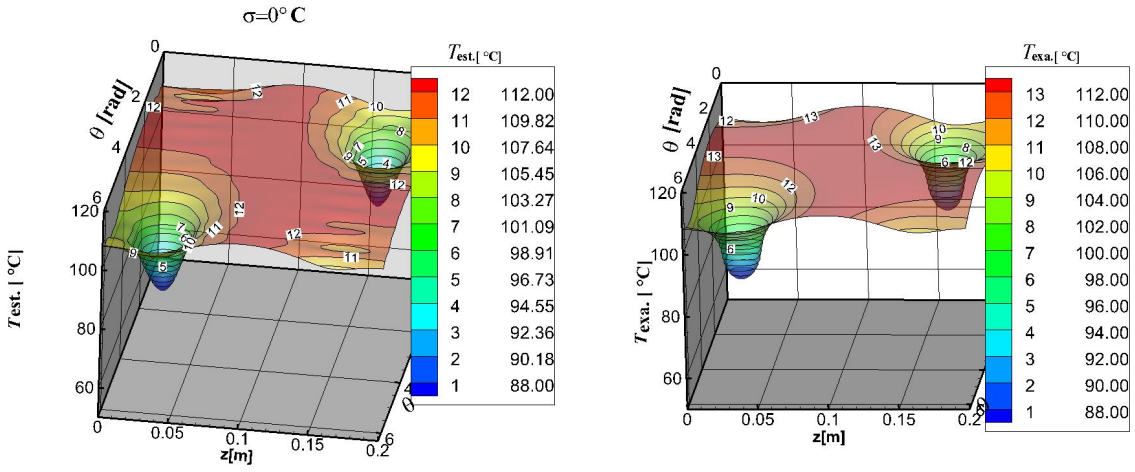

(a) (b)

Figure 6.11: (a)Estimated temperature on S_0 (h2); (b)Exact temperature on S_0 (h2)

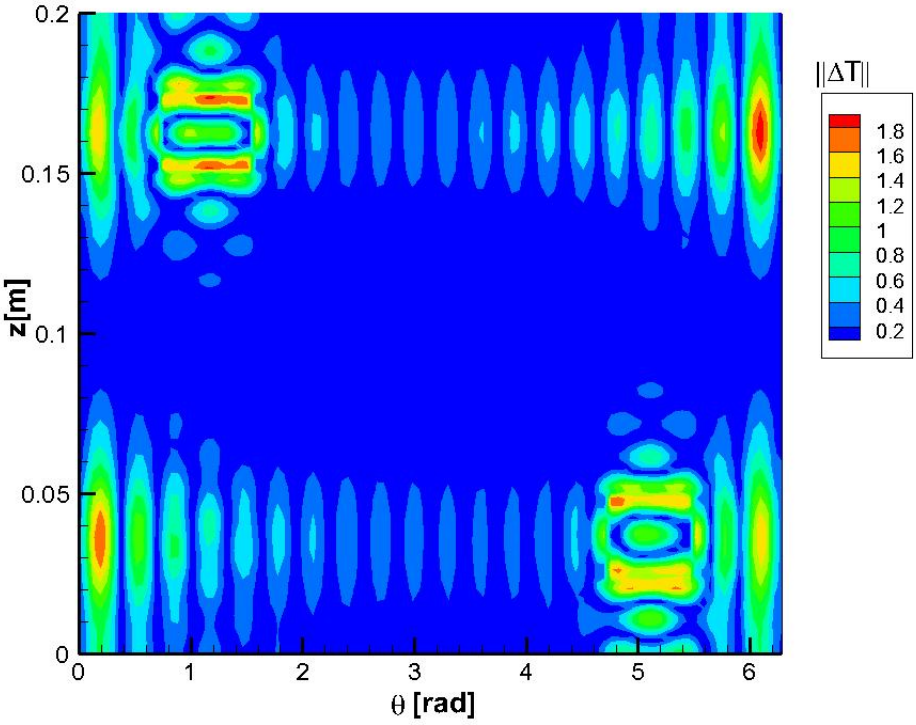

Figure 6.12: Absolute error between the exact and estimated temperature for case h2

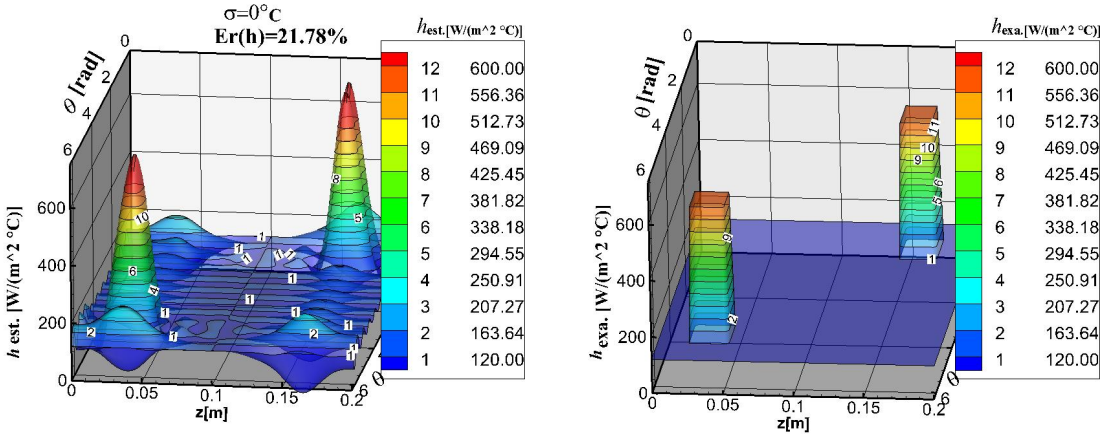

(a) (b)

Figure 6.13: (a)Estimated heat transfer coefficient h_0 on S_0 (h2); (b)Exact heat transfer coefficient h_0 on S_0 (h2)

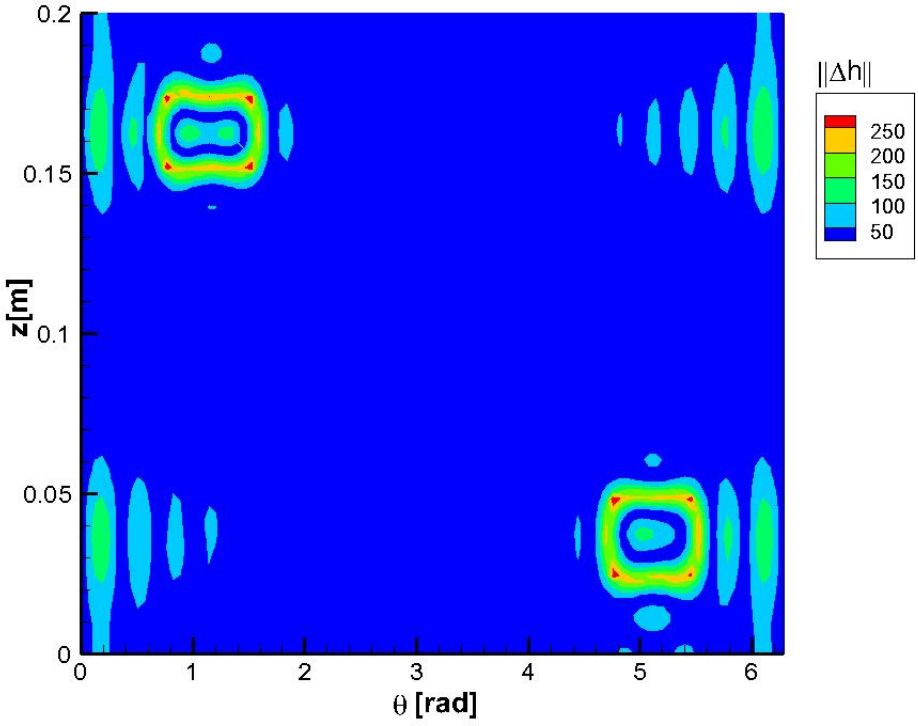

Figure 6.14: Absolute error between the exact and estimated heat transfer coefficient for case h2

Case with Three Discontinuities (h3)

The convection heat transfer h3, as specified in Tab.6.1, was tested with the main objective of challenging the Reciprocity Functional Method. In fact, the presence of three discontinuities is more difficult to recover than the previous cases.

Fig.6.15a presents the recovered profile of the heat flux, where it can be seen three peaks corresponding to three discontinuities as shown in the exact distribution presented in Fig.6.15b. The maximum value of the peaks is not well captured but the general shape was recovered well. A similar behaviour is observed in Fig.6.17, which represents the estimated and exact profile of the internal wall temperature. Fig.6.16 and 6.18 presents the absolute errors for the heat flux and temperature on the internal surface of the tube. As expected, these values are higher than the one presented in Figs.6.10 and 6.12, for the case h2, where only two peaks were considered. On Fig.6.19, it can be seen that the convection heat transfer coefficient was restored accurately, even though the individual profile of the heat flux and the temperature were not. In fact, Tab.6.2 shows that the overall relative error for this case was 23%, which is equivalent to the previous case h1 and h2. Fig.6.20 shows the absolute error for h_0 in this case.

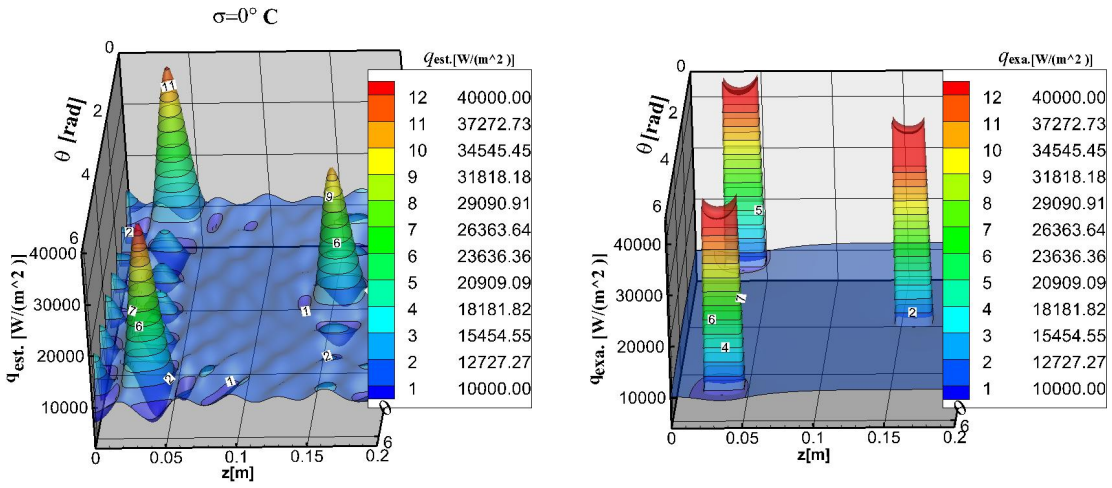

(a) (b)

Figure 6.15: (a)Estimated heat flux on S_0 (h3); (b)Exact heat flux on S_0 (h3)

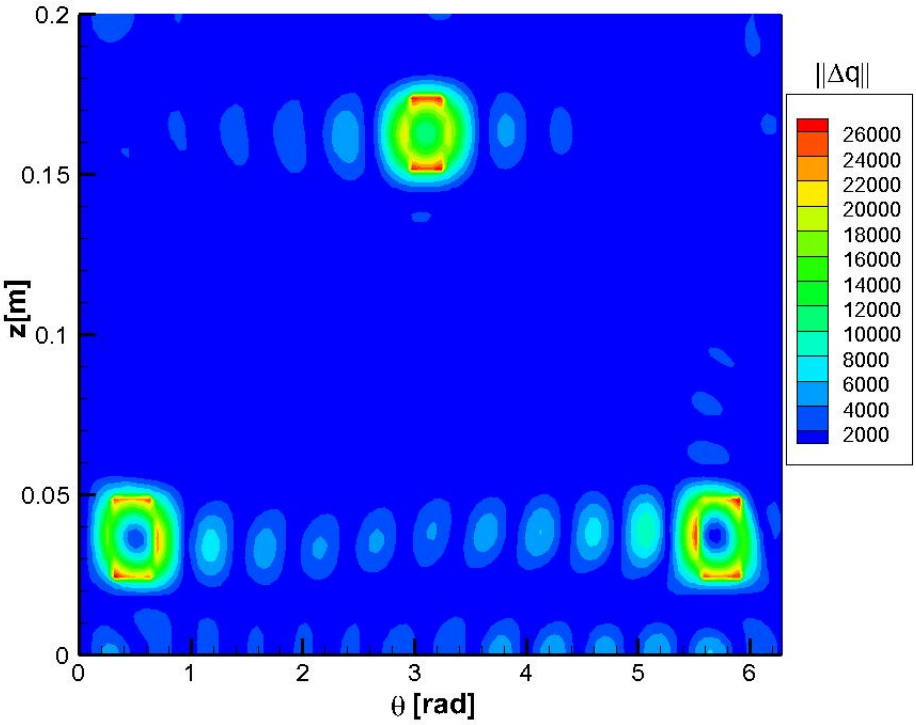

Figure 6.16: Absolute error between the exact and estimated heat flux for case h3

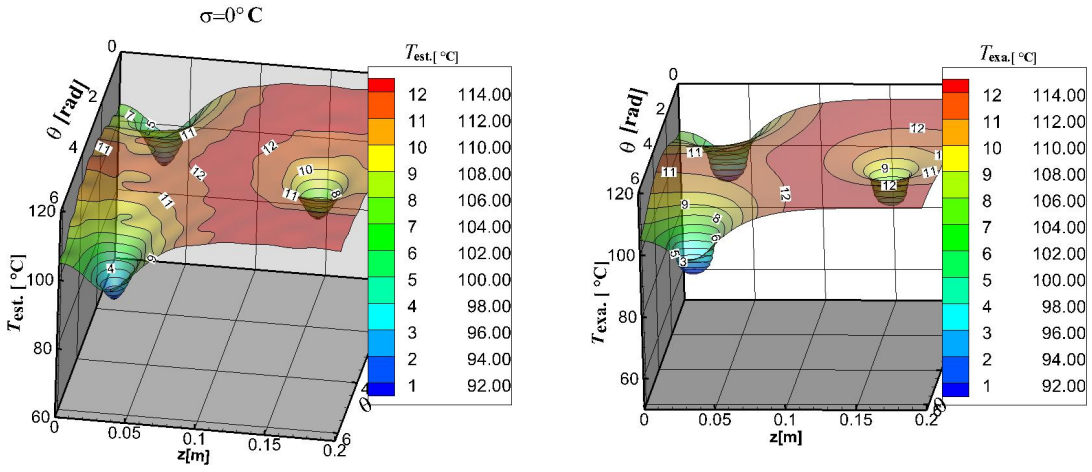

(a) (b)

Figure 6.17: (a)Estimated temperature on S_0 (h3); (b)Exact temperature on S_0 (h3)

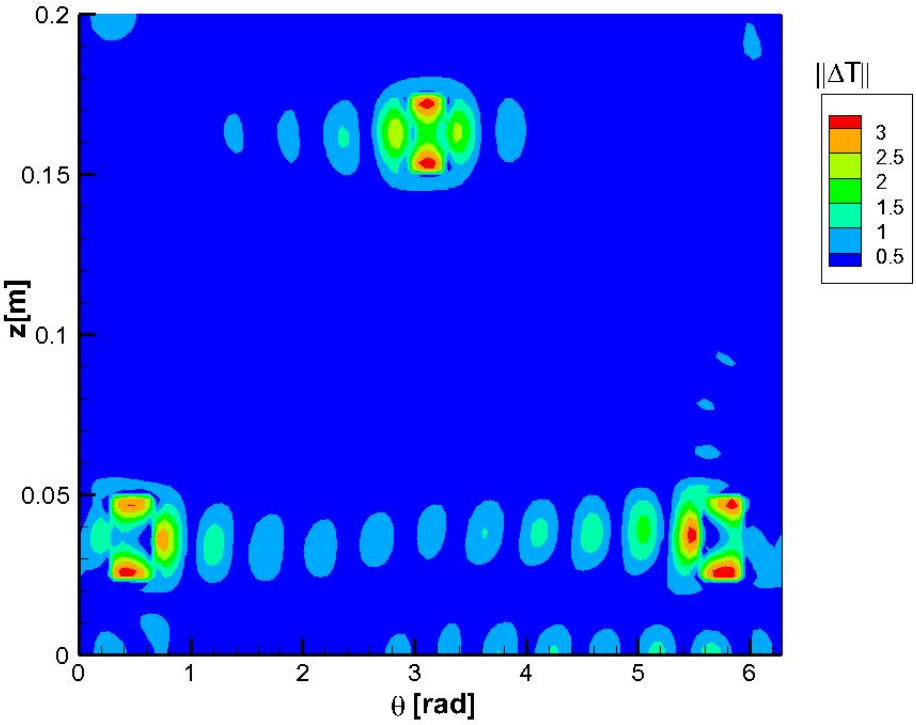

Figure 6.18: Absolute error between the exact and estimated temperature for case h3

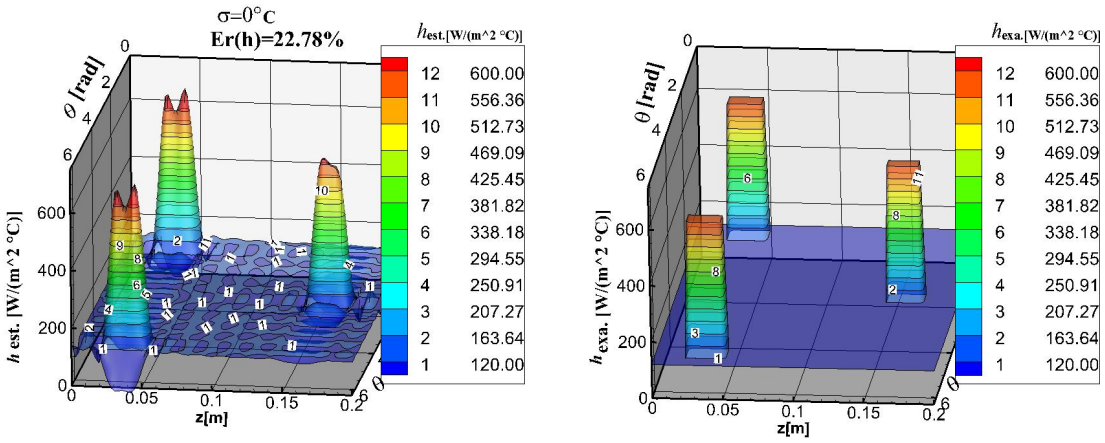

(a) (b)

Figure 6.19: (a)Estimated heat transfer coefficient h_0 on S_0 (h3); (b)Exact heat transfer coefficient h_0 on S_0 (h3)

Case with Smooth and Low Magnitude Profile (h4)

After checking the flexibility of the method through the estimate of functions with high level of discontinuity, two cases with smooth functions were tested. In

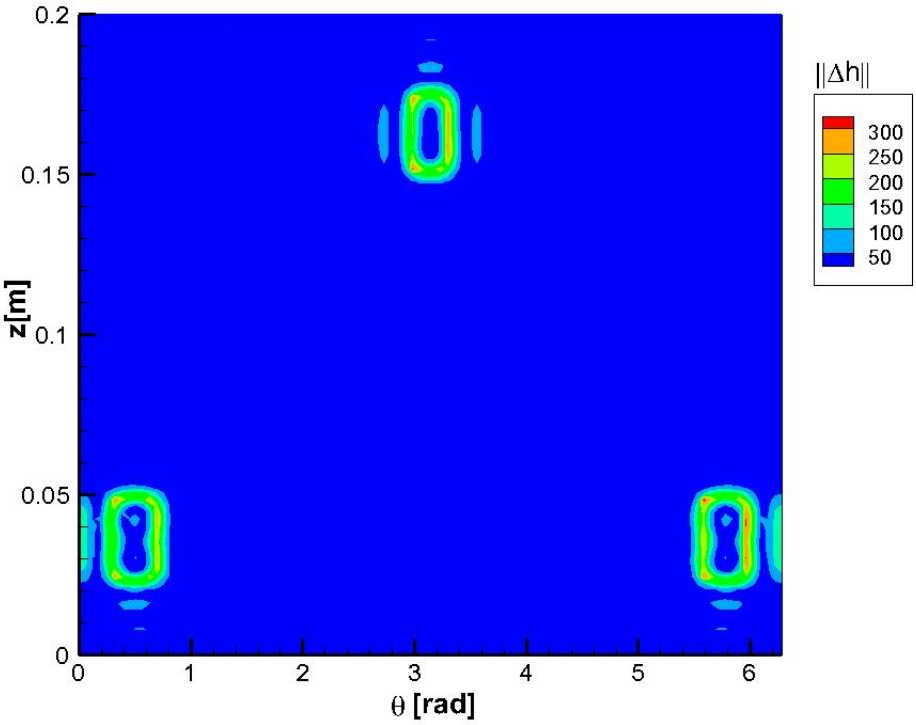

Figure 6.20: Absolute error between the exact and estimated heat transfer coefficient for case h3

this section we will show the results using the profile h4, as defined in Tab.6.1. This profile was used to generate synthetic measurements solving the direct problem. The estimate regarding the heat flux is presented in Fig.6.21, where a good agreement is observed by the comparison with the exact profile. Fig.6.23 presents the estimated internal wall temperature, while Fig.6.25 shows the restored heat transfer coefficient. It is observed a higher accuracy compared to the previous cases, since the profile of the heat transfer coefficient is smooth in this case.

In fact, the overall relative error for this case is only 2.6% (see Tab.6.2), which is one order of magnitude lower than the previous cases. Finally, Figs.6.22, 6.24 and 6.26, present the absolute errors for the heat flux, temperature and heat transfer coefficient for this case.

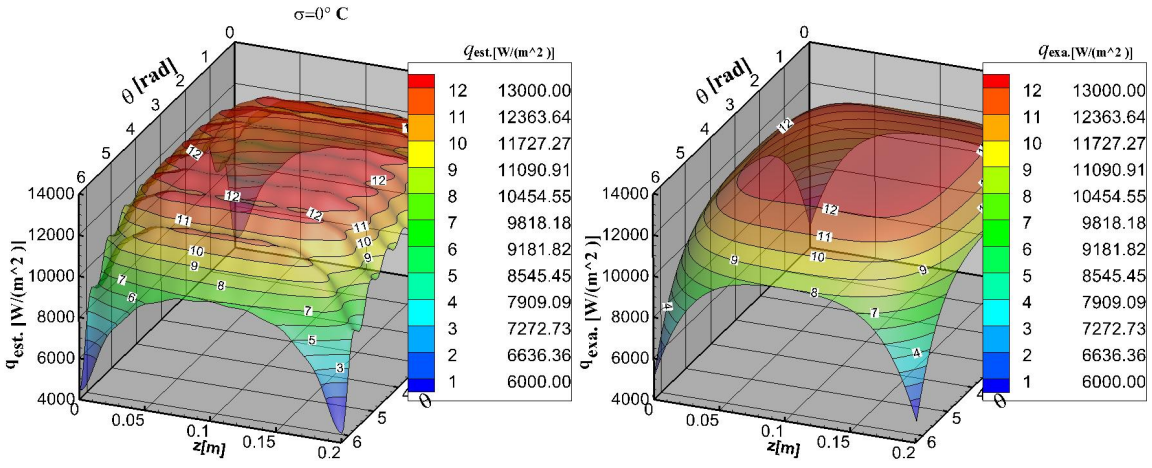

(a) (b)

Figure 6.21: (a)Estimated heat flux on S_0 (h4); (b)Exact heat flux on S_0 (h4)

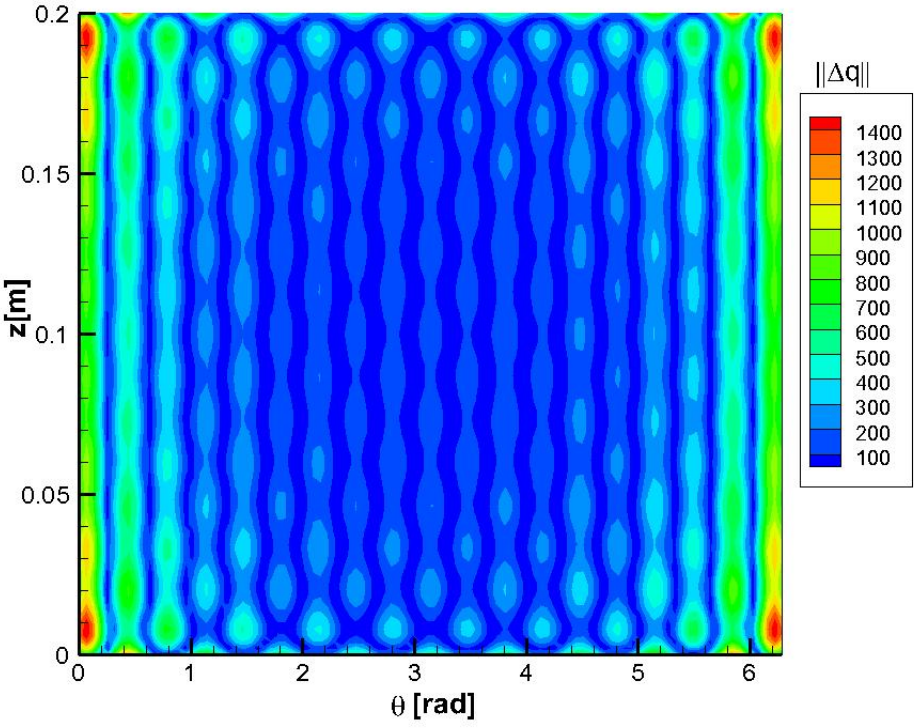

Figure 6.22: Absolute error between the exact and estimated heat flux for case h4

Case with Smooth and High Magnitude Profile (h5)

This case investigates the influence of the magnitude of the function being recovered on the methodology hereby used. Therefore, profile h5, which is also smooth, has a higher magnitude than h4 as it was shown in Tab.6.1. The estimated heat flux is presented in Fig.6.27, while the recovered internal wall temperature is presented

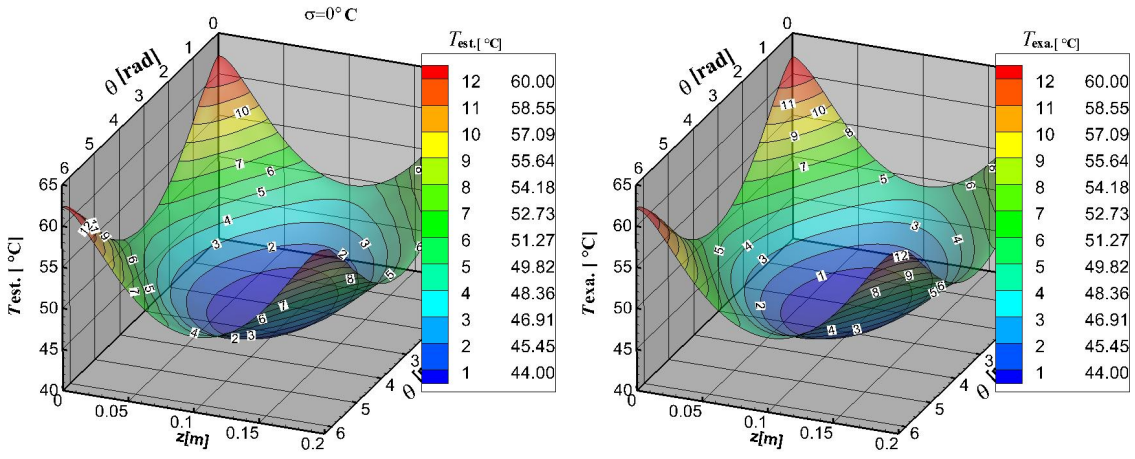

(a) (b)

Figure 6.23: (a)Estimated temperature on S_0 (h4); (b)Exact temperature on S_0 (h4)

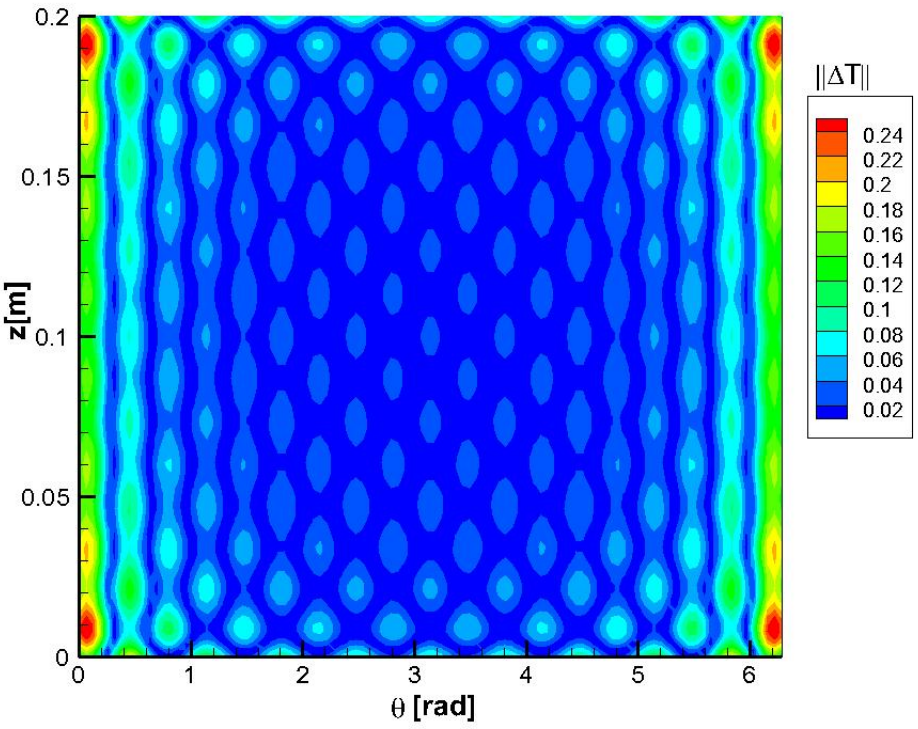

Figure 6.24: Absolute error between the exact and estimated temperature for case h4

in Fig.6.29. The estimated heat flux and the internal wall temperature are then used to compute the convection heat transfer coefficient as it can be seen in Fig.6.31.

As expected, results for this case are also much better than the ones for the discontinuous functions h1-h3. However, the fact that the maximum value of h in

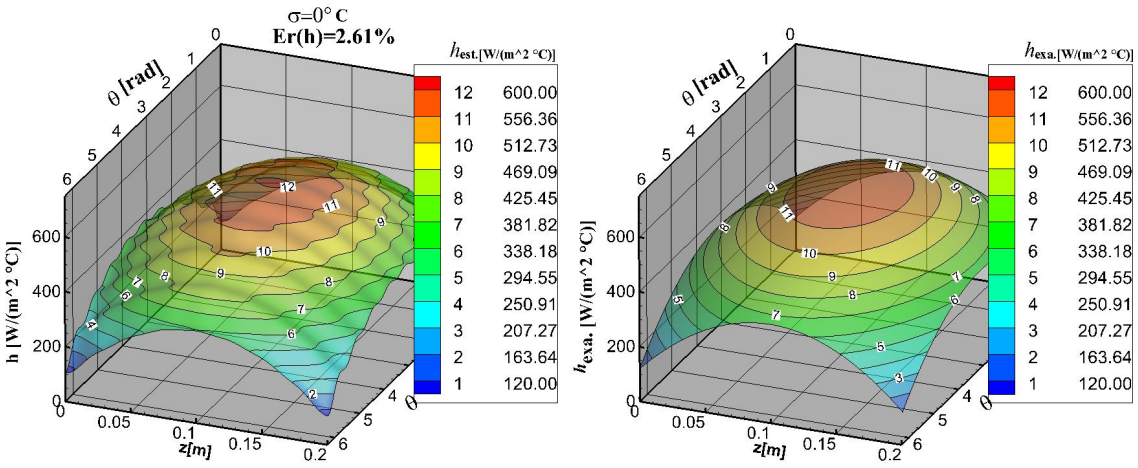

(a) (b)

Figure 6.25: (a)Estimated heat transfer coefficient h_0 on S_0 (h4); (b)Exact heat transfer coefficient h_0 on S_0 (h4)

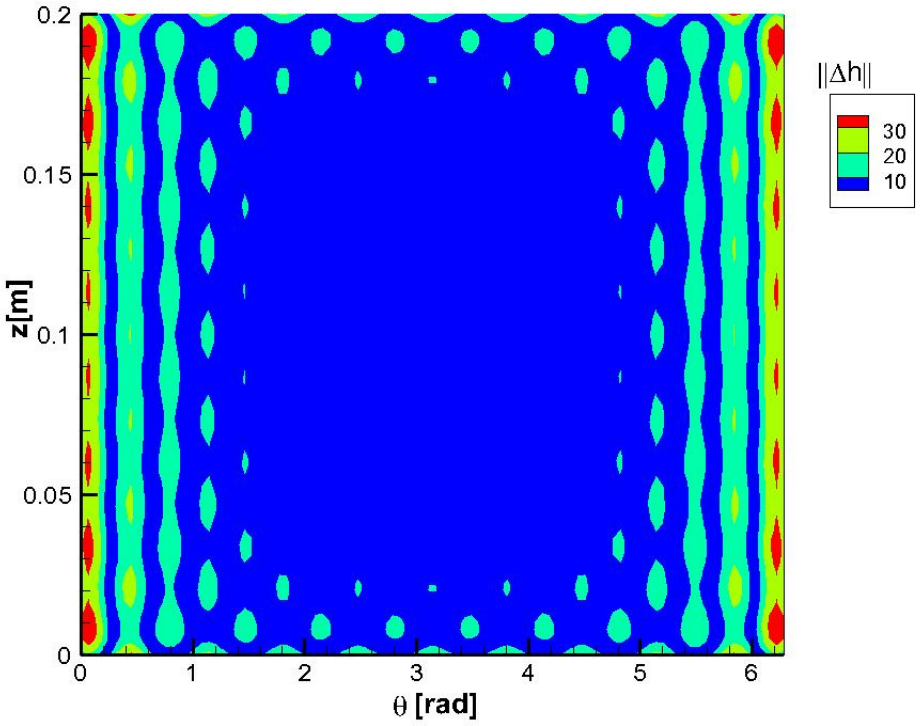

Figure 6.26: Absolute error between the exact and estimated heat transfer coefficient for case h4

this case is one order of magnitude higher than in case h4 (which was also smooth) caused a slightly increase in the the overall relative error, going from 2.6% for h4 to 2.9% for case h5 (see Tab.6.2). Finally Figs.6.28, 6.30 and 6.32 present the absolute

errors for the heat flux, temperature and internal convection coefficient for this case.

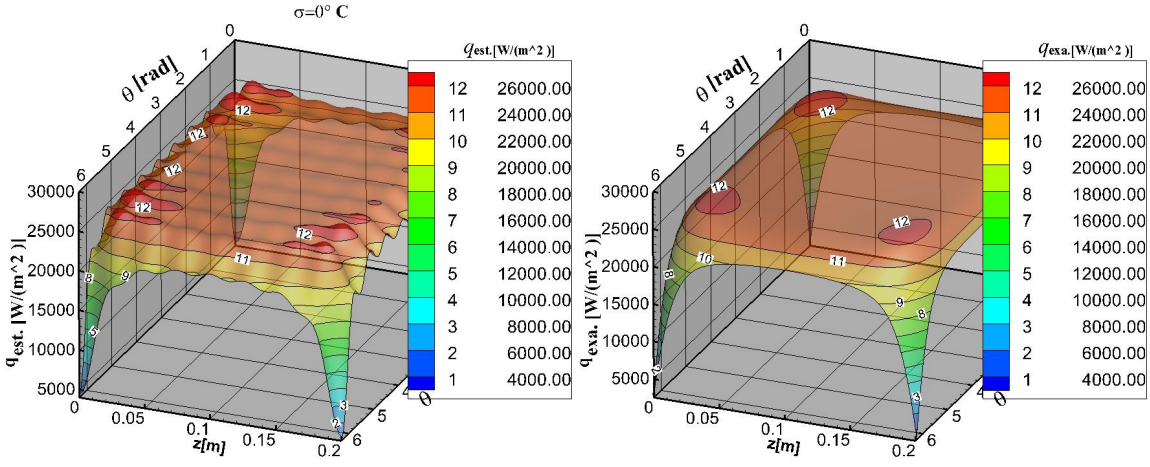

(a) (b)

Figure 6.27: (a)Estimated heat flux on S_0 (h5); (b)Exact heat flux on S_0 (h5)

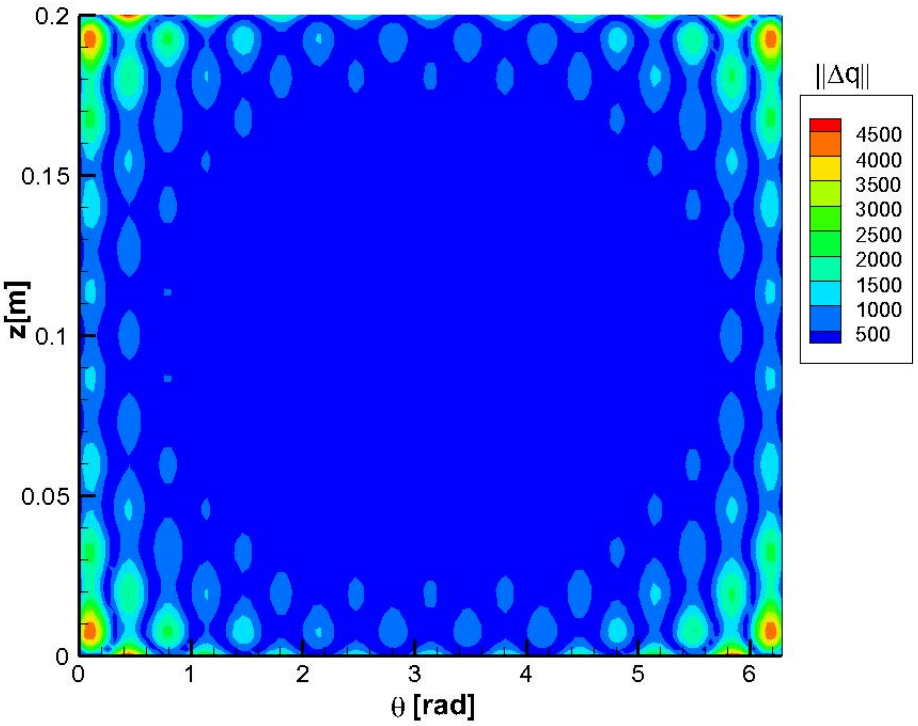

Figure 6.28: Absolute error between the exact and estimated heat flux for case h5

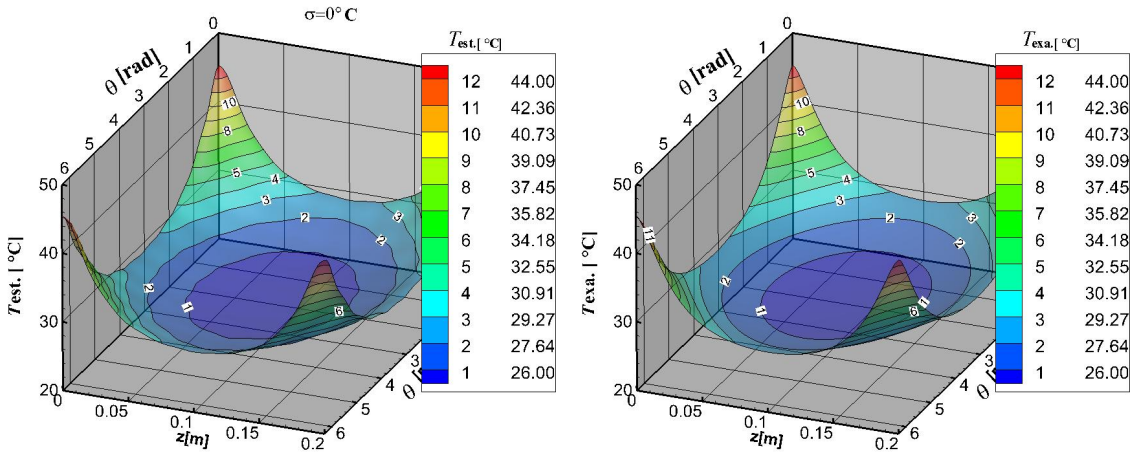

(a) (b)

Figure 6.29: (a)Estimated temperature on S_0 (h5); (b)Exact temperature on S_0 (h5)

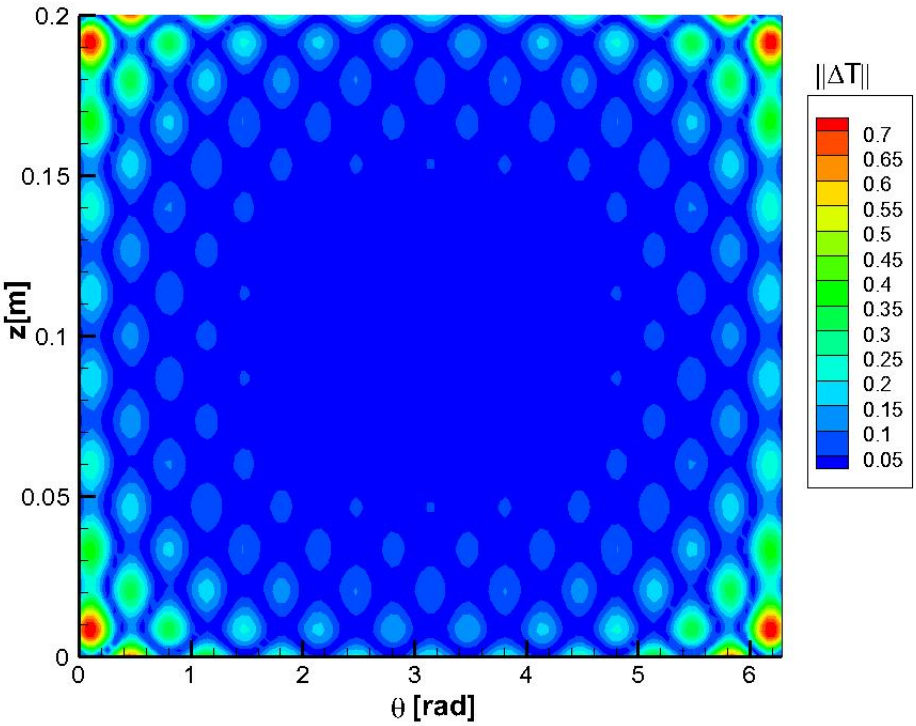

Figure 6.30: Absolute error between the exact and estimated temperature for case h5

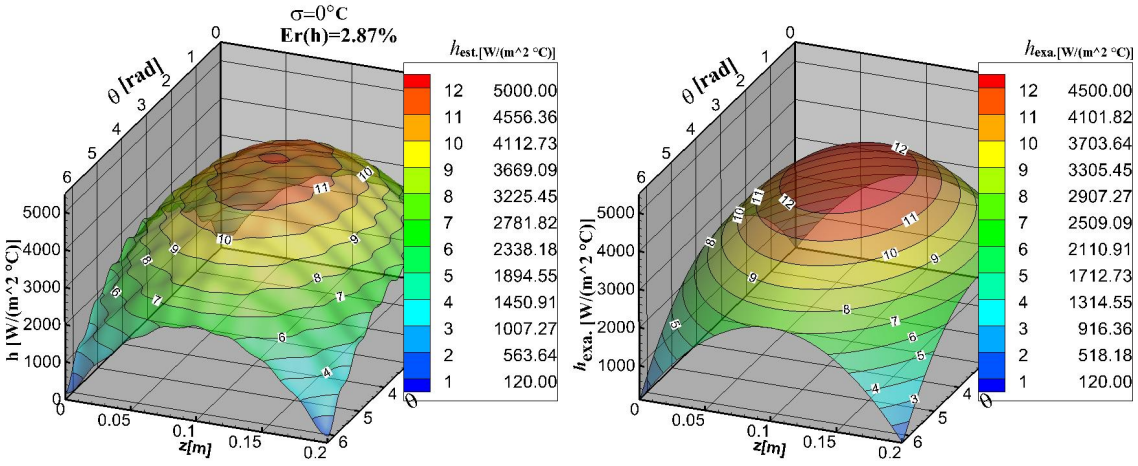

(a) (b)

Figure 6.31: (a)Estimated heat transfer coefficient h_0 on S_0 (h5); (b)Exact heat transfer coefficient h_0 on S_0 (h5)

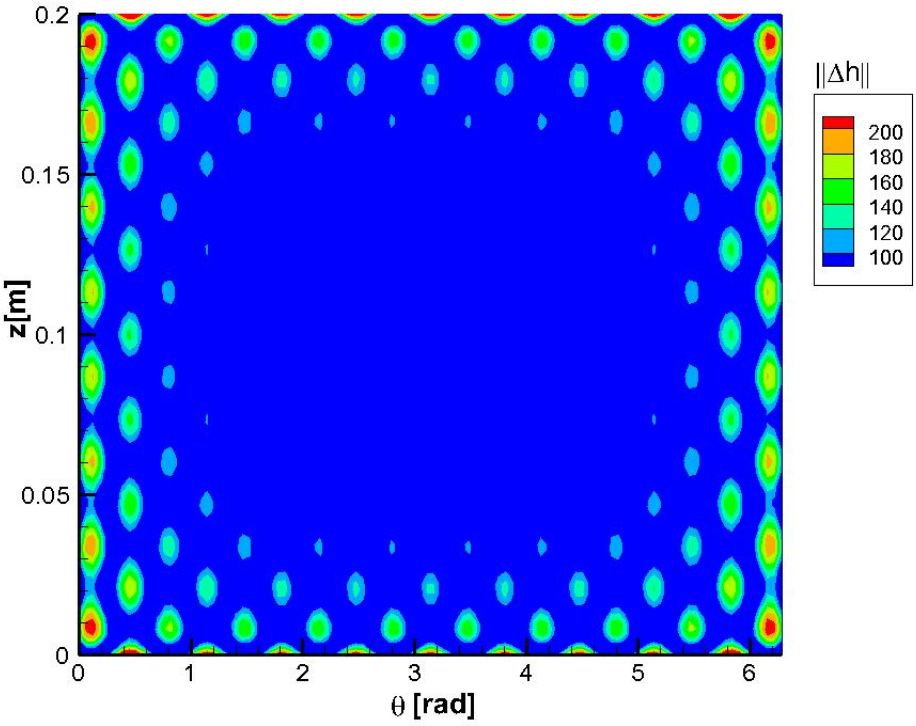

Figure 6.32: Absolute error between the exact and estimated heat transfer coefficient for case h5

6.1.3 Steady-state Estimate with Noise in the Synthetic Data

After the solution of the inverse problem using synthetic temperature measurement without noise it is fundamental to simulate test cases that contain noise in the synthetic data. Noisy temperature measurements were generated by adding a Gaussian noise to the external wall temperature T_{ext} according to the Eq.(6.4), where ϵ is a random variable with Gaussian distribution and σ is the standard deviation of the measurements. The random variable ε was generated by using the Box-Muller transformation [64] according to Eq.(6.5), where ω_0 and ω_1 are two uniformly distributed random numbers between 0 and 1.

$$Y = T_{ext} + \varepsilon\sigma \tag{6.4}$$

$$\varepsilon = \sqrt{-2ln(\omega_0)}\cos(2\pi\omega_1) \tag{6.5}$$

Case with One Discontinuity (h1: $\sigma = 0.1^oC$, $\sigma = 0.3^oC$, $\sigma = 0.5^oC$)

Regarding the test case h1, results concerning the heat flux are presented in Figs.6.33a-6.33d where synthetic temperature measurements with noise ($\sigma = 0.1^o$C, $\sigma = 0.3^o$C, $\sigma = 0.5^o$C) were adopted. The case h1 represents a uniform profile of heat transfer coefficient with an abrupt discontinuity, as reported in Tab.6.1. The internal wall temperature was also estimated and shown in Figs.6.34a-6.34d for each noise level. As the heat flux and the wall temperature are available on the boundary S_0, the convection heat transfer coefficient are computed and shown in Figs.6.35a-6.35d. The restored heat transfer coefficient, as well as the heat flux and the internal wall temperature, for the case with $\sigma = 0.1^o$C, agrees very well with the exact profile. The discontinuity is well captured even in the presence of noise with $\sigma = 0.3^o$C, as it can be observed in Figs.6.33c, 6.34c and 6.35c. However, the accuracy of the estimate deteriorates when the noise level increases. This fact can be observed in Figs.6.33d, 6.34d and 6.35d, which represents the heat flux, the internal wall temperature and the heat transfer coefficient estimated with $\sigma = 0.5^o$C. The estimation error values for h, reported in Tab.6.2, which were 23% for $\sigma = 0.1^o$C, 28% for $\sigma = 0.3^o$C and 31% for $\sigma = 0.5^o$C, confirm this observation.

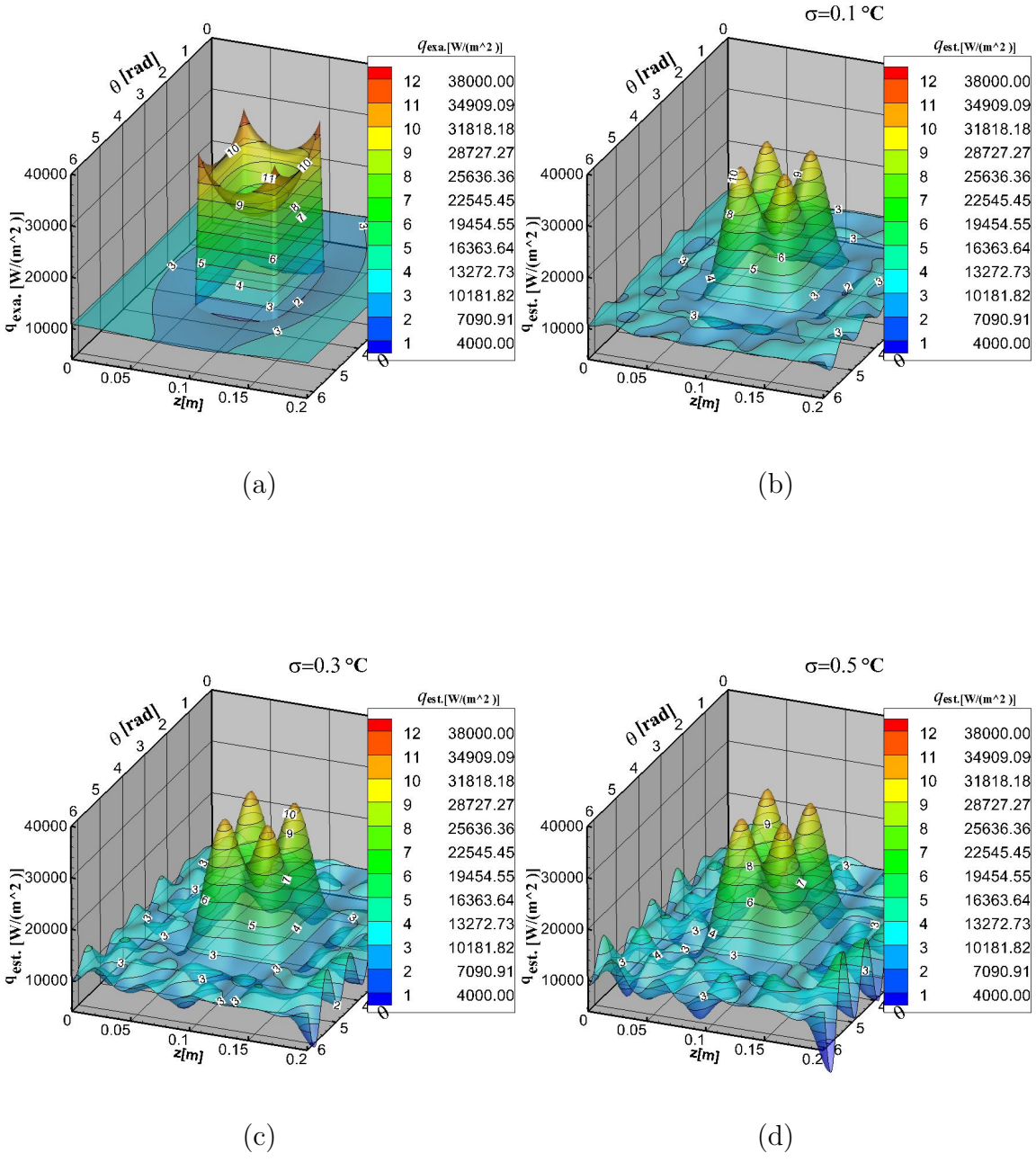

(a) (b)

(c) (d)

Figure 6.33: (a)Exact heat flux on S_0 (h1); (b)Estimated heat flux on S_0 with $\sigma = 0.1^o$C (h1); (c)Estimated heat flux on S_0 with $\sigma = 0.3^o$C (h1); (d)Estimated heat flux on S_0 with $\sigma = 0.5^o$C (h1)

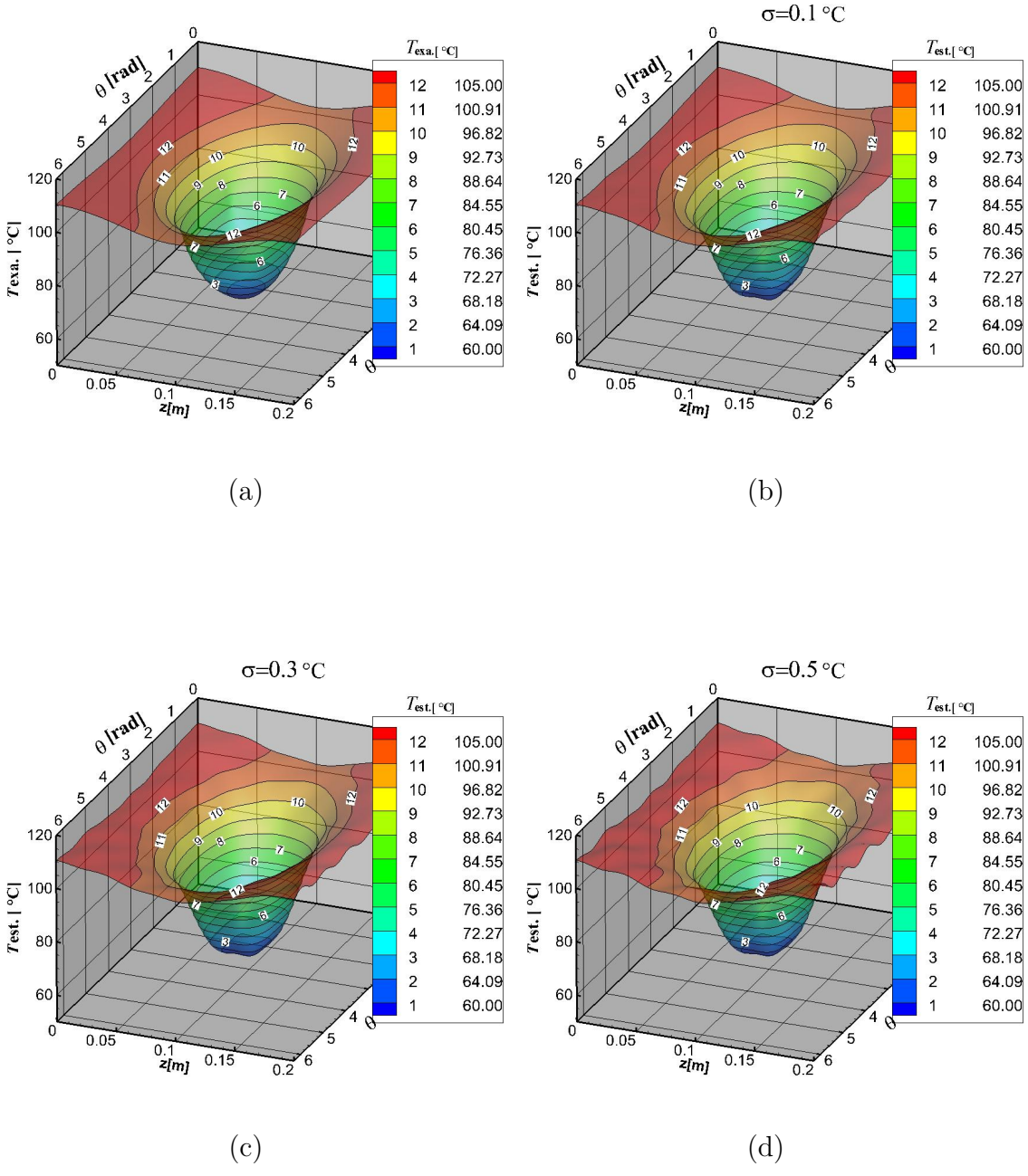

Figure 6.34: (a)Exact temperature on S_0 (h1); (b)Estimated temperature on S_0 with $\sigma = 0.1^o$C (h1); (c)Estimated temperature on S_0 with $\sigma = 0.3^o$C (h1); (d)Estimated temperature on S_0 with $\sigma = 0.5^o$C (h1)

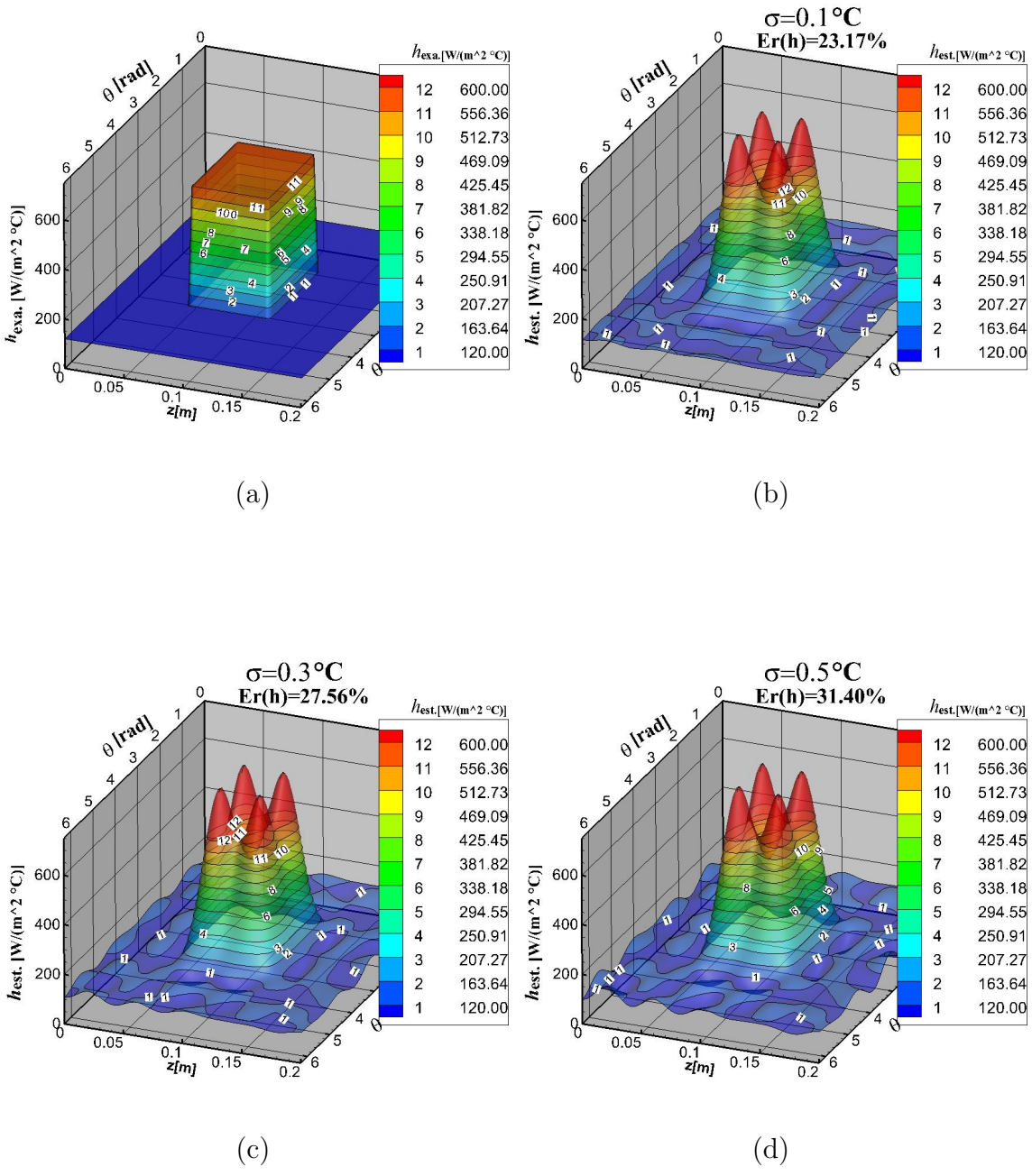

(a) (b)

(c) (d)

Figure 6.35: (a)Exact heat transfer coefficient on S_0 (h1); (b)Estimated heat transfer coefficient on S_0 with $\sigma = 0.1^o$C (h1); (c)Estimated heat transfer coefficient on S_0 with $\sigma = 0.3^o$C (h1); (d)Estimated heat transfer coefficient on S_0 with $\sigma = 0.5^o$C (h1)

Case with Two Discontinuities (h2: $\sigma = 0.1^o$C, $\sigma = 0.3^o$C, $\sigma = 0.5^o$C)

Results concerning the estimate of the heat flux for case h2 are presented in Figs.6.36a-6.36d, where synthetic temperature measurements with noise ($\sigma = 0.1^o$C, $\sigma = 0.3^o$C, $\sigma = 0.5^o$C) were adopted. In this case, the heat transfer coefficient h2 is different from the previous h1 profile by the presence of two abrupt discontinuities, as reported in Tab.6.1. The same noisy temperature data was used to estimate the internal wall temperature, which is shown in Figs.6.37a-6.37d. With the value of heat flux and the wall temperature, the convection heat transfer coefficient on the boundary S_0 was computed and it is shown in Figs.6.38a-6.38d. Similarly to what was observed for the case h1, the estimated heat transfer coefficient as well as the heat flux and the internal wall temperature for noisy temperature measurement with $\sigma = 0.1^o$C agrees well with the exact profile although the accuracy of the estimation decreases when the noise level increases. This fact can be observed on Figs.6.36c, 6.37c and 6.38c, which correspond to $\sigma = 0.3^o$C, and on Figs.6.36d, 6.37d and 6.38d for $\sigma = 0.5^o$C. The estimation error values for h2 as reported in Tab.6.2, confirms again this observation. The overall relative error for the heat transfer coefficient was 27% for $\sigma = 0.1^o$C, 29% for $\sigma = 0.3^o$C and 32% for $\sigma = 0.5^o$C. Nevertheless, the discontinuity is well captured even when the noise level was increased.

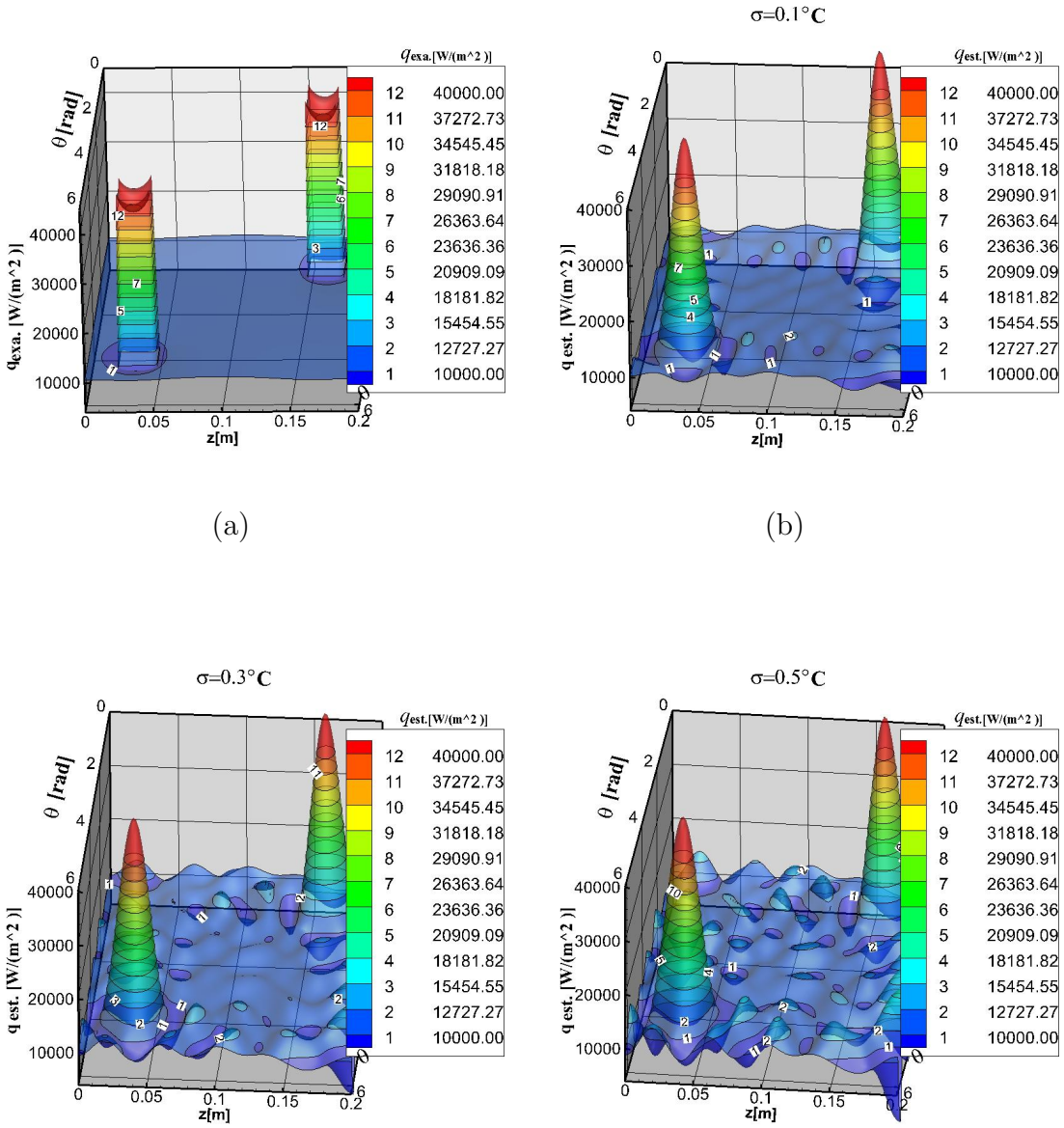

(a) (b)

(c) (d)

Figure 6.36: (a)Exact heat flux on S_0 (h2);(b)Estimated heat flux on S_0 with $\sigma = 0.1^o$C (h2); (c)Estimated heat flux on S_0 with $\sigma = 0.3^o$C (h2); (d)Estimated heat flux on S_0 with $\sigma = 0.5^o$C (h2)

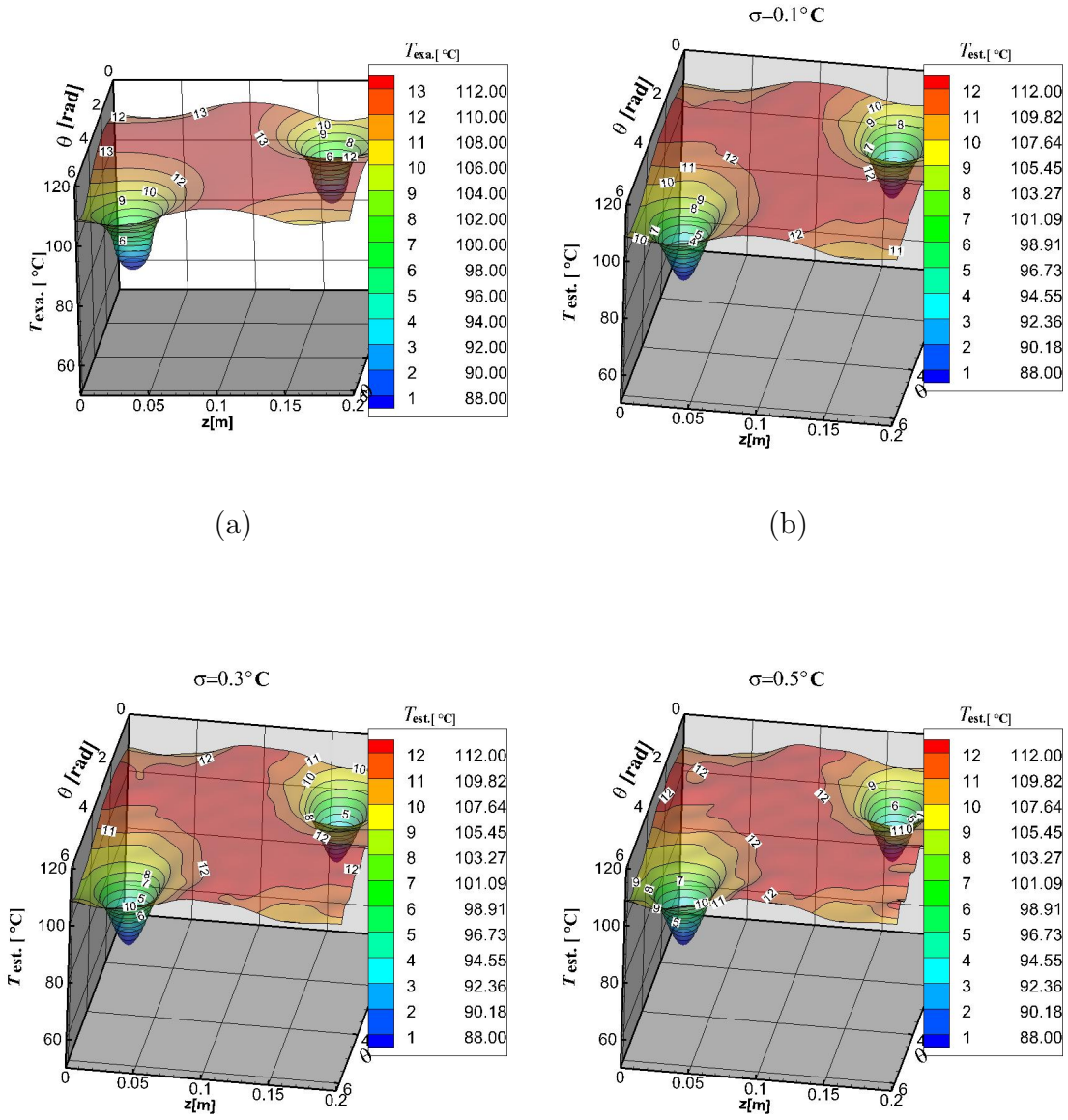

(a) (b)

(c) (d)

Figure 6.37: (a)Exact temperature on S_0 (h2); (b)Estimated temperature on S_0 with $\sigma = 0.1^o$C (h2); (c)Estimated temperature on S_0 with $\sigma = 0.3^o$C (h2); (d)Estimated temperature on S_0 with $\sigma = 0.5^o$C (h2)

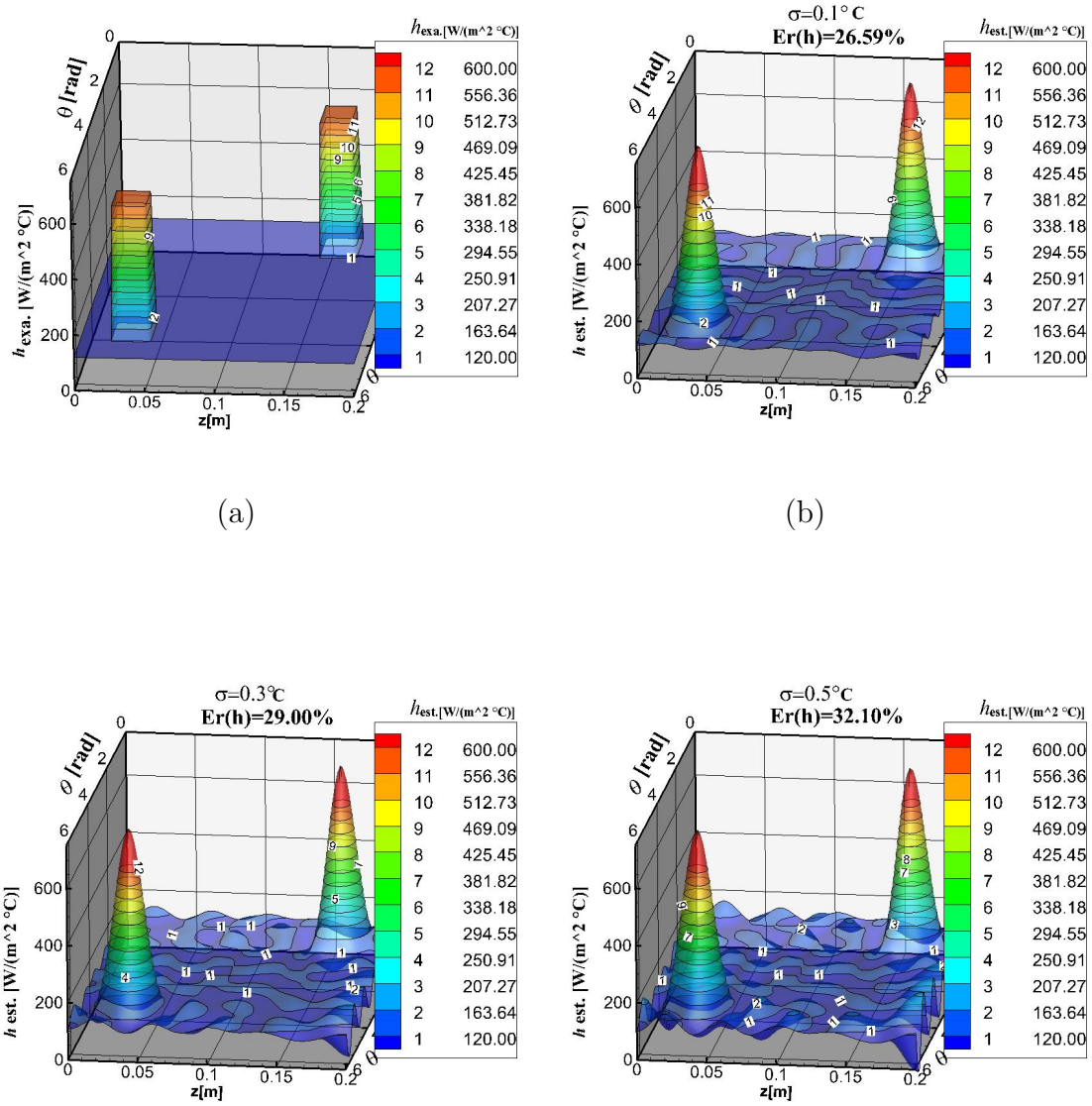

(a) (b)

(c) (d)

Figure 6.38: (a)Exact heat transfer coefficient on S_0 (h2); (b)Estimated heat transfer coefficient on S_0 with $\sigma = 0.1^o$C (h2); (c)Estimated heat transfer coefficient on S_0 with $\sigma = 0.3^o$C (h2); (d)Estimated heat transfer coefficient on S_0 with $\sigma = 0.5^o$C (h2)

Case with Three Discontinuities (h3: $\sigma = 0.1^o$C, $\sigma = 0.3^o$C, $\sigma = 0.5^o$C)

The test case h3, as already mentioned, was chosen to challenge the method regarding its capability of estimating the heat transfer coefficient in a situation with many discontinuities. In this case, the heat transfer coefficient distribution is characterized by three peaks, designed by h3 in Tab.6.1. Noisy temperature measurements were generated with $\sigma = 0.1^o$C. $\sigma = 0.3^o$C and $\sigma = 0.5^o$C.

Results concerning the heat flux are presented in Figs.6.39a-6.39d, while the estimated internal wall temperatures are shown in Figs.6.40a-6.40d. The convection heat transfer coefficient on the boundary S_0 was estimated through Eq.(4.108) and shown in Figs.6.41a-6.41d. Comparing these results with the previous ones, for the h1 profile, a slightly deterioration of the estimates can be observed, where, for exemple, for the heat flux, there are more oscillations. Such qualitative behaviour can be verified from the analysis of Tab.6.2, where the overall relative error increased from 27% to 28% for $\sigma = 0.1^o$C, from 29% to 31% for $\sigma = 0.3^o$C and from 31% to 35% for $\sigma = 0.5^o$C. Nevertheless, the estimates are still good in the sense that they allow identifying the regions with large variations on the heat transfer coefficient.

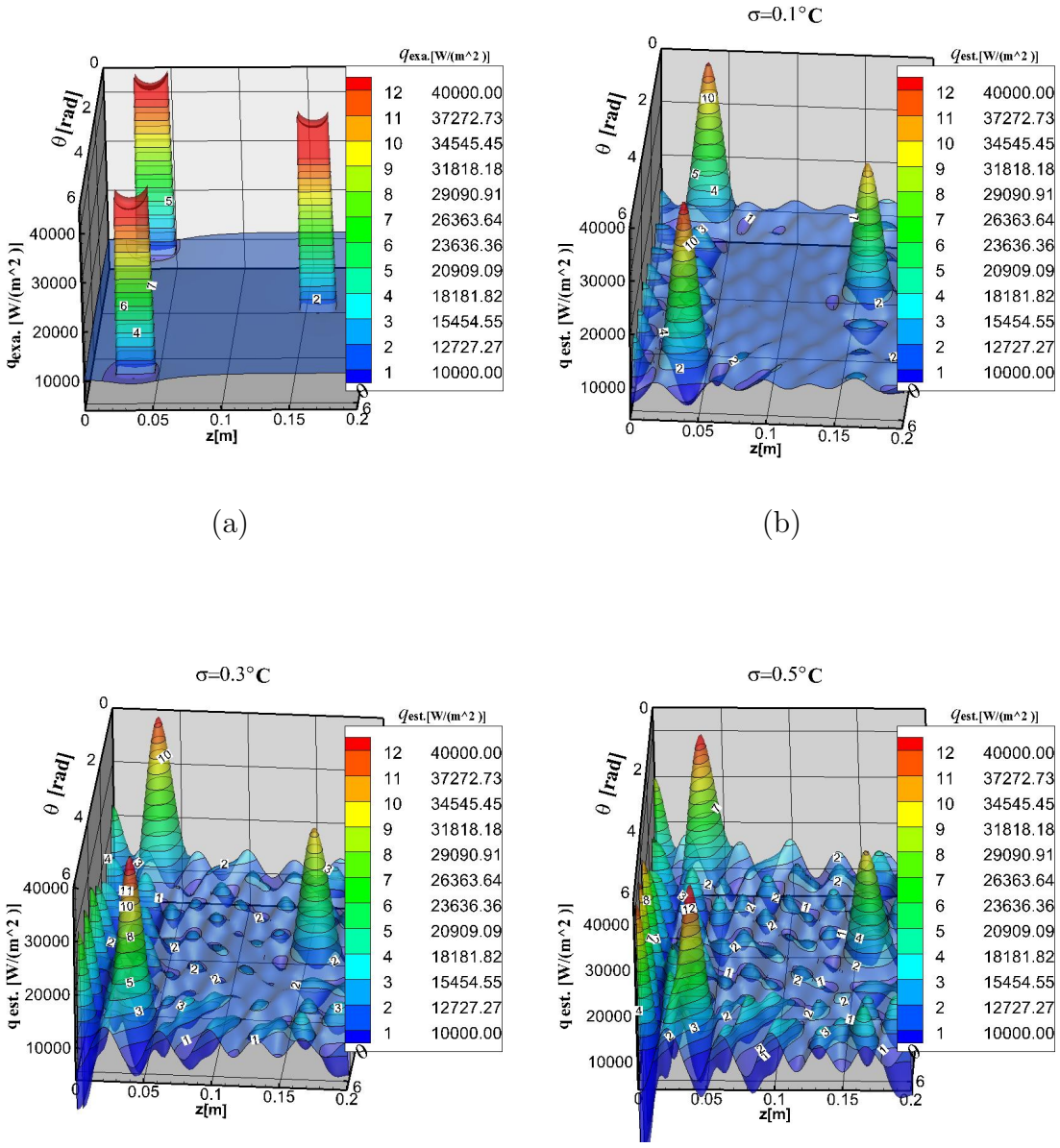

(a) (b)

(c) (d)

Figure 6.39: (a)Exact heat flux on S_0 (h3); (b)Estimated heat flux on S_0 with $\sigma = 0.1^o$C (h3); (c)Estimated heat flux on S_0 with $\sigma = 0.3^o$C (h3); (d)Estimated heat flux on S_0 with $\sigma = 0.5^o$C (h3)

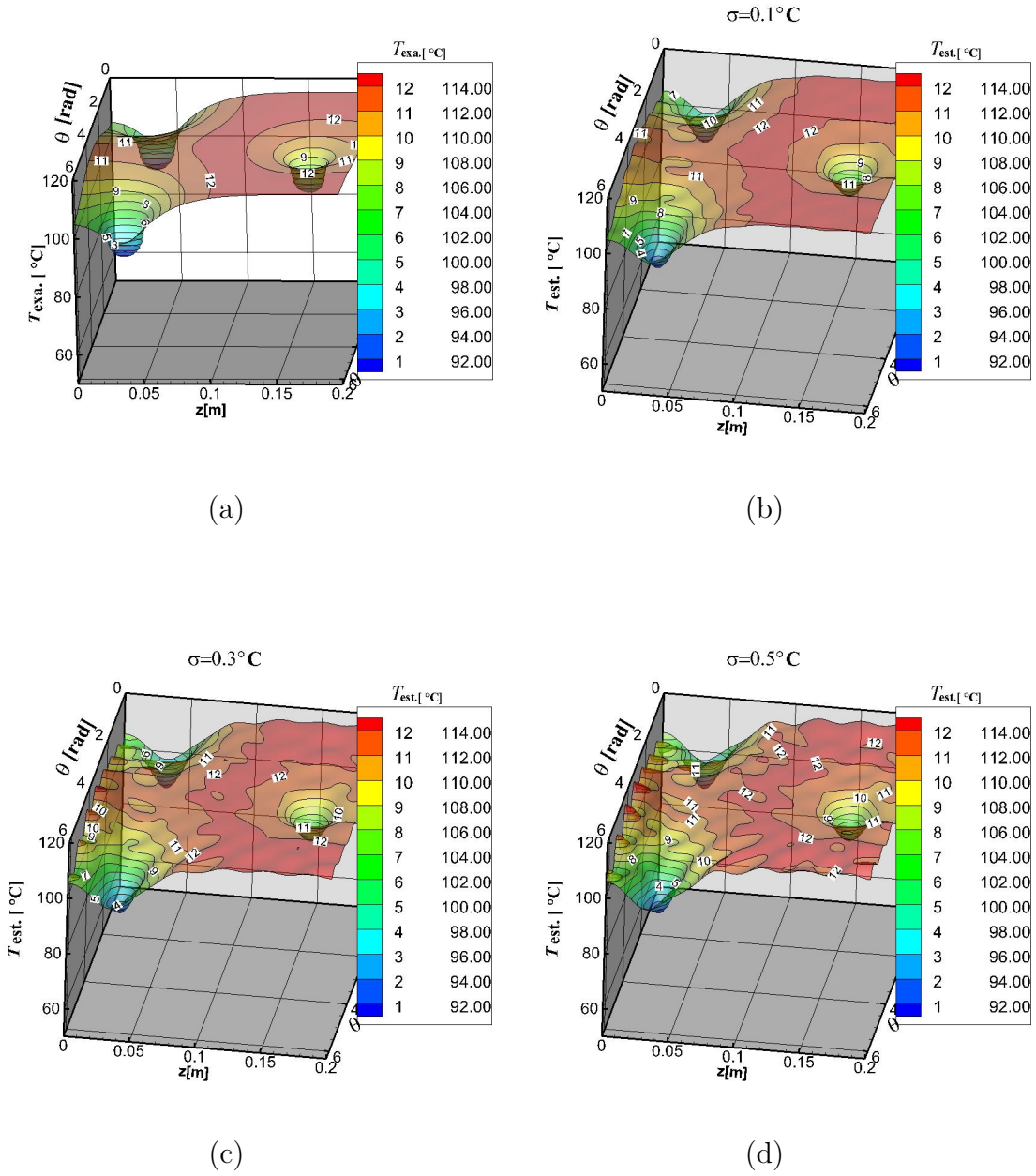

Figure 6.40: (a)Exact temperature on S_0 (h3); (b)Estimated temperature on S_0 with $\sigma = 0.1^o$C (h3); (c)Estimated temperature on S_0 with $\sigma = 0.3^o$C (h3); (d)Estimated temperature on S_0 with $\sigma = 0.5^o$C (h3)

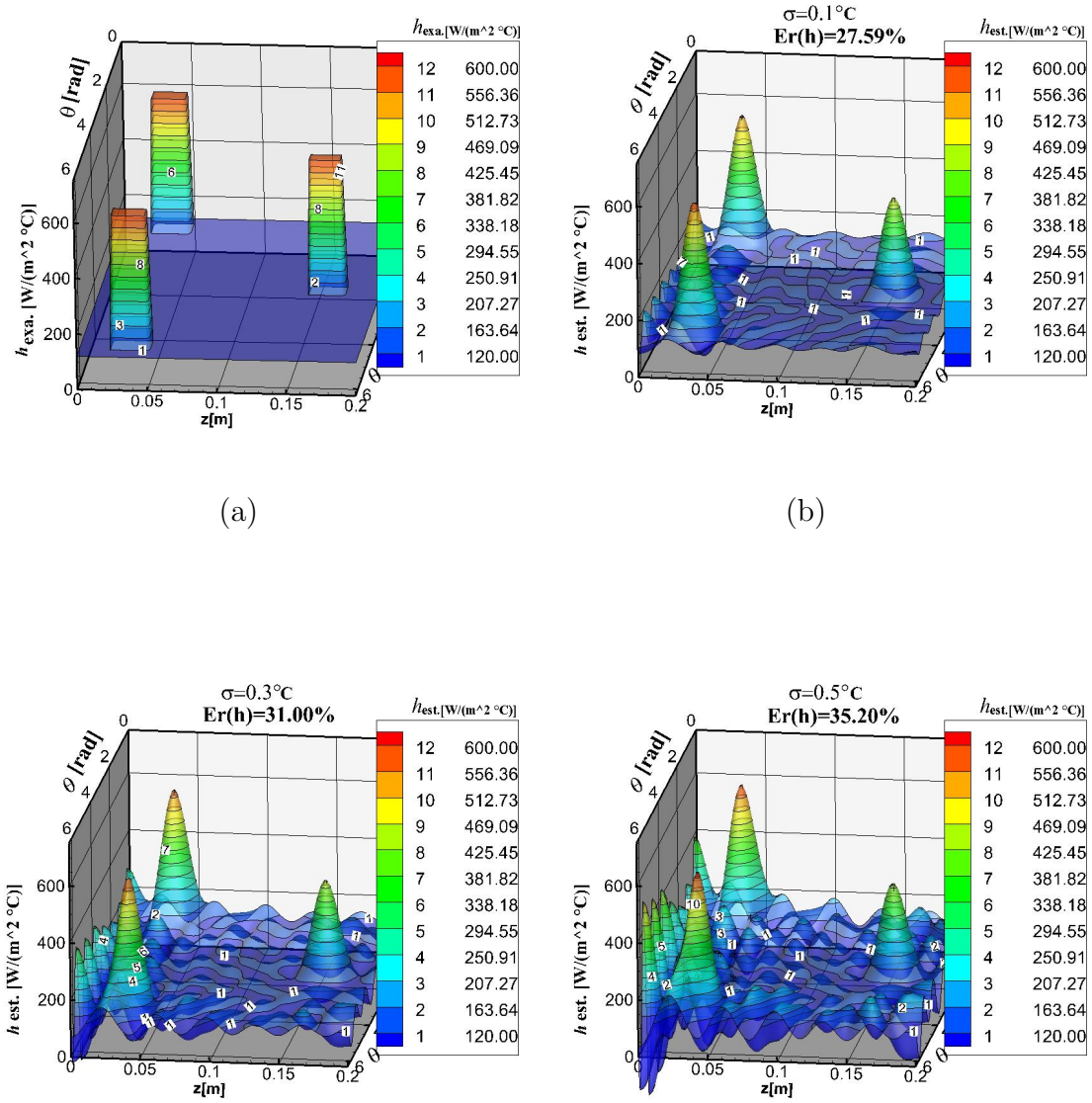

Figure 6.41: (a)Exact heat transfer coefficient on S_0 (h3); (b)Estimated heat transfer coefficient on S_0 with $\sigma = 0.1^o$C (h3); (c)Estimated heat transfer coefficient on S_0 with $\sigma = 0.3^o$C (h3); (d)Estimated heat transfer coefficient on S_0 with $\sigma = 0.5^o$C (h3)

Case with Smooth Low Magnitude Profile (h4: $\sigma = 0.1^o$C, $\sigma = 0.3^o$C, $\sigma = 0.5^o$C)

In this section, the results regarding the test case h4 with smooth distribution and low magnitude of the heat transfer coefficient are presented. This profile was defined in Tab.6.1. Figures6.42,6.43 and 6.44 show the estimated heat flux, internal wall temperature and the convection heat transfer coefficient. It can be observed that the results are better than the previous cases even when measurement data

contained noise up to $\sigma = 0.5^o$C. This observation is also confirmed by Tab.6.2, where one can notice the small values of the overall relative errors, which vary from 4.07%(for $\sigma = 0.1^o$C) to 4.25% (for $\sigma = 0.5^o$C). In fact, these values are much smaller than the ones for test cases h1-h3.

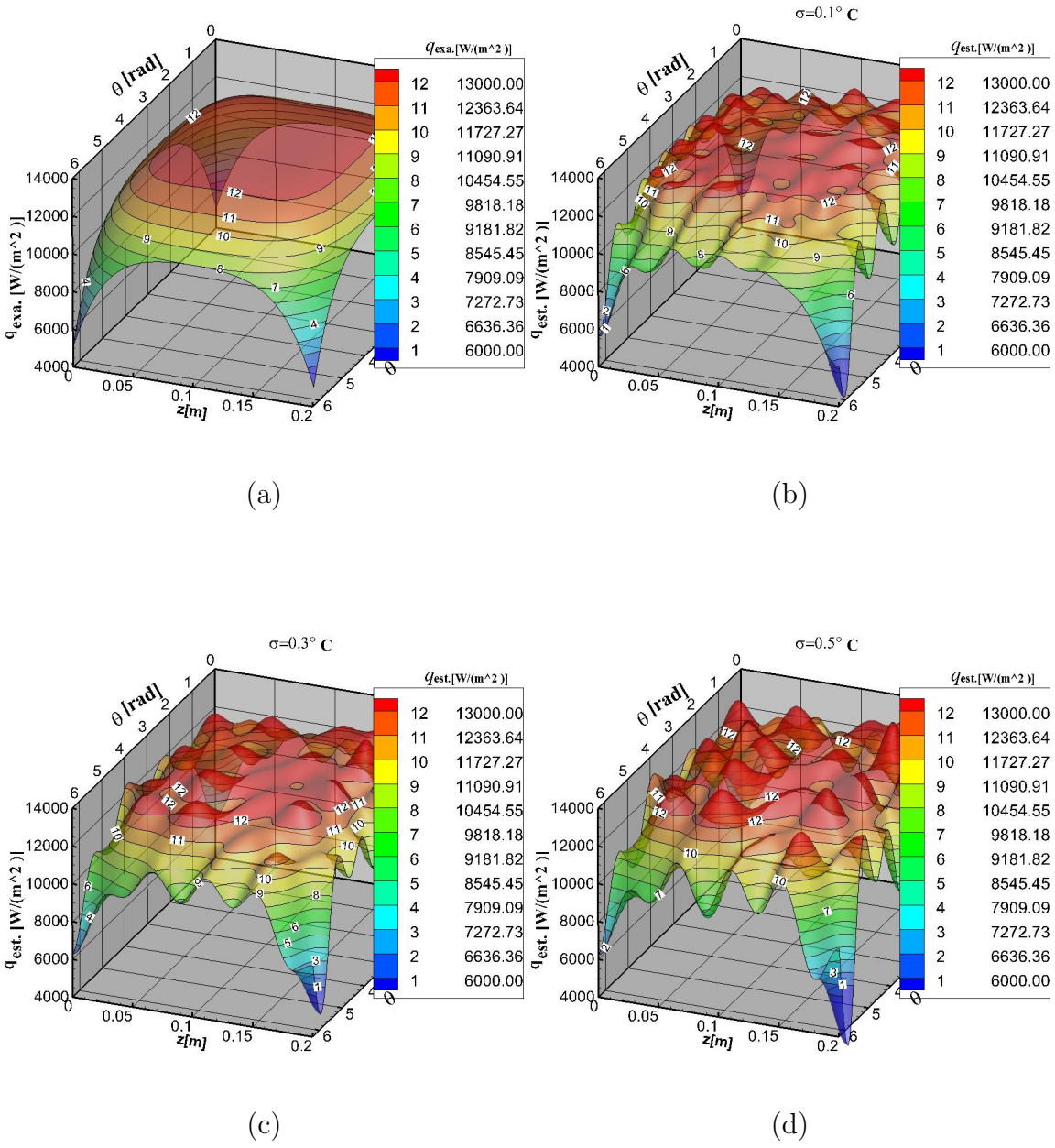

(a) (b)

(c) (d)

Figure 6.42: (a)Exact heat flux on S_0 (h4); c(b)Estimated heat flux on S_0 with $\sigma = 0.1^o$C (h4); (c)Estimated heat flux on S_0 with $\sigma = 0.3^o$C (h4); (d)Estimated heat flux on S_0 with $\sigma = 0.5^o$C (h4)

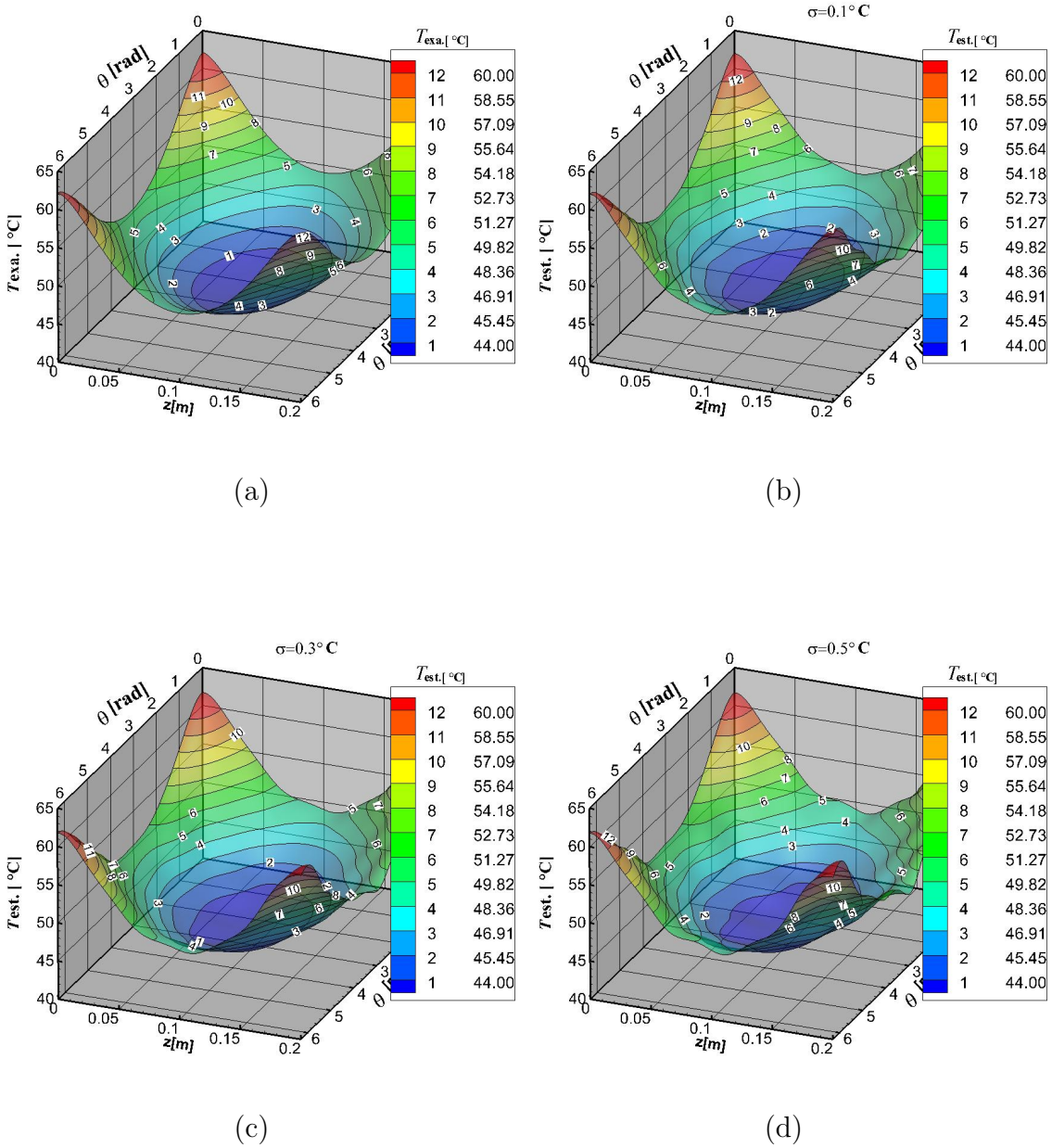

(a) (b)

(c) (d)

Figure 6.43: (a)Exact temperature on S_0 (h4); (b)Estimated temperature on S_0 with $\sigma = 0.1^o$C (h4); (c)Estimated temperature on S_0 with $\sigma = 0.3^o$C (h4); (d)Estimated temperature on S_0 with $\sigma = 0.5^o$C (h4)

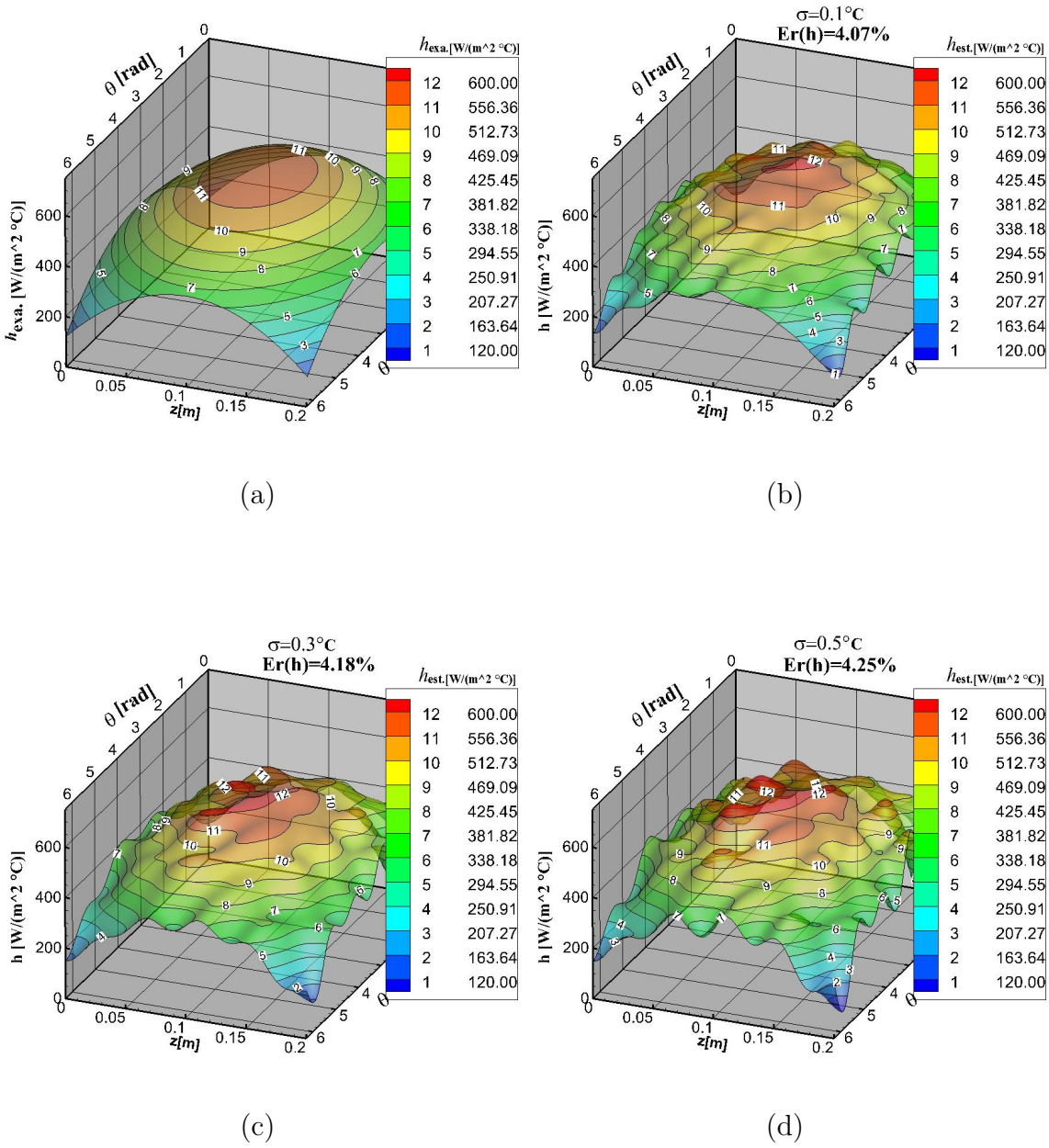

Figure 6.44: (a)Exact heat transfer coefficient on S_0 (h4); (b)Estimated heat transfer coefficient on S_0 with $\sigma = 0.1^o$C (h4); (c)Estimated heat transfer coefficient on S_0 with $\sigma = 0.3^o$C (h4); (d)Estimated heat transfer coefficient on S_0 with $\sigma = 0.5^o$C (h4)

Case with High Magnitude Smooth Profile (h5: $\sigma = 0.1^o$C, $\sigma = 0.3^o$C, $\sigma = 0.5^o$C)

The case h5 has also a smooth heat transfer coefficient distribution like h4, but with a higher magnitude. The maximum amplitude of h5 is 5000 W/(m^2 ^{o}C), while for the test case h4 it is 600 W/(m^2 ^{o}C). This case (h5) was tested to investigate the effectiveness of the method regarding the estimate of smooth functions with high magnitude, especially when noisy input data are used. The analysis of Figs.6.45,

6.46 and 6.47 shows the same observation made regarding the case h4. The results are more accurate than for the cases containing discontinuities. These differences of accuracy were reported in Tab.6.2 through the analysis of residues and estimation error. It can also observed, from Tab.6.2, that an increase in the maximum value of the heat transfer coefficient slightly deteriorates the estimate when compared with the ones for h4. In fact, the overall relative error increased from 3.76%(for $\sigma = 0.1^o$C) to 5.35% (for $\sigma = 0.5^o$C).

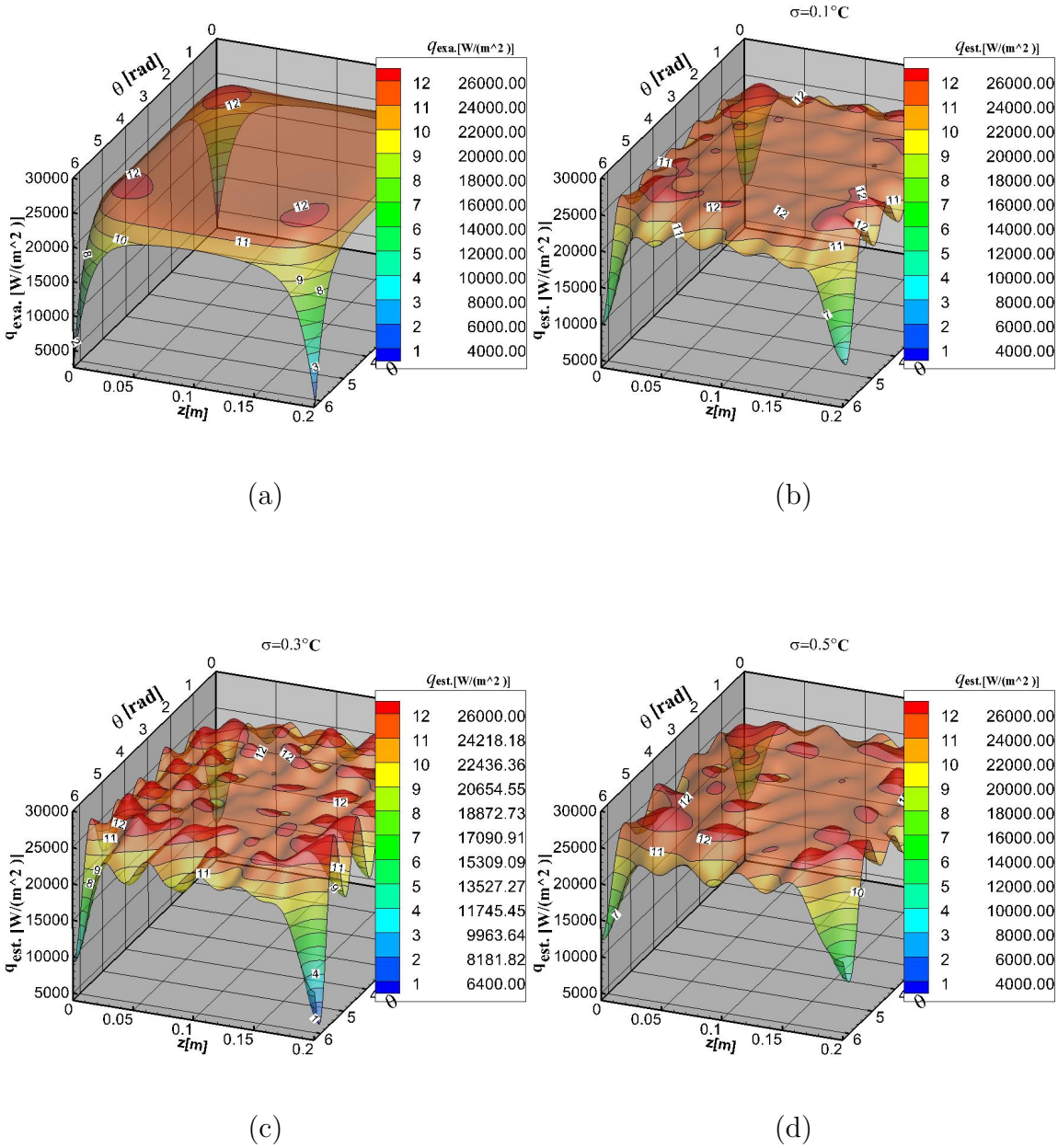

Figure 6.45: (a)Exact heat flux on S_0 (h5); (b)Estimated heat flux on S_0 with $\sigma = 0.1^o$C (h5); (c)Estimated heat flux on S_0 with $\sigma = 0.3^o$C (h5); (d)Estimated heat flux on S_0 with $\sigma = 0.5^o$C (h5)

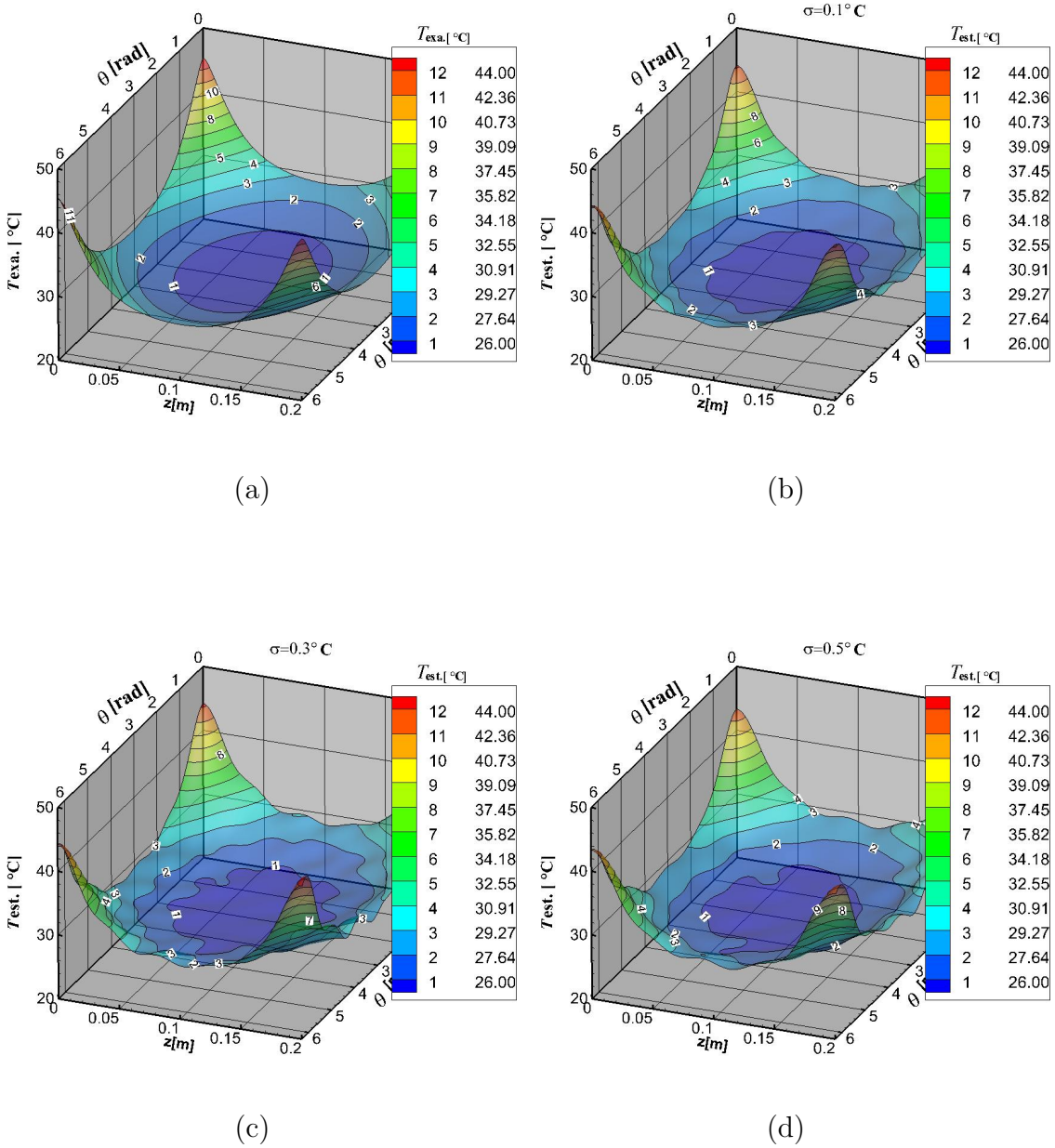

(a) (b)

(c) (d)

Figure 6.46: (a)Exact temperature on S_0 (h5); (b)Estimated temperature on S_0 with $\sigma = 0.1^o$C (h5); (c)Estimated temperature on S_0 with $\sigma = 0.3^o$C (h5); (d)Estimated temperature on S_0 with $\sigma = 0.5^o$C (h5)

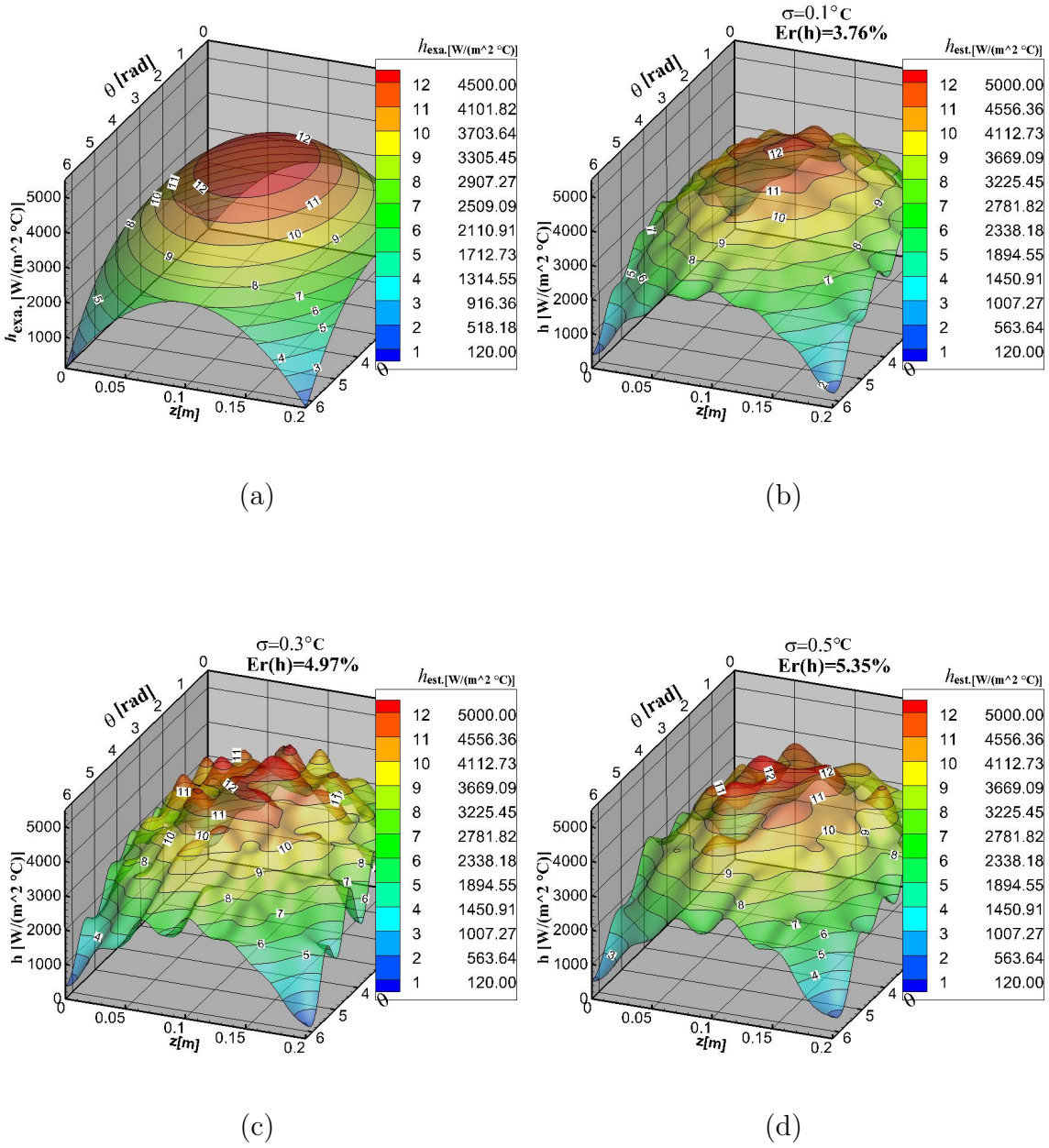

(a) (b)

(c) (d)

Figure 6.47: (a)Exact heat transfer coefficient on S_0 (h5); (b)Estimated heat transfer coefficient on S_0 with $\sigma = 0.1^o$C (h5); (c)Estimated heat transfer coefficient on S_0 with $\sigma = 0.3^o$C (h5); (d)Estimated heat transfer coefficient on S_0 with $\sigma = 0.5^o$C (h5)

6.2 Numerical Verification Using Transient Synthetic Data

In order to verify the accuracy of the time depending Reciprocity Functional Method [10] used in this work, numerical experiments were made regarding the test cases h1 and h3. Since these cases were used to challenge the RFM in steady state regime, they where chosen for transient verification of the method. The same physical problem and parameters were used in the solution of the direct problem, formulated by Eq.(3.2). The environment temperature T_{env} and the working fluid temperature T_b were considered known equal to 20^oC. Measurements with and without noise were used to verify the methodology.

6.2.1 Heat Transfer Estimate without Noise in the Transient Synthetic Data

By using the convection heat transfer coefficients h1 and h3 on the boundary S_0, numerical temperature measurements were generated by solving Eq.(3.2). The temperature maps $T_{ext}(t)$ on the external boundary of the tube were saved for Nt time steps, Nt being the number of measurements. These data were considered as the exact temperature measurements $Y(t)$ in Eq.(4.109) to estimate the spatially distribution of the heat transfer coefficient on S_0. The basic idea here is to estimate the heat transfer coefficient in a time much smaller than the one required to reach the steady-state. Fig.6.48 shows the time evolution of the temperature on the external radius for several different locations, considering the h1 profile. As it can be seen, the steady-state regime is reached for $t > 1800$s. Therefore, the results of this section will perform the estimate for smaller times than this.

Figures6.49a-6.49d show the results regarding the estimate of the heat transfer coefficient for the test case h1. Four different times, corresponding to $t = 120s$, $t = 240s$ $t = 540s$ and $t = 900s$ were considered. It can be observed that the shape of the discontinuity was well recovered, even for the lower time, as reported on Figs.6.49a and 6.49b. For $t = 540s$ (see Fig.6.49c), the heat transfer coefficient was completely recovered, while the solution of Eq.(3.2) was still far from the steady-state regime as it can be observed on Fig.6.48.

Concerning the test case h3, Fig.6.51 shows the time evolution of the temperature at points on the external radius, while Figs.6.52a-6.52d present the results obtained using noiseless temperature measurement. The same time steps were considered as for the case h1, and it can also be observed that the peaks were well recovered, even for lower times as shown on Figs.6.52a and 6.52b. The transient external temperature profile for some meaningful points presented in Fig.6.51 show that the

heat transfer coefficient was estimated without the need to reach steady-state regime.

It can also be observed, both for case h1 and h3, that the overall relative error, as calculated by Eq.(6.2) decreases as we advance in time, as it can be seen on Figs.6.50 and 6.53. Nevertheless, the time need to obtain a good estimate is much smaller than the required to reach the steady-state regime.

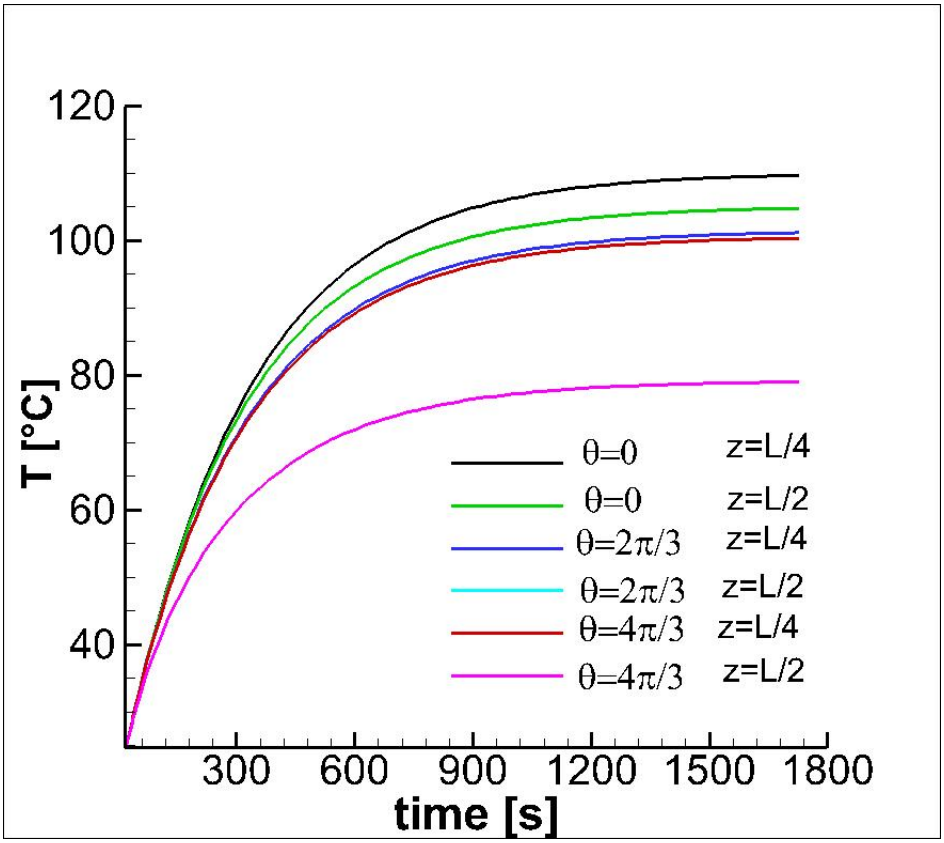

Figure 6.48: Transient temperature profile on the external wall of the duct for some meaningful points (case h1)

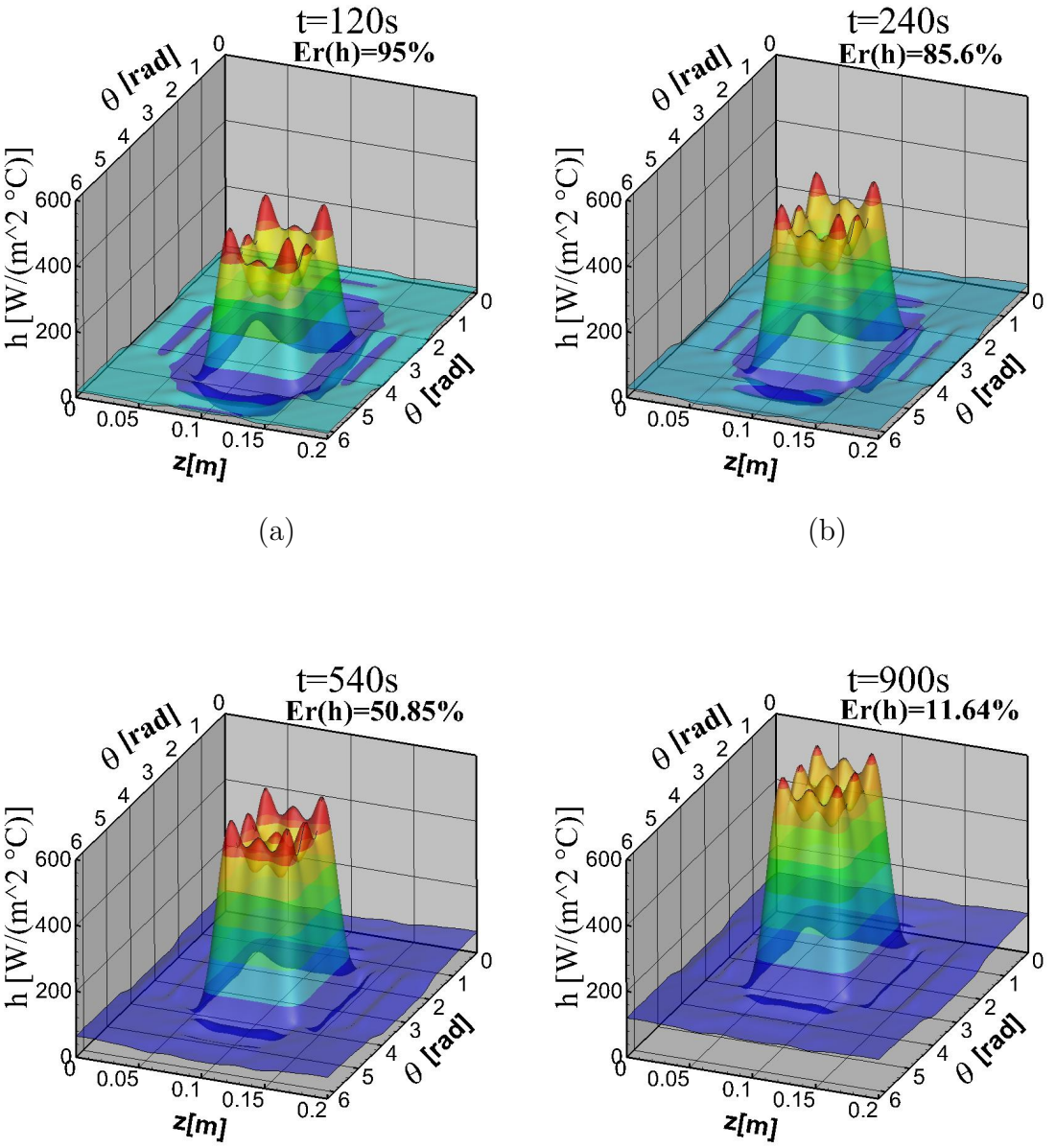

Figure 6.49: (a)Estimated heat transfer coefficient h_0 on S_0 at $t = 120$ s (h1); (b)Estimated heat transfer coefficient h_0 on S_0 at $t = 240$ s (h1); (c)Estimated heat transfer coefficient h_0 on S_0 at $t = 540$ s (h1); (d)Estimated heat transfer coefficient h_0 on S_0 at $t = 900$ s (h1)

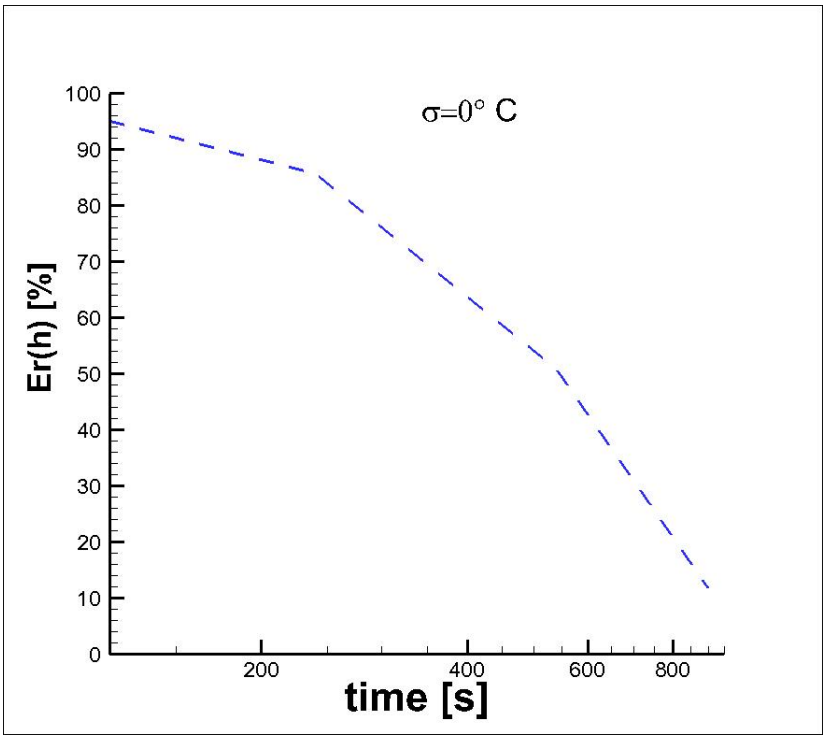

Figure 6.50: Variation of the estimation error $E_r(h)$ with time when using temperature measurements without noise(case h1)

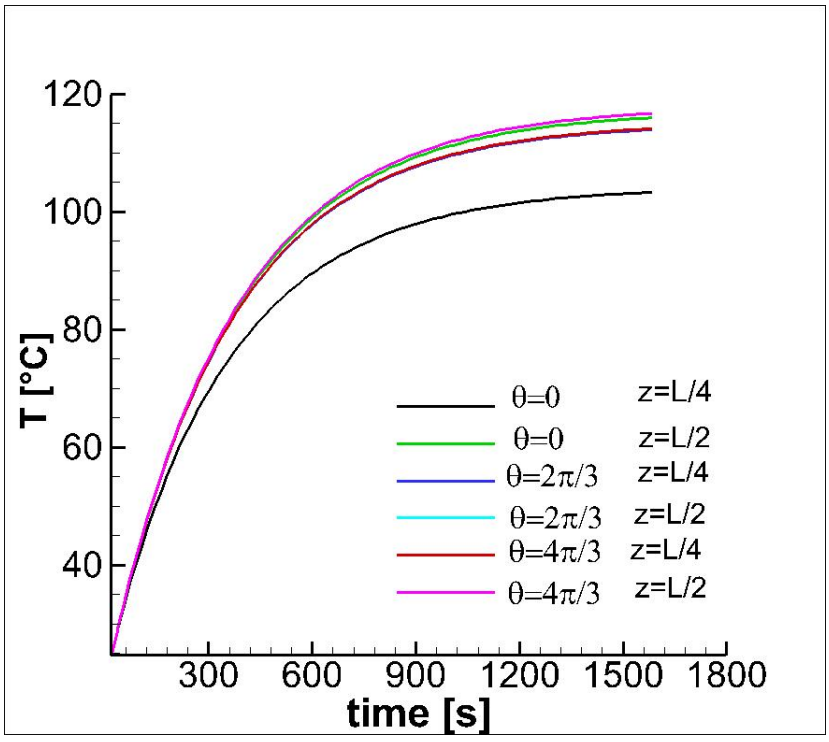

Figure 6.51: Transient temperature profile on the external wall of the duct for some meaningful points (case h3)

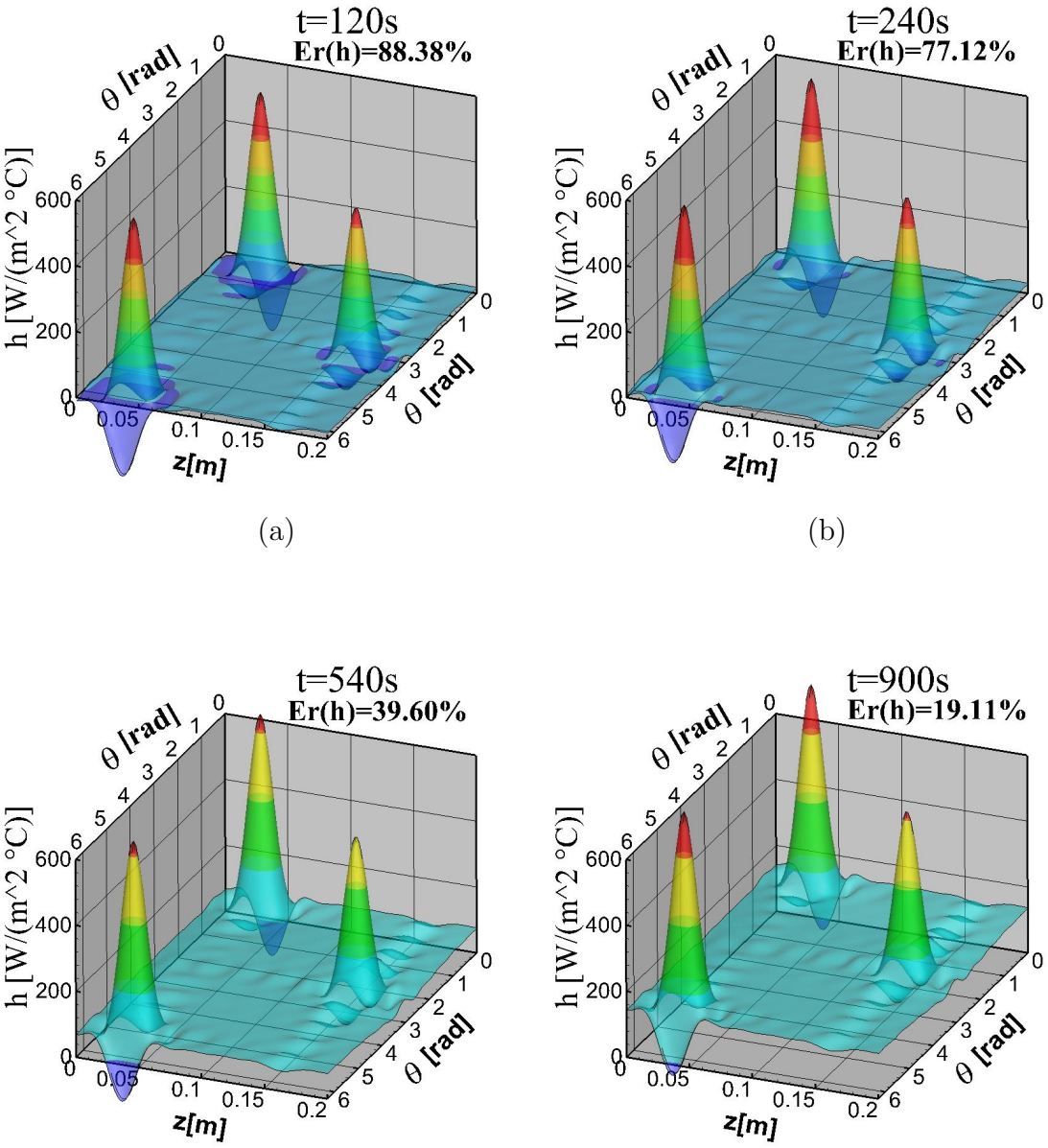

Figure 6.52: (a)Estimated heat transfer coefficient h_0 on S_0 at $t = 120$ s (h3); (b)Estimated heat transfer coefficient h_0 on S_0 at $t = 240$ s (h3); (c)Estimated heat transfer coefficient h_0 on S_0 at $t = 540$ s (h3); (d)Estimated heat transfer coefficient h_0 on S_0 at $t = 900$ s (h3)

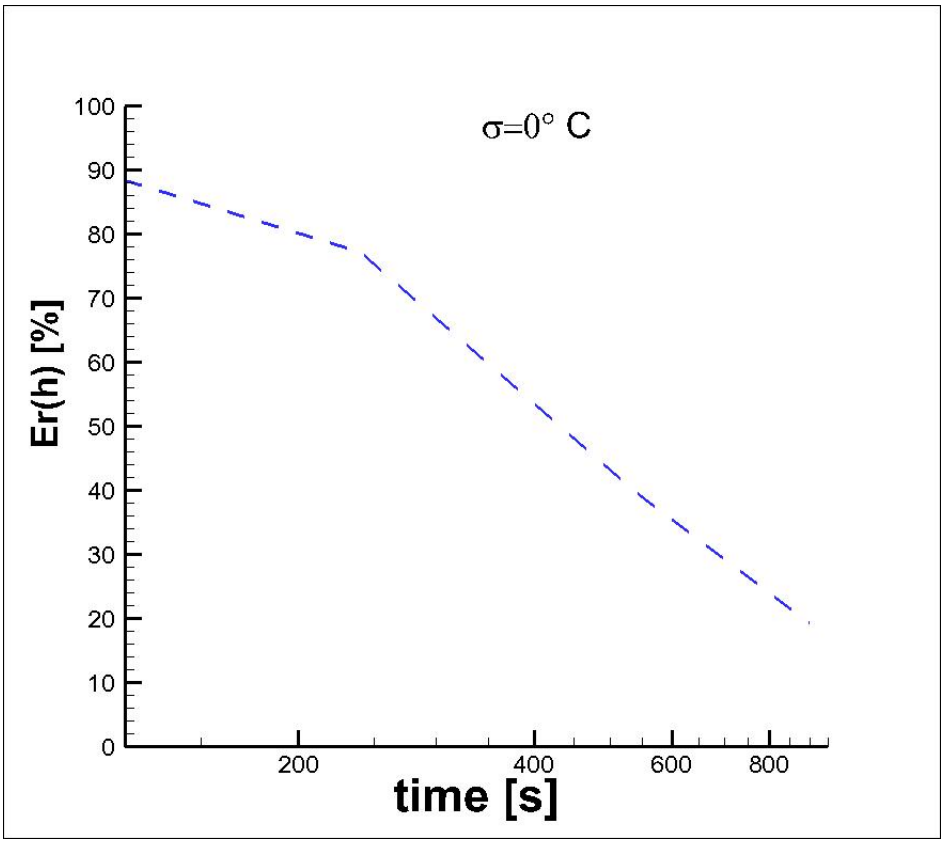

Figure 6.53: Variation of the estimation error $E_r(h)$ with time when using temperature measurements without noise(case h3)

6.2.2 Heat Transfer Estimate with Noise in the Transient Synthetic Data

Numerical transient noisy ($\sigma = 0.1^0C$) temperature measurement were generated following the procedure described by Eqs.(6.4) and (6.5), considering again cases h1 and h3. The noise was added at each time step to generate synthetic measurement data.

By using the convection heat transfer coefficient h1 and h3 on the boundary S_0, numerical temperature measurements were generated by solving Eq.(3.2). The temperature map $T_{ext}(t)$ on the external boundary of the tube was saved for Nt time steps, where Nt is the number of two-dimensional temperature map acquired on the external wall of the duct. Noise was added to these data, according to Eqs.(6.4) and (6.5), and used as measurement $Y(t)$ in Eq.(4.109) to estimate the spatially distribution of the heat transfer on S_0. Figs.6.54 and 6.55 show the time evolution of the noisy ($\sigma = 0.1^0C$) temperature on the external radius for several different locations concerning case h1 and h3.

Figures6.56a-6.56d show the estimate regarding test case h1, while Figs.6.57a-6.57d present the estimate related to the test case h3. It can be observed that the peaks were well recovered, even with the presence of noisy temperature measure-

ment. The overall relative error decreases when advancing in time, both for the case h1 and h3, as it can be seen on Figs.6.58 and 6.59 It is worth noting that good estimates were also obtained without requiring steady-state temperature.

Comparing these transient estimates with the steady-state ones, presented in Fig.6.35b for h1, one can notice that the transient estimates are initially less accurate, but near $t = 900$s they are more accurate than the steady-state ones. Also comparing the overall relative error for the steady-state and the transient measurements, one can confirm this fact.

Regarding the case h3, it is possible to compare the steady-state estimate presented in Fig.6.41b with the transient ones shown on Figs.6.57a-6.57d. From the qualitative analysis of these figures, it is possible to observe that the estimate are almost similar. Also by the qualitative comparison of the overall relative errors of the steady-state estimation, which is 27.59% and the ones for the transient estimate (86.06% for 120s, 75.86% for 240s, 40.51% for 540s and 21.98% for 900s), it is possible to conclude that the convection heat transfer coefficient can accurately be estimated using transient measurements.

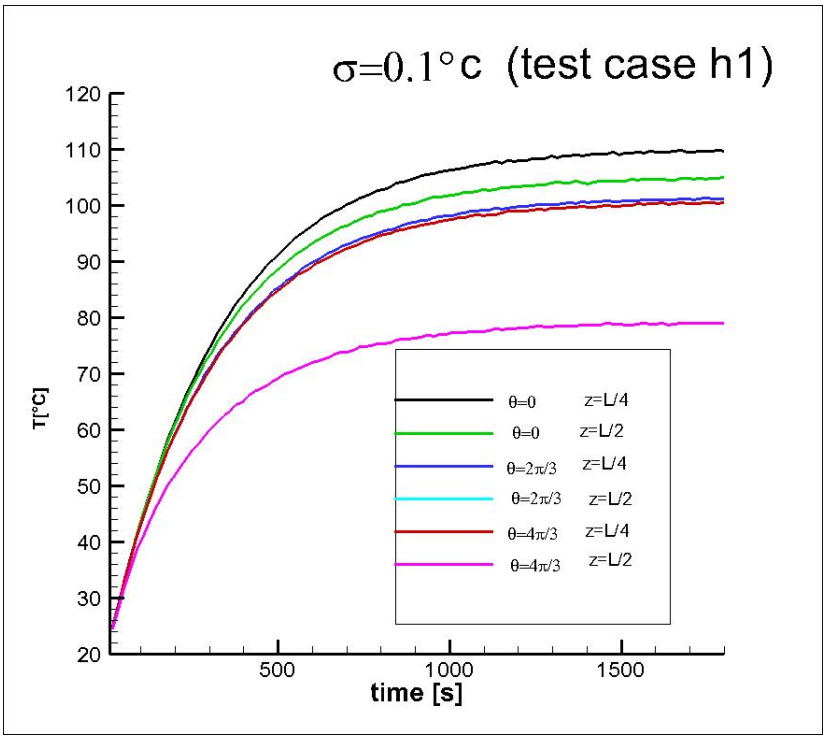

Figure 6.54: Noisy transient temperature profile on the external wall of the duct for some meaningful points with $\sigma = 0.1^0$C (case h1)

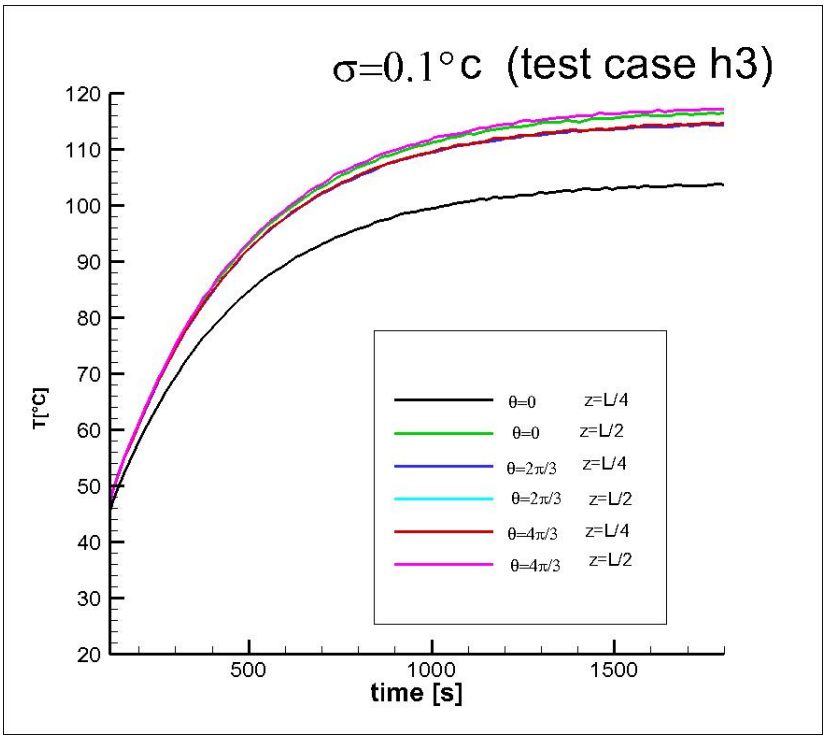

Figure 6.55: Noisy transient temperature profile on the external wall of the duct for some meaningful points with $\sigma = 0.1^0$C (case h3)

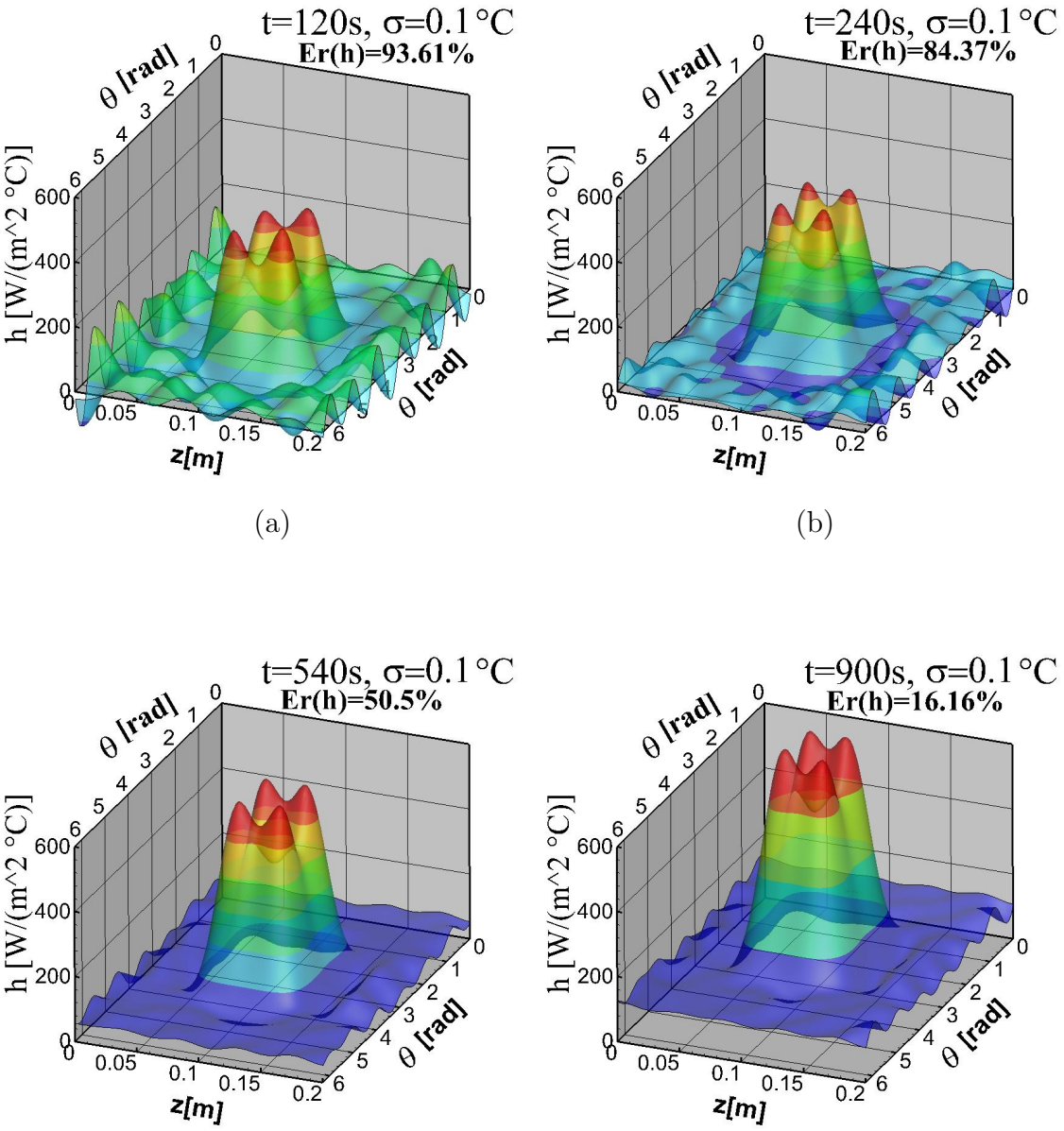

Figure 6.56: (a)Estimated heat transfer coefficient h_0 on S_0 at $t = 120$ s $\sigma = 0.1^0C$ (h1); (b)Estimated heat transfer coefficient h_0 on S_0 at $t = 240$ s $\sigma = 0.1^0C$ (h1); (c)Estimated heat transfer coefficient h_0 on S_0 at $t = 900$ s $\sigma = 0.1^0C$ (h1); (d)Estimated heat transfer coefficient h_0 on S_0 at $t = 900$ s $\sigma = 0.1^0C$ (h1)

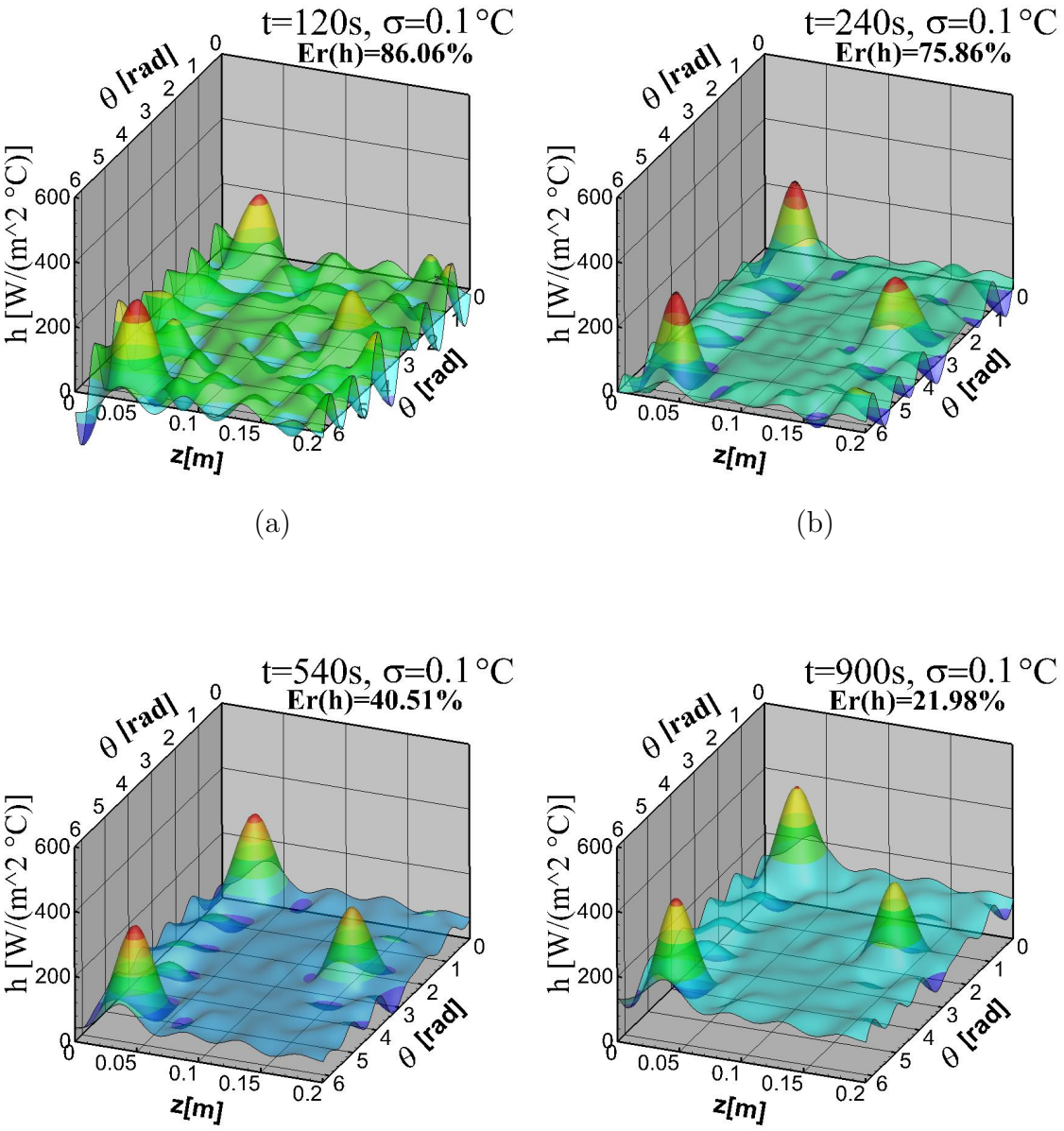

Figure 6.57: (a)Estimated heat transfer coefficient h_0 on S_0 at $t = 120$ s $\sigma = 0.1^0C$(h3); (b)Estimated heat transfer coefficient h_0 on S_0 at $t = 240$ s $\sigma = 0.1^0C$ (h3); (c)Estimated heat transfer coefficient h_0 on S_0 at $t = 540$ s $\sigma = 0.1^0C$ (h3); (d)Estimated heat transfer coefficient h_0 on S_0 at t=900 s $\sigma = 0.1^0C$ (h3)

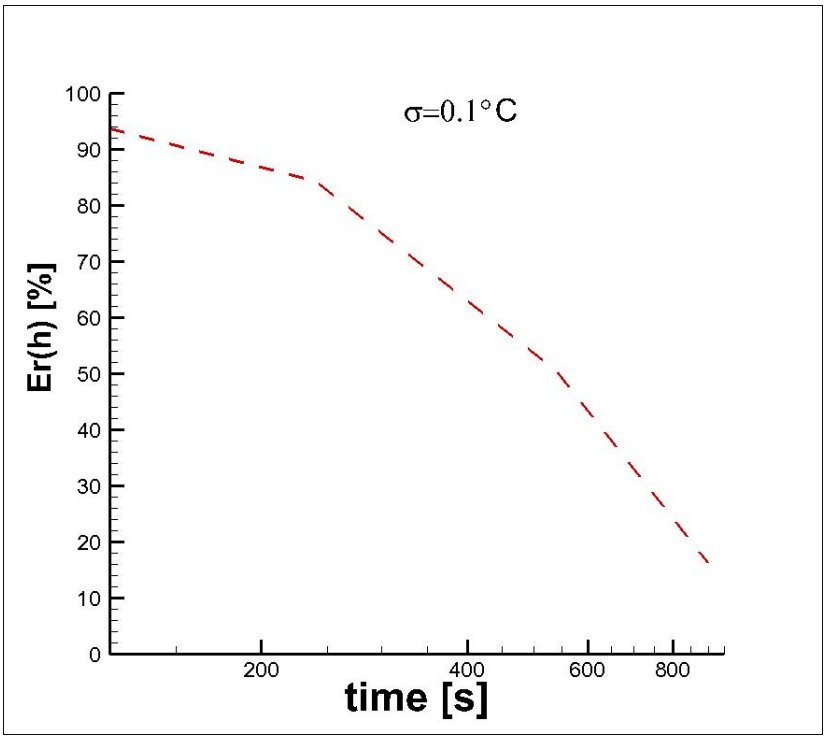

Figure 6.58: Variation of the estimation error $E_r(h)$ with time when using temperature measurements with noise corresponding to $\sigma = 0.1^0$C (case h1)

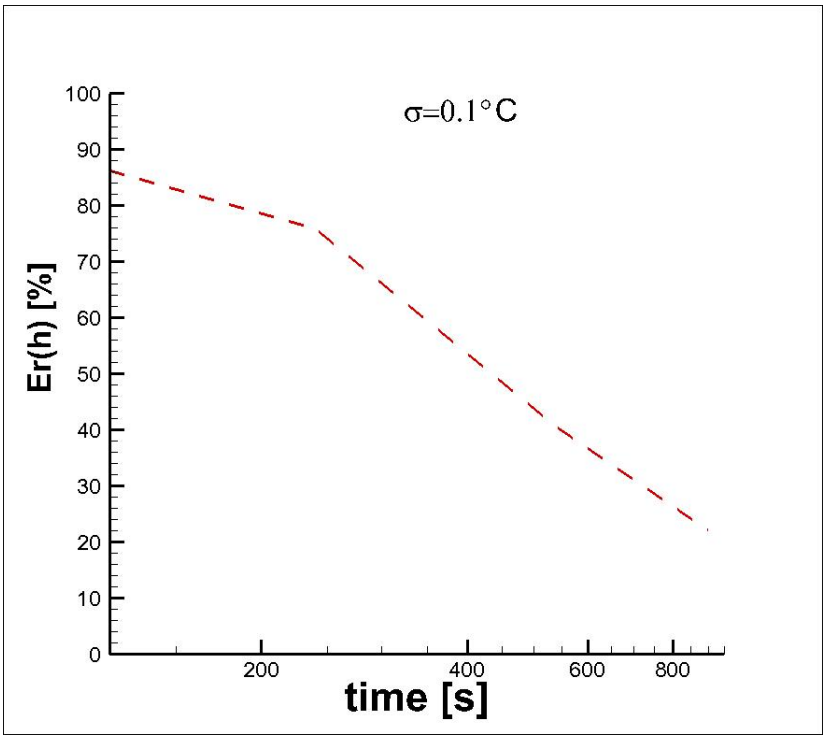

Figure 6.59: Variation of the estimation error $E_r(h)$ with time when using temperature measurements with noise corresponding to $\sigma = 0.1^0$C (case h3)

6.3 Application of the Reciprocity Functional Method to an Experimental Case

The Reciprocity Functional Method hereby developed has been verified numerically, using synthetic temperature measurements on the external wall of the duct in steady-state as well as in transient regime. The methodology was then applied to a real experimental case, as described in Chapter 5. The external temperature was measured with a FLIR SC7000 infrared camera, which has a resolution of 640x512 pixels. The thermal sensitivity of the camera is 20 mK at 303K and its accuracy is ±1K. Tab.6.4 presents the uncertainties associated with the input data. Concerning the estimated convective heat transfer coefficient, the uncertainties have been calculated by parametric bootstrap [65–67], assuming the uncertainties in the input data reported in Tab.6.4. Therefore, the estimated uncertainty for this experimental run is approximately ±10%.

Table 6.4: Uncertainty of the main physical quantities involved in the estimation procedure.

Y[°C]	θ°	K[W/(m°C)]	T_{env}[°C]	h_1[W/(m^2°C)]	g[W/m^3]	T_b[°C]
±0.1°C	±4°	±5%	±0.1°C	±50%	±4%	±0.1°C

The experimental case hereby applied represents an ideal test case for validating the effectiveness of the proposed methodology, since the introduction inside the pipe of the particular inserts represented in Fig.5.3 caused a significant variation of both temperature and heat flux distribution along the angular and axial coordinates as it is possible to notice from Fig.5.8.

The duct considered was modelled as a hollow cylinder and its geometry and physical parameters are presented in Tab.6.5. For the experimental applicability of the Reciprocity Functional Method in this work, a test case corresponding to a turbulent fluid flow Reynolds number of about 8800 was used. The estimated internal heat transfer coefficient obtained by applying the here presented technique in steady state regime and adopting the optimal number of harmonics $N_{\theta,opt}$, is shown in Fig.6.61. It is possible to observe the large variations in the heat transfer coefficient distribution produced by the device inserted into the tube. Particularly, stagnation points could be identified in correspondence to the two extreme parts of the "wings" where the temperature of the fluid reaches the highest values (see Fig.6.60) and the heat transfer coefficient distribution presents its minimum. Also,

around them it can be noticed an increase of heat transfer coefficient due to the fluid acceleration.

Table 6.5: Geometry data and physical parameters for the duct: experimental case.

r_0[m]	r_1[m]	L[m]	K[W/(m°C)]	g[W/m^3]
0.0065	0.0075	0.12	15	7.48x10^6

In addition, it is reported in Figs.6.62a and 6.62b the internal heat transfer coefficient distribution obtained by using a number of harmonics equal to $N_{\theta,opt} - 1$ and $N_{\theta,opt} + 1$, respectively. It can be observed that the results are almost the same, which confirms the robustness of the solution with small variations in the adopted number of harmonics. Figure 6.63 shows that the residuals between the experimental and the estimated temperature values are quite randomly distributed. This is another marker that highlights the effectiveness of the here proposed solution technique according BECK *et al.* [2]. It is also worth noticing that the average standard deviation of the residuals is $\sigma = 0.0498$°C, which is less than the standard deviation of the measurements($\sigma_Y = 0.1$°C, according to Tab.6.4).

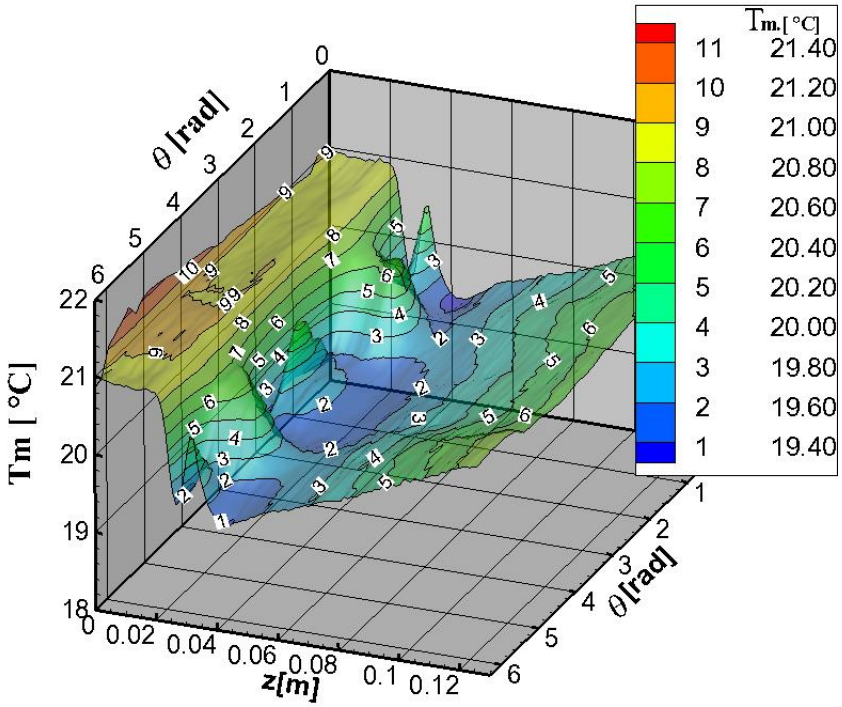

Figure 6.60: Temperature distribution for the experimental case measured with an Infrared Camera(Re=8800) on S_1.

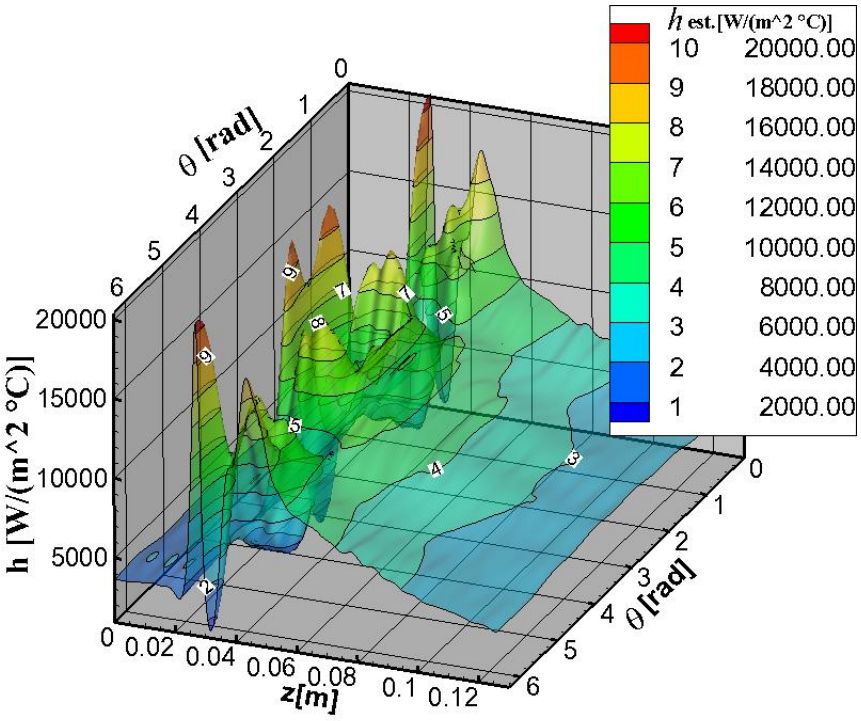

Figure 6.61: Estimated internal heat transfer coefficient for the experimental case using the optimal number of harmonics $N_{\theta,opt}$ (Re=8800, $\sigma = 0.05^{o}C$).

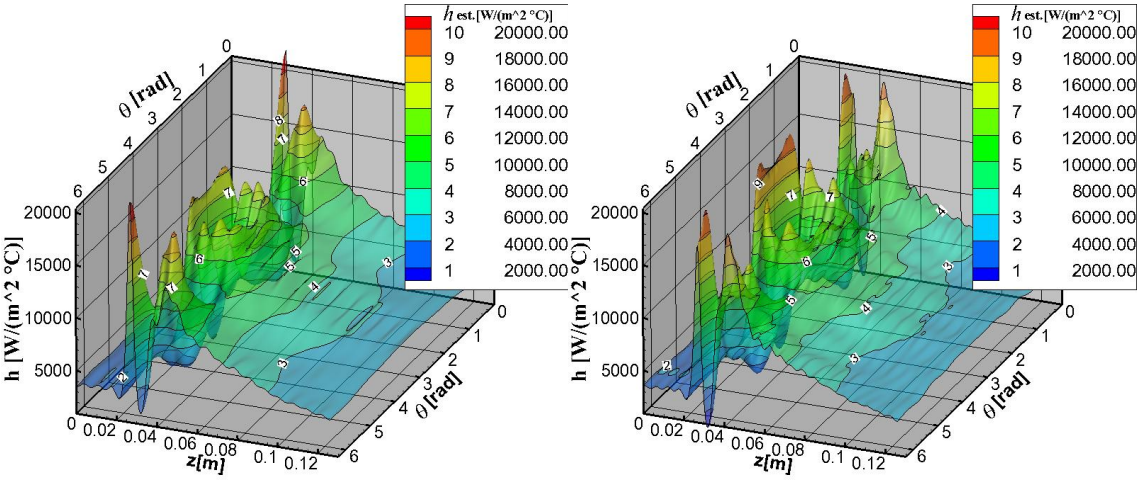

(a) (b)

Figure 6.62: (a)Estimated internal heat transfer coefficient for the experimental case varying the optimal number of harmonics $N_{\theta,opt} - 1$ (Re=8800, $\sigma = 0.05^{o}C$); (b)Estimated internal heat transfer coefficient for the experimental case varying the optimal number of harmonics $N_{\theta,opt} + 1$ (Re=8800, $\sigma = 0.05^{o}C$)

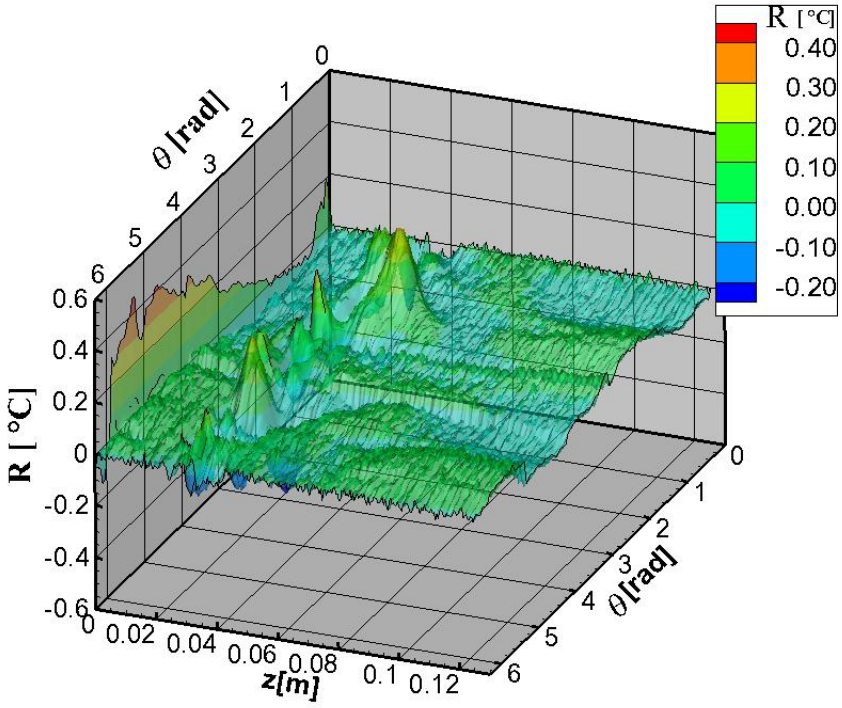

Figure 6.63: Temperature residuals for the experimental case using the optimal number of harmonics $N_{\theta,opt}$ (Re=8800, $\sigma = 0.05^oC$).

The Reciprocity Functional Method has been compared to the Filtering Method (FM) using the real temperature data of the reference [37]. In this reference, the authors estimated the local convection heat transfer coefficient in a duct by adopting the Filtering Method using the real external temperature data acquired with an infrared camera. The case corresponding to a laminar fluid flow Reynolds number of about 275 was analyzed through the RFM and results are compared to the Filtering Method used in the reference [37] as it can be seen in Fig.6.64. Figure 6.64a shows the estimated internal heat transfer coefficient through the Reciprocity Functional Method while Fig.6.64b presents the estimated internal heat transfer coefficient in the reference [37]. The profiles of the estimated heat transfer coefficient are similar and have the same magnitude. This analysis highlights the effectiveness of the here proposed solution technique.

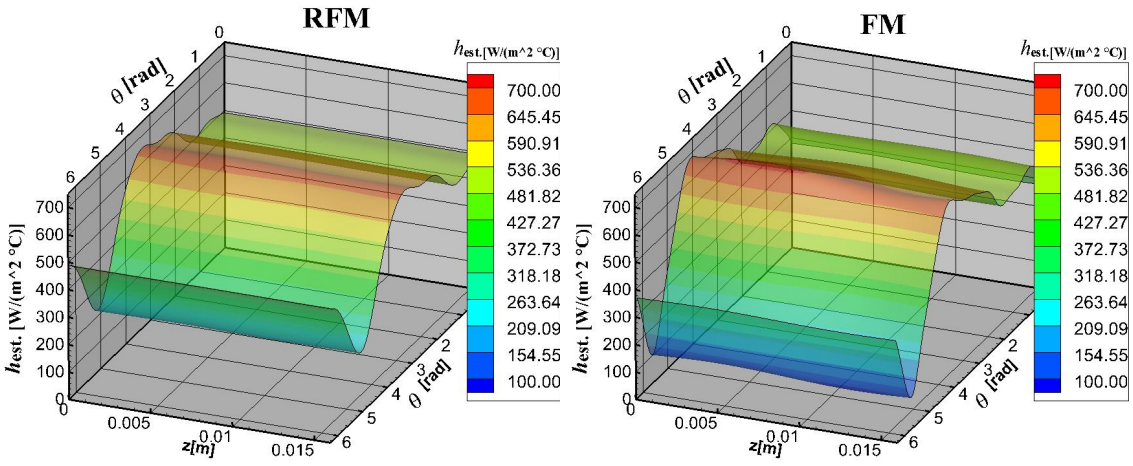

(a) (b)

Figure 6.64: (a)Estimated internal heat transfer coefficient through the Reciprocity Functional Method for the experimental temperature data taken in the literature(Re=275, $\sigma = 0.05^{o}C$); (b)Estimated internal heat transfer coefficient in the literature for the same the experimental temperature data (Re=275, $\sigma = 0.05^{o}C$)

Chapter 7

Conclusion and Future Works

7.1 Conclusion

In this work an original inverse problem approach, based on the reciprocity functional method coupled with the integral transform technique, was presented. The initial associated with this research challenges can be summarized as:

(**i**) Develop a fully analytical three-dimensional inverse problem approach to estimate the internal heat transfer coefficient distribution in ducts;

(**ii**) The methodology must be non-iterative and non-intrusive, in order to be a faster tool for non-destructive tests;

(**iii**) The technique must be able to use both steady and transient temperature measurements on the external wall as input data to estimate the convective heat transfer coefficient distribution on the internal wall;

(**iv**) The method must be numerically verified both in steady and transient regimes;

(**v**) An experiment must be performed in order to highlight the effectiveness of the proposed solution technique.

All these challenges have been solved in this work. A fully analytical estimation approach was successfully applied to a three-dimensional inverse problem: the internal heat transfer coefficient distribution in ducts was estimated by temperature measurements taken on the external boundary of the duct. Such innovative methodology, avoiding the solution of linear systems, resulted in a very fast technique, compared to traditional approaches that are applied to three dimensional problems.

The Reciprocity Functional Method hereby developed has been verified numerically using noiseless measurement as well as noisy temperature measurements ($\sigma = 0.1^oC$, $\sigma = 0.3^oC$, $\sigma = 0.5^oC$). Results showed that the method is able to recover accurately the heat transfer coefficient, even in the presence of noise in the measured temperature. Different internal heat transfer coefficient distributions were accurately recovered. It was found that the results were more accurate when the heat transfer profile to be estimated was smooth than for cases that contained discontinuities.

The number of orthonormal functions, which is an important parameter for the reciprocity functional method, was chosen according to the analysis of the temperature residuals, producing stable and good results. For the experimental case, the choice of this parameter was made analyzing the temperature residuals.

After the numerical verification, the proposed procedure was then tested using real temperature measurements acquired by a FLIR SC 7000 infrared camera, which has the sensitivity about 20 mK at 303K and its accuracy is $\pm$1K. The experiments were realized by the student at the University of Parma in the Department of Industrial and Mechanical Engineering. The results highlighted that the presented methodology was able to recover the unknown function in a very short computational time (around four seconds) and with a good accuracy when the noise level is reasonable.

7.2 Future Works

Along this work, some recommendations to improve the inverse problem methodology developed in this work have appeared. The main recommendations can be summarized as the following:

• Filtering the temperature measurement acquired on the external wall of the ducts in order to eliminate some unwanted frequencies;

• Express the measurement data in terms of Fourier series, which would reduce the integrals appearing in the reciprocity functional terms to constants, reducing even more the computational cost;

• Extend the technique to allow the estimate of the specially bulk temperature if this one is z depending. In the experimental part of this thesis, the bulk temperature has been considered constant.

Bibliography

[1] ALIFANOV, O. *Inverse heat Transfer Problems.* Springer, Berlin, 1994.

[2] BECK, J. V., BALCKWELL, B., CLAIR, C. S. *Inverse Heat Conduction-Ill-posed problems.* John Wiley & Sons Inc, 1985.

[3] TIKHONOV, S. A., ARSENIN, V. *Solution of ill-posed problems.* Winstone & Sons, Washington, 1977.

[4] MURIO, S. D. *The Mollification Method and the Numerical Solution of Ill-posed Prolems.* John Wiley and Sons, New York, 1993.

[5] ABREU, L. A., ORLANDE, H. R. B., KAIPIO, J., *et al.* "Identification of Contact Failures in Multilayered Composites With the Markov Chain Monte Carlo Method", *Journal of Heat Transfer*, v. 136, n. 10, pp. 101302, 2014.

[6] KAIPIO, J., SOMERSALO, E. *Statistical and Computational Inverse Problem.* Springer, 2004.

[7] COLAÇO, M. J., ALVES, C. J. S., BOZZOLI, F. "The reciprocity function approach applied to the non-intrusive estimation of spatially varying internal heat transfer coefficients in ducts: numerical and experimental results", *International Journal of Heat and Mass Transfer*, v. 90, pp. 1221–1231, 2015.

[8] TOUGRI, I., COLAÇO, M. J., BOZZOLI, F., *et al.* "Internal heat transfer coefficient estimation in three-dimensional ducts through the reciprocity functional approach - An analytical approach and validation with experimental data", *International Journal of Heat and Mass Transfer*, v. 122, pp. 587–601, 2018.

[9] TOUGRI, I., COLAÇO, M. J. "Estimation of internal heat transfer coefficients in three-dimensional ducts through the reciprocity functional approach: preliminary results". In: *24th ABCM International Congress of Mechanical Engineering, December 3-8, 2017 Curitiba, PR, Brazil.*

[10] TOUGRI, I., COLAÇO, M. J., BOZZOLI, F. "Time depending reciprocity functional method formulation for estimating internal heat transfer coefficient in ducts". In: *The 9th International Conference "Inverse Problems: Modeling and Simulation" (IPMS-2018), Malta, May 21 - 25, 2018*, .

[11] TOUGRI, I., PADILHA, R. S., COLAÇO, M. J. "An analytical extension of the reciprocity functional approach to estimate thermal contact conductances between different materials using transient measurements". In: *Proceeding of the 16th International Heat Transfer Conference, IHTC-16, August 10-15, 2018 Beijing, China*, .

[12] OZISIK, M. N., ORLANDE, H. R. B. *Inverse Heat transfer: Fundamentals and Applications*. Taylor & francis, New York, NY, 2000.

[13] HADAMARD, J. *Lectures on Cauchy's problem in linear partial differential equations*. Yale University Press, 1923.

[14] ANDRIEUX, S., BEN ABDA, A. "The reciprocity gap: A general concept for flaws identification problems", *Mechanics Research Communication*, v. 20 (5), pp. 415–420, 1993.

[15] REDDY, J. *Energy Principles and Variational Methods in Applied Mechanics*. John Wiley & Sons, Inc, 2002.

[16] ANDRIEUX, S., ABDA, A. B. "Identification of planar cracks by complete overdetermined", *Inverse problems*, v. 12, pp. 553–563, 1996.

[17] BANNOUR, T., ABDA, A. B., JAOUA, M. "A Semi-Explicit Algorithm for the Reconstruction of 3D", *Research Report : inria-00073629*, 1996.

[18] ABDA, A. B., DELBARRY, F., HADDAR, H. "On the use of the Reciprocity-Gap functional in inverse", *Research Report : inria-00070710*, 2004.

[19] COLTON, D., HADDAR, H. "An application of the reciprocity gap functional to inverse scattering theory", *Inverse problems*, v. 21, n. 1, pp. 383–398, 2005.

[20] DELBARY, F., ARAMINI, R., BOZZA, G., *et al.* "On the use of the Reciprocity Gap Functional in inverse scattering with near-field data: An application to mammography", *Journal of Physics: Conference Series*, v. 135, pp. 012032, 2008.

[21] ALVES, C. J. S., ABDALLAH, J. B., JAOUA, M. "Recovery of cracks using a point-source reciprocity gap function", *Inverse Problems in Science and Engineering*, v. 12, n. 5, pp. 519–534, 2004.

[22] SHIFRIN, E. I., SHUSHPANNIKOV, P. S. "Application of Reciprocity Gap Functional for Elastostatic Inverse Problem of Small Well-separated Defects Identification", *Procedia Materials Science*, v. 3, pp. 1105–1110, 2014.

[23] ROBERTY, N. C., ALVES, C. J. S. "On the identification of star-shape sources from boundary measurements using a reciprocity functional", *Inverse Problems in Science and Engineering*, v. 17, n. 2, pp. 187–202, 2009.

[24] COLAÇO, M. J., ALVES, C. J. S. "A fast non-intrusive method for estimating spatial thermal contact conductance by means of the reciprocity functional approach and the method of fundamental solutions", *International Journal of Heat and Mass Transfer*, v. 60, pp. 653–663, 2013.

[25] ABREU, L. A., ALVES, C. J., COLAÇO, M. J., *et al.* "A non-intrusive inverse problem technique for the identification of contact failures in double-layred composites". In: *Proceedings of the 15th International Heat Transfer Conference, IHTC-15 August 10-15 Kyoto, Japan, 2014*.

[26] PADILHA, R. S., COLAÇO, M. J., ORLANDE, H. R. B., *et al.* "An analytical method to estimate spatially-varying thermal contact conductances using the reciprocity functional and the integral transform methods: Theory and experimental validation", *International Journal of Heat and Mass Transfer*, v. 100, pp. 599–607, 2016.

[27] COLAÇO, M. J., ALVES, C. J. S., ORLANDE, H. R. B. "Transient non-intrusive method for estimating spatial thermal contact conductance by means of the reciprocity functional approach and the method of fundamental solutions", *Inverse Problems in Science and Engineering*, v. 23, n. 4, pp. 688–717, 2014.

[28] COLAÇO, M. J., ALVES, C. J. S. "A Backward Reciprocity Function Approach to the Estimation of Spatial and Transient Thermal Contact Conductance in Double-Layered Materials Using Non-Intrusive Measurements", *Numerical Heat Transfer, Part A: Applications*, v. 68, n. 2, pp. 117–132, 2015.

[29] MOCERINO, A., COLAÇO, M. J., BOZZOLI, F., *et al.* "Filtered reciprocity functional approach to estimate internal heat transfer coefficients in 2D cylindrical domains using infrared thermography", *International Journal of Heat and Mass Transfer*, v. 125, pp. 1181–1195, 2018.

[30] KAKAÇ, S., BERGLES, A. E., MAYINGER, F., *et al. Heat Transfer Enhancement of Heat Exchangers*, v. 355. Kluwer, 1999.

[31] KAKAÇ, S., YENER, Y., PRAMUANJAROENKIJ, A. *Convective Heat Transfer*. CRC Press, 2013.

[32] RAINIERI, S., BOZZOLI, F., PAGLIARINI, G. "Experimental investigation on the convective heat transfer in straight and coiled corrugated tubes for highly viscous fluids: Preliminary results", *International Journal of Heat and Mass Transfer*, v. 55, n. 1-3, pp. 498–504, 2012.

[33] RAINIERI, S., BOZZOLI, F., CATTANI, L., *et al.* "Compound convective heat transfer enhancement in helically coiled wall corrugated tubes", *International Journal of Heat and Mass Transfer*, v. 59, pp. 353–362, 2013.

[34] HUANG, C.-H., CHEN, W.-C. "A three-dimensional inverse forced convection problem in estimating surface heat flux by conjugate gradient method", *International Journal of Heat and Mass Transfer*, v. 43, 2000.

[35] BOZZOLI, F., CATTANI, L., RAINIERI, S., *et al.* "Estimation of the local heat-transfer coefficient in the laminar flow regime in coiled tubes by the Tikhonov regularisation method", *International Journal of Heat and Mass Transfer*, v. 72, pp. 352–361, 2014.

[36] BAZÁN, F. V. S., FRANCISCO, J. B. "An improved fixed-point algorithm for determining a Tikhonov regularization parameter", *Inverse problems*, v. 25, n. 4, pp. 045007, 2009.

[37] BOZZOLI, F., CATTANI, L., RAINIERI, S. "Effect of wall corrugation on local convective heat transfer in coiled tubes", *International Journal of Heat and Mass Transfer*, v. 101, pp. 76–90, 2016.

[38] YANG, Y.-C., CHEN, W.-L., CHOU, H.-M., *et al.* "Inverse hyperbolic thermoelastic analysis of a functionally graded hollow circular cylinder in estimating surface heat flux and thermal stresses", *International Journal of Heat and Mass Transfer*, v. 60, pp. 125–133, 2013.

[39] CEBULA, A., TALER, J. "Determination of transient temperature and heat flux on the surface of a reactor control rod based on temperature measurements at the interior points", *Applied Thermal Engineering*, v. 63, n. 1, pp. 158–169, 2014.

[40] LU, T., HAN, W. W., JIANG, P. X., *et al.* "A two-dimensional inverse heat conduction problem for simultaneous estimation of heat convection coefficient, fluid temperature and wall temperature on the inner wall of a pipeline", *Progress in Nuclear Energy*, v. 81, pp. 161–168, 2015.

[41] MIN, C., LI, X., YUAN, Y., *et al.* "An inverse study to optimize the rib pitch in a two-dimensional channel flow problem for heat transfer enhancement", *International Journal of Heat and Mass Transfer*, v. 112, pp. 1044–1051, 2017.

[42] DHIMAN, S. K., PRASAD, J. K. "Inverse estimation of heat flux from a hollow cylinder in cross-flow of air", *Applied Thermal Engineering*, v. 113, pp. 952–961, 2017.

[43] NOH, J.-H., CHA, K.-U., YOOK, S.-J. "Three-dimensional inverse heat conduction modeling of a multi-layered hollow cylindrical tube using input estimation algorithm and thermal resistance network", *International Journal of Heat and Mass Transfer*, v. 106, pp. 793–803, 2017.

[44] NOH, J.-H., CHA, K.-U., AHN, S.-T., *et al.* "Prediction of time-varying heat flux along a hollow cylindrical tube wall using recursive input estimation algorithm and thermal resistance network method", *International Journal of Heat and Mass Transfer*, v. 97, pp. 232–241, 2016.

[45] VOLLE, F., MAILLET, D., GRADECK, M., *et al.* "Practical application of inverse heat conduction for wall condition estimation on a rotating cylinder", *International Journal of Heat and Mass Transfer*, v. 52, n. 1-2, pp. 210–221, 2009.

[46] LU, T., LIU, B., JIANG, P. X., *et al.* "A two-dimensional inverse heat conduction problem in estimating the fluid temperature in a pipeline", *Applied Thermal Engineering*, v. 30, n. 13, pp. 1574–1579, 2010.

[47] INGLESE, G., OLMI, R. "Nondestructive evaluation of spatially varying internal heat transfer coefficients in a tube", *International Journal of Heat and Mass Transfer*, v. 108, pp. 90–96, 2017.

[48] TAHIRI, A., MANSOURI, K. "Theoretical investigation of laminar flow convective heat transfer in a circular duct for a non-Newtonian nanofluid", *Applied Thermal Engineering*, v. 112, pp. 1027–1039, 2017.

[49] BAZÁN, F. S. V., BEDIN, L. "Identification of heat transfer coefficient through linearization: explicit solution and approximation", *Inverse problems*, v. 33, n. 12, pp. 124006, 2017.

[50] OZISIK, M. N. *Heat Conduction*. John Wiley & Sons, Inc., 1993.

[51] OZISIK, M. N. *Finit Difference Method in Heat transfer*. CRC Press.

[52] FORTUNA, A. D. O. *Técnicas Computacionais par Dinâmica dos Fluidos Conceitos Básicos e Aplicaçoes*. edusp, 2000.

[53] CHUNG, T. J. *Computational fluid dynamics*. Cambridge University Press, 2002.

[54] VERSTEEG, H. K., MALALASEKERA, M. *An introduction to computational fluid dynamics The Finite Volume Method*. Longman Scientific & Technical, 1995.

[55] VERSTEEG, H. K., MALALASEKERA, M. *An Introduction to Computational Fluid Dynamics*. Pearson Education Limited, 2007.

[56] HIGGINS, J. R. *Cambridge Tracts in Mathematics 72 - Completeness and Basis Properties of Sets of Special Functions*, v. 72. Cambridge University Press, 1977.

[57] ROSE, J. W. "Heat-transfer coefficients, Wilson plots and accuracy of thermal measurements", *Experimental Thermal and Fluid Science*, v. 28, n. 2-3, pp. 77–86, 2004.

[58] ASTARITA, T., CARLOMAGNO, G. M. *Infrared Thermography for Thermo-Fluid-Dynamics*. Springer, Berlin, 2012.

[59] MEOLA, C., CARLOMAGNO, G. M. "Recent advances in the use of infrared thermography", *Measurement Science and Technology*, v. 15, n. 9, pp. R27–R58, 2004.

[60] PAVELKA, K., RUZICKA, S., BILA, S. "Photo-plan creation of cylindrical objects". In: ISPRS Annals of the Photogrammetry, R. S., Spatial Information Sciences, Volume II-5/W1, . (Eds.), *XXIV International CIPA Symposium, 2-6 September 2013, Strasbourg, France*.

[61] IMSL. *Fortran Subroutines for Mathematical Aplications.* Houston, Texas, Visual Numerics, Inc., 1997.

[62] PRESS, W. H., TEUKOLSKY, S. A., VETTERLING, W. T., *et al. Numerical Recipes in Fortran 77 The Art of Scientfic Computing*, v. 1. Cambridge University Press, 1986.

[63] PRESS, W. H., TEUKOLSKY, S. A., VETTERLING, W. T., *et al. Numerical Recipes in Fortran 90 The Art of Parallel Scientific Computing*, v. 2. Cambridge University Press 1986, 1996.

[64] BOX, G. E. P., MULLER, M. E. "A Note on the Generation of Random Normal Deviates", *Math. Statist*, v. 29, n. 2, pp. 610–611, 1958.

[65] ORLANDE, H. R. B., OLIVIER, F., COTTA, R. M. *Thermal Measurements and Inverse Techniques*. Taylor and Francis, New York, 2011.

[66] REINHARDT, H. J., HAO, D., FROHNE, J., *et al.* "Numerical solution of inverse heat conduction problems in two spatial dimensions", *J.Inverse Ill-posed Probl.*, v. 15, pp. 19–36, 2007.

[67] WHEELER, A. J., GANJI, A. *Introduction to Engineering Experiment*. Pearson Higher Education, 2010.